Impact of Fanconi-associated protein on the mitochondrial proteome

DISSERTATION ZUR ERLANGUNG DES

DOKTORGRADES DER NATURWISSENSCHAFTEN (DR. RER. NAT.)

DER FAKULTÄT FÜR BIOLOGIE UND VORKLINISCHE MEDIZIN

DER UNIVERSITÄT REGENSBURG

vorgelegt von

Nadine Aßmann

aus Kulmbach

im Jahr

2014

Das Promotionsgesuch wurde eingereicht am:
16.10.2014

Die Arbeit wurde angeleitet von:
Prof. Dr. Richard Warth

Unterschrift:

Für meine Familie

Danksagung

An dieser Stelle möchte ich mich bei allen bedanken, die mich während der Entstehung dieser Arbeit begleitet und unterstützt haben.

Mein besonderer Dank gilt **Prof. Dr. Peter Oefner** für die Möglichkeit am Institut für Funtionelle Genomik zu promovieren, seine Unterstützung während der gesamten Zeit, die Übernahme des Zweitgutachtens, die Bereitstellung des Arbeitsplatzes und die Möglichkeit mich durch die Teilnahme an verschiedensten Kursen ständig weiterzubilden.

Ein großer Dank geht an **Prof. Dr. Richard Warth**, für die Erstbetreuung der Dissertation und für die Möglichkeit einen Teil meiner Doktorarbeit an seinem Institut anfertigen zu können.

Für die Übernahme des Drittgutachtens bin ich **Prof. Dr. Jens Schlossmann** dankbar.

Dr. Jörg Reinders danke ich für die intensive, warmherzige und professionelle Betreuung, der Hilfe beim Auswerten der riesigen Datensätze und die stetige Diskussionsbereitschaft während aller Phasen meiner Doktorarbeit.

Für die Betreuung bei der Durchführung der Metabolomics-Messungen und ein stets offenes Ohr danke ich **Dr. Katja Dettmer-Wilde** und **Prof. Dr. Wolfram Gronwald**.

Bei den Sekretärinnen **Sabine Botzler** und **Eva Engl** möchte ich mich herzlich Bedanken für die Hilfe bei all den großen und kleinen Problemen.

Bei all meinen Kollegen der Proteomics-Gruppe **Sophie Schirmer**, **Dr. Yvonne Reinders**, **Anja Thomas**, **Corinna Feuchtinger†**, **Johann Simbürger** und **Elke Perthen** möchte ich mich für die stetige Unterstützung, die Hilfsbereitschaft und die enge Zusammenarbeit bedanken. Dabei gilt ein ganz besonderer Dank **Sophie Schirmer**, die mich schon während meiner Diplomarbeit am Institut hervorragend betreut hat, immer da war und mich unterstützt hat wenn es mal nicht so gut lief und für die enge Freundschaft die über die Zeit entstanden ist.

Ein herzliches Dankeschön geht an **Nadine Nürnberger** und **Claudia Samol**. Danke Nadine, dass du mit einer wirklich hervorragenden Musikauswahl das Arbeiten im Labor etwas aufgepeppt hast, für die unzähligen Einkaufsfahrten und deine Freundschaft. Danke, liebe Claudia, dass du mit deiner freundlichen, lieben und zuvorkommenden Art die Zeit am Institut wirklich unvergesslich gemacht hast, für die

Unterstützung über die ganze Zeit, die vielen aufmunternden Worte und ebenfalls für deine Freundschaft.
Nicht unerwähnt bleiben dürfen die anderen ständigen Mitglieder der Kaffeepause **Christian Wachsmuth**, **Magdalena Waldhier**, **Dr. Martin Almstetter**, **Dr. Matthias Klein** und **Lisa Ellmann**, die die Nachmittage wirklich unvergesslich gemacht haben.
Für die Lösung so mancher statistischer Probleme und die stetige Hilfsbereitschaft bei meinen Computerproblemen möchte ich mich ganz herzlich bei allen Mitarbeitern der Arbeitsgruppen von Prof. Dr. Rainer Spang und Dr. Claudio Lottaz bedanken. Dabei gilt ein besonderer Dank **Prof. Dr. Rainer Spang**, **Dr. Claudio Lottaz**, **Dr. Christian Hundsrucker**, **Dr. Katharina Meyer**, **Franziska Taruttis** und **Christian Kohler**.
Vielen Dank auch an die Mitarbeiter des Lehrstuhls für Medizinische Zellbiologie **Dr. Markus Reichold**, **Dr. Evelyn Humberg**, **Carsten Broeker**, **Christina Sterner** und **Ines Tegtmeier** für das angenehme Arbeitsklima und die Hilfsbereitschaft bei der Arbeit am Lehrstuhl.
Vielen Dank auch an **Dr. Kathrin Renner-Sattler** und **Stephanie Färber** für die Unterstützung bei der Durchführung der respirometrischen Messungen.
Ein herzlicher Dank geht auch an unsere Kooperationspartner aus England **Prof. Dr. Robert Kleta** und **Dr. Enriko Klootwijk** für das Bereitstellen der Zellkulturen und die gute Zusammenarbeit über all die Jahre.
Ein Dank geht auch an das Team des Kompetenzzentrums für Fluoreszente Bioanalytik **Dr. Thomas Stempfl**, **Dr. Christoph Möhle**, **Jutta Schipka** und **Susanne Schwab**. Vielen Dank für das Annehmen aller Pakete und die vielen netten Gespräche zwischendurch.
Ich möchte mich auch bei **Jochen Hochrein**, **Helena Zacharias**, **Philipp Schwarzfischer**, **Dr. Alexander Riechers** und **Franziska Vogl** für die Unterstützung in allen Phasen meiner Arbeit und das angenehme Arbeitsklima bedanken.

Der größte Dank gilt meinen Eltern **Sieglinde** und **Wolfgang Aßmann**, meinem Bruder **David Aßmann** und meiner Schwester **Nicole Schädler**, sowie deren Ehemann **Eugen Schädler** und Sohn **Jakob**. Vielen Dank, dass ihr mich immer Unterstützt habt, immer an meiner Arbeit interessiert wart, für die vielen aufmunternden Worte und dass ihr immer an mich geglaubt habt.

I. Table of contents

I. Table of contents 6

II. Abbreviations and Acronyms 10

1 Summary 13

2 Zusammenfassung 14

3 Introduction 16

3.1 The kidney 16

3.2 Transport processes in the proximal tubulus 18

3.2.1 Sodium transport 19

3.2.2 Luminal Na^+-coupled symporter for the transport of bicarbonate, glucose and amino acids 20

3.2.3 Protein and peptide transport 20

3.2.4 Water and chloride transport 21

3.3 Fanconi´s syndrome 22

3.3.1 Inherited Fanconi´s syndrome 23

3.3.2 Acquired Fanconi´s syndrome 24

3.4 Mitochondria 25

3.4.1 Mitochondrial structure 26

3.4.2 Mitochondrial energy metabolism 27

3.4.3 Mitochondrial protein import 34

3.5 Peroxisomes 37

3.5.1 Structure and Function 37

3.5.2 Peroxisomal protein import 41

3.6 Enoyl-coenzyme A hydratase / L-3-hydroxyacyl-coenzyme A dehydrogenase (EHHADH) 42

4 Aim of this work 44

5 Materials and Methods 45

5.1 Material 45

5.1.1 Cell line 45

5.1.2 Media 45

5.1.3 Buffers and Solutions 46

5.1.4 Antibodies 47

5.1.5 Kits, turnkey solution, marker 48

5.1.6 Consumable Material 49

5.1.7 Chemicals 50

5.1.8 Devices 53

5.1.9 Software 54

5.2 Methods 54

5.2.1 Cell culture work 54

5.2.2 Immunofluorescence staining 55

5.2.3 Isolation of mitochondria 56

5.2.4 BSA-fatty acid complex 57

5.2.5 SDS-PAGE with subsequent immunoblot analysis 58

5.2.6 Two-dimensional differential in-gel electrophoresis 59

5.2.7 Co-Immunoprecipitation 60

5.2.8 Blue native PAGE analysis 63

5.2.9 Metabolic analysis 64

5.2.10 High resolution respirometry 67

5.2.11 Citrate synthase activity measurement 68

5.2.12 Respiratory chain supercomplex assembly 69

5.2.13 SWATH™ analysis 69

5.2.14 Statistical analysis 70

6 Results 71

6.1 Stable overexpression and localization of EHHADH 71

6.1.1 Time series for EHHADH overexpression 71

6.1.2 Analysis of mistargeting of EHHADH by immunoblotting 71

6.1.3 Control of mistargeting of $EHHADH_{MUT}$ by immunofluorescence staining 72

6.1.4 Two-dimensional differential in-gel electrophoresis 73

6.2 Incorporation of mutated EHHADH into the mitochondrial trifunctional protein 74

6.2.1 Co-immunoprecipitation of EHHADH and HADHB 74

6.2.2 Blue native PAGE analysis 75

6.3 Respiratory chain analysis 76

6.3.1 High-resolution respirometry 76

6.3.2 Interaction analysis of EHHADH with the respiratory chain by 2D-blue native/ SDS-PAGE with subsequent immunoblot analysis 79

6.3.3 Quantification of supercomplex assembly 80

6.4 Metabolic analysis 82

6.4.1 Palmitic acid uptake 82

6.4.2 Metabolic analysis of acetyl-CoA 82

6.4.3 Acylcarnitne analysis 83

6.4.4 Measurement of ATP content 84

6.5 Proteomic analysis 85

7 Discussion 88

7.1 Localization and mistargeting of $EHHADH_{MUT}$ 88

7.2 Erroneous interaction of $EHHADH_{MUT}$ with the mitochondrial trifunctional protein 89

7.3 Effects of mistargeting of $EHHADH_{MUT}$ on mitochondrial fatty acid β-oxidation 90

7.4 Impact of impaired mitochondrial fatty acid β-oxidation on other cellular mechanisms 91
7.4.1 Uptake of exogeneous long-chain fatty acids 91
7.4.2 Formation of acetyl-CoA from β-oxidation 94
7.4.3 Generation of ATP 94
7.5 Global proteomic analysis of the *EHHADH$_{WT}$* and *EHHADH$_{MUT}$* cell lines 96
7.6 Effects of mistargeting of EHHADH$_{MUT}$ on mitochondrial respiration and supercomplex formation 97
7.7 Development of diseases due to the mistargeting of proteins 99
8 Conclusion and Outlook 101
III. References 102

II. Abbreviations and Acronyms

1D	One-dimensional
2D	Two-dimensional
2D-PAGE	Two-dimensional polyacrylamide gel electrophoresis
AAA	ATPase associated with various cellular activities
ACAD	Acyl-CoA dehydrogenase
ACOX	Acyl-CoA oxidase
ADP	Adenosine diphosphate
APS	Ammonium persulfate
ATP	Adenosine triphosphate
BisTris	Bis(2-hydroxyethyl)amino-tris(hydroxymethyl)methane
BSA	Bovine serum albumin
CACT	Carnitine acylcarnitine translocase
CHAPS	3-[(3-Cholamidopropyl)-dimethylammonio]-1-propanesulfonate
CoA	Coenzyme A
CoIP	Co-immunoprecipitation
CPT1	Carnitine-palmitoyltransferase I
CPT2	Carnitine-palmitoyltransferase II
DTT	1,4-dithio-D-threitol
DMSO	Dimethyl sulfoxide
DTNB	5,5’ - Dithiobis(2-nitrobenzoic acid)
EDTA	Ethylenediaminetetraacetic acid
EGTA	Ethylene glycol tetraacetic acid
EHHADH	Enoyl-Coenzyme A hydratase / L-3-Hydroxyacyl-Coenzyme A dehydrogenase, L-bifunctional enzyme
ESI	Electrospray ionization

ETC	Electron transport chain
ETF	Electron transfer flavoprotein
FA	Fatty acid
FAD	Flavin adenine dinucleotide
FATP	Fatty acid transport protein
FCCP	Carbonylcyanide p-(trifluoromethoxy)phenylhydrazone
FCS	Fetal calf serum
FDR	False discovery rate
FMN	Flavin mononucleotide
GC	Gas chromatography
GFR	Glomerular filtration rate
HEPES	2-[4-(2-hydroxyethyl)piperazin-1-yl]ethanesulfonic acid
HFBA	2,2,3,3,4,4,4-Heptafluorobutanoic acid
HPLC	High-performance liquid chromatography
HRP	Horseradish peroxidase
IDA	Information Dependent Acquisition
IMM	Inner mitochondrial membrane
IPG	Immobilized pH-gradient
LCAD	Long-chain acyl-CoA dehydrogenase
LCHAD	Long-chain 3-hydroxyacyl-CoA dehydrogenase
MCAD	medium-chain acyl-CoA dehydrogenase
MEMα	Minimum Essential Medium Eagle , alpha modification
MOPS	4-Morpholinopropanesulfonic acid
MPC	Mitochondrial pyruvate carrier
MSD	Mass Selective Detector
MS/MS	Tandem mass spectrometry
NAD+	Nicotineamide adenine dinucleotide

OMM	Outer mitochondrial membrane
PBS	Phosphate buffered saline
PFA	Paraformaldehyde
PMSF	Phenylmethylsulfonyl fluoride
PTS	Peroxisomal targeting sequence
PVDF	Polyvinylidene difluoride
RNS	Reactive nitrogen species
ROS	Reactive oxygen species
RPMI 1640	Roswell Park Memorial Institute Medium 1640
SCAD	Short-chain acyl-CoA dehydrogenase
SDS	Sodium dodecyl sulfate
SWATH-MS	Sequential Windowed data independent Acquisition of the Total High-resolution Mass Spectra
TCA cycle	Tricarboxylic acid cycle
TEMED	N,N,N′,N′-Tetramethylethane-1,2-diamine
TIM	Translocase of the inner membrane
TMPD	N,N,N',N'-Tetramethyl-1,4-phenylenediamine
TOF	Time-of-flight
TOM	Translocase of the outer membrane
Tris	2-Amino-2-hydroxymethyl-propane-1,3-diol
VLCAD	Very-long-chain acyl-CoA dehydrogenase

1 Summary

This work describes the analysis of a novel, isolated, autosomal dominant form of Fanconi´s syndrome, a disorder of the renal proximal tubule associated with decreased reapsorption of solutes from the primary urine. This yet unknown Fanconi´s syndrome is evoked by a mutation in the third codon of the peroxisomal protein enoyl-CoA hydratase / L-3-hydroxyacyl-CoA dehydrogenase (EHHADH), also called “Fanconi-associated protein”, which results in the substitution of a glutamic acid residue with lysine (p.E3K). By complementing proteomic and metabolomic analyses of wildtype- and mutant-*EHHADH*-expressing proximal tubular cell lines (LLC-PK1) with different biochemical and cell biological investigations, the underlying pathomechanism is elucidated. The E3K-mutation leads to the erroneous localization of peroxisomal EHHADH into mitochondria causing a mitochondriopathy. Upon mistargeting of $EHHADH_{MUT}$ into mitochondria, it replaces an alpha subunit of the mitochondrial trifunctional protein (MTP). The MTP normally builds a heterooctamer consisting of four alpha and four beta subunits and is involved in mitochondrial fatty acid β-oxidation. The incorporation into MTP impairs both mitochondrial β-oxidation and respiratory supercomplex assembly, leading to a decreased oxidative phosphorylation capacity. Impairment of the former is shown by the characteristic accumulation of hydroxyacyl-, enoyl- and acylcarnitines in the cell culture supernatant, thus resembling the situation in patients with MTP and/or LCHAD deficiency. The impaired mitochondrial β-oxidation consequently decreases cellular long-chain fatty acid uptake and the acetyl-CoA production in $EHHADH_{MUT}$ cell line. In addition, $EHHADH_{MUT}$ is also incorporated into respiratory supercomplexes, thereby disturbing their assembly, as shown by blue native PAGE. As a result of impaired mitochondrial β-oxidation and diminished supercomplex assembly the $EHHADH_{MUT}$ cell line shows a decreased oxidative phosphorylation capacity and reduced ATP generation. This mitochondriopathy results in the decreased tubular reabsorption of electrolytes and low-molecular-weight proteins, leading to the Fanconi´s syndrome.

2 Zusammenfassung

Diese Arbeit beschreibt die Analyse einer neuen Form eines isolierten, autosomal dominanten Fanconi Syndroms, einer Erkrankung des proximalen Tubulus der Niere, die mit einer verringerten Absorption verschiedener Komponenten aus dem Primärharn einhergeht. Dieses bisher unbekannte Fanconi Syndrom wird durch eine Mutation am N-terminalen Ende des peroxisomalen Proteins Enoyl-CoA Hydratase / L-3-Hydroxyacyl-CoA Dehydrogenase (EHHADH), auch „Fanconi-assoziertes Protein“ genannt, hervorgerufen. In dieser Arbeit werden proteomische und metabolomische Analysen einer renalen proximalen tubulären Zelllinie (LLC-PK1) durch verschiedene biochemische und zellbiologische Untersuchungsmethoden ergänzt, um den zugrundeliegenden Pathomechanismus aufzuklären. Die E3K-Mutation führt zu einer fehlerhaften Lokalisierung von EHHADH in die Mitochondrien, wodurch eine Mitochondriopathie hervorgerufen wird. In den Mitochondrien wird $EHHADH_{MUT}$ ins mitochondriale trifunktionelle Protein (engl.: „mitochondrial trifunctional protein / MTP“) an Stelle einer alpha-Untereinheit eingebaut. Das MTP ist an der mitochondriellen β-Oxidation von Fettsäuren beteiligt und besteht normalerweise aus je vier alpha- und beta-Untereinheiten, welche ein Hetero-Oktamer bilden. Der Einbau ins MTP beeinträchtigt dabei sowohl die mitochondriale β-Oxidation von Fettsäuren als auch die Zusammensetzung der Superkomplexe der Atmungskette. Beide Vorgänge führen zu einer verringerten Aktivität der oxidativen Phosphorylierung.

Die Störung der mitochondrialen β-Oxidation wird durch die charakteristische Akkumulation von Hydroxyacyl-, Enoyl- und Acylcarnitinen im Zellkulturmedium experimentell bestätigt; damit weisen die Medien ein ähnliches Muster wie Seren von Patienten mit MTP- und/oder LCHAD-Defizienz auf. Die gestörte mitochondriale β-Oxidation von Fettsäuren führt nachfolgend zu einer erniedrigten zellulären Aufnahme langkettiger Fettsäuren und zu einer erniedrigten Produktion von Acetyl-CoA in der *$EHHADH_{MUT}$* Zelllinie. Zusätzlich zu der gestörten β-Oxidation ist auch die Bildung von Superkomplexen der Atmungskette gestört. Aufgrund dessen sind die oxidative Phosphorylierung und ATP-Produktion in den betroffenen Zelllinien erniedrigt. Die durch die Mislokalisation entstandene Mitochondriopathie ist der Grund für die erniedrigte tubuläre Resorption von Glukose, Aminosäuren, Phosphat,

Kalium und niedermolekularen Proteinen, welche in erster Linie zu Minderwuchs und Vitamin-D-resistenter Rachitis führt.

3 Introduction

3.1 The kidney

The kidneys are paired, bean-shaped organs, that are located in human behind the retroperitoneum in the abdominal cavity, one on either side of the spine, between the twelfth thoracic vertebra and the third lumbar vertebra [1]. They have three main functions: they are major excretory organs, they regulate the salt- and water balance, and they have an endocrine function. Each kidney contains about 0.5 – 1 million nephrons that are divided in cortical and juxtamedullary nephrons. Each nephron is composed of a glomerulus and a tubular apparatus [2]. The glomerulus is located in the cortex of the kidney and fed with blood by the afferent arteriole, which splits into the glomerular capillary loops and exits through the efferent ateriole. Along the glomerular capillary wall the blood is filtered, by which the primary urine is produced into the Bowman´s space.

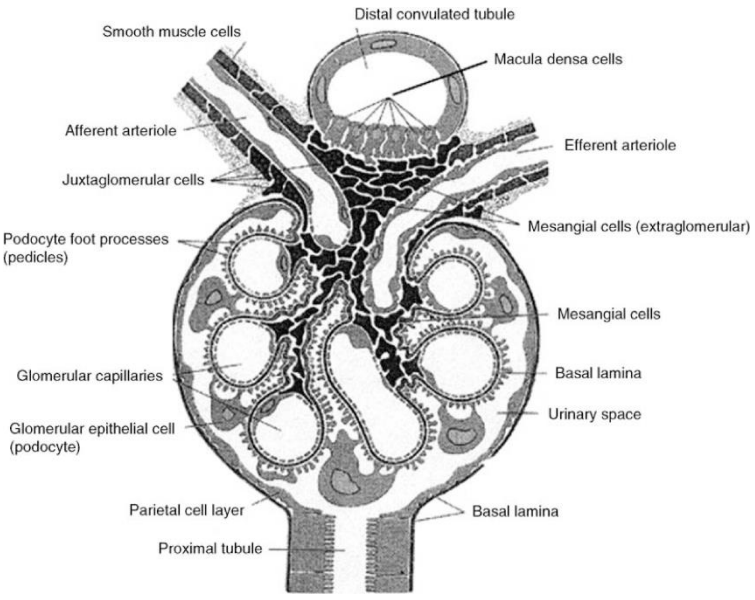

Figure 1: Schematic representation of a glomerulus.

(Figure from Avner E. D., H.W.E., Niaudet P., Yoshikawa N., Pediatric Nephrology, Springer Verlag Berlin Heidelberg, Sixth Edition.)

Every day about 170 L of primary urine are filtered in the glomerula. The transudation along the capillary wall happens across three layers: the endothelial cells of the capillary wall with endothelial pores, the circumambient basement membrane, and

the glomerular epithelial cells (podocytes) with foot protrusions on the side of the Bowman´s space. The glomerular filtration is a permselective and pressure dependent process due to the hydrostatic and oncotic pressure difference between capillary lumen and the Bowman´s space [1]. The selective permeability depends on both the size and the charge of molecules. Only molecules with a diameter < 4 nm and a molecular weight < 50 kDa are filtered across the capillary wall, and the basement membrane is nearly impermeable to negatively charged macromolecules [1-3] due to its high content of negatively charged heparan sulfate.

Subsequent to the urinary pole, the tubular apparatus arises. The main function of the tubular apparatus is the production of urine from the primary urine. The tubular apparatus is divided into different segments: proximal tubule, Henle´s loop, distal tubule, and the collecting duct.

The mitochondria-rich proximal tubule is responsible for the reabsorption of nearly all the filtered water and solutes, approximately two thirds of the previously filtered NaCl, 95% of the bicarbonate, and the entire glucose and amino acids [2]. Characteristic for the proximal tubule cells is the brush-border membrane, which creates a large luminal surface, as well as the “leaky” tight junctions, which are permeable for small ions and water [3]. The pars recta, the straight segment of the proximal tubule, the descending and ascending thin limb segment and the thick ascending limb are parts of the loop of Henle. The loop of Henle is responsible for the formation of an osmotic gradient for the urinary concentration. The pars recta shows the same transport systems as the proximal tubule, and the thin descending limb segment shows nearly no active transport, however a passive transport of cations takes place through the “leaky” tight junctions. The thin ascending limb segment and the thick ascending limb are the important parts of the loop of Henle. They show active transport of NaCl from the luminal to the basolateral side, while they are impermeable to water, resulting in a higher osmolarity in the interstitial space. Water is transported through the loop-like arrangement of the tubule and the higher interstitial space osmolarity from the thin descending limb to the interstitial space, which leads to a concentrated luminal fluid in the descending limb segment. In the ascending limb segment more solutes are transported into the interstitital space, so that the osmolarity of the tubular fluid drops. Thus, the tubular fluid is hypotonic at the end of the loop of Henle [2]. The thick ascending limb comes in contact with the vas afferens of the own glomerulum at the end of the loop of Henle (Figure 1). To be more precise, the macula densa cells of

the thick ascending limb touch the extraglomerular mesangial cells and the renin producing juxtaglomerular cell of the vas afferens. Together, the three cell types build the juxtaglomerular apparatus, which regulates the function of each nephron. In case of an elevated blood pressure, which is accompanied with an elevated glomerular filtration rate (GFR), this can only partly be rescued by the autoregulation of the kidney. This elevated GFR leads to an increased concentration of NaCl in the ascending limb segment of the loop of Henle. The registered elevated NaCl concentration is counteracted by a constriction of the afferent arteriole, thereby decreasing the GFR. A decrease in NaCl concentration on the other hand, has the inverse effect. Subsequent to the juxtaglomerular apparatus the tubular fluid reaches the distal tububule ending in the collecting duct. The fine tuning of the urine occurs in the distal nephron segment. In contrast to the “leaky” tight junctions of the proximal tubulus and the loop of Henle, the tight junctions of the distal nephron are tight. The nadir of luminal fluid osmolality is achieved in the distal nephron, where NaCl is also resorbed form the luminal fluid and the membrane is impermeable to water. The urine has an osmolality of ~ 50 mOsm/kg water entering the collecting duct [4]. The urine produced by the nephrons is initially collected in the renal pelvis, to be then transported over the ureter to the urinary bladder.

3.2 Transport processes in the proximal tubulus

The proximal tubule is the first segment of the tubular component of the nephron. It is responsible for the reabsorption of nearly all the filtered water and solutes. This means that in the proximal tubule 60% of the sodium, as well as 60% of the potassium, water and chloride, 95 % of the bicarbonate, and nearly all of the filtered glucose and amino acids are reabsorbed. For a detailed overview of the reabsorbed solutes and water see also Table 1.

Table 1: Transport of substances in the proximal tubulus segment [2].

Substances	Transport in the proximal tubulus in %
Water	60
Creatinine	0
Sodium	60
Chloride	55
Potassium	60
Bicarbonate	95
Calcium	60
Phosphate	70
Magnesium	30
Glucose	99
Amino acids	99
Urea	50

In the proximal tubule four main transport mechanisms are at work, the primary-active transport, the secondary-active transport, endocytosis of large molecules, and passive transport across the “leaky” tight junctions. These transport processes are shown schematically in Figure 2.

3.2.1 Sodium transport

The steep electrochemical gradient of sodium is generated by the Na^+/K^+-ATPase, which is imbedded in the basolateral membrane. The Na^+/K^+-ATPase exports three sodium ions and imports two potassium ions for every ATP consumed. It is an example for a primary active transport of the proximal tubular cell. This primary-active transport of sodium and the resulting concentration gradient is a requirement for the secondary-active transport of sodium on the luminal side, where it is transported into the cell through the Na^+-coupled symporter, or the Na^+/H^+-antiporter. On the basolateral side sodium is transported out of the cell by the $Na^+,3HCO_3^-$ -symporter. In addition to the primary- and secondary-transport of sodium, sodium is also passively transported into the interstitium over the “leaky” tight junctions.

3.2.2 Luminal Na^+-coupled symporter for the transport of bicarbonate, glucose and amino acids

At the luminal membrane, different Na^+-coupled symporters are responsible for the secondary-active transport of bicarbonate, glucose and amino acids.

Bicarbonate is produced in the proximal tubular cells by the carboanhydrase, which is imbedded in the luminal membrane. This bicarbonate is exported into the interstitium by the basolateral $Na^+,3HCO_3^-$ -symporter.

Glucose is imported into the proximal tubular cells via a luminal Na^+-coupled symport. Two different symporters, SGLT1 and SGLT2, are responsible for the import of glucose at the luminal membrane. SGLT1 couples the transport of glucose and galactose to the transport of two sodium ions, while SGLT2 couples the transport of glucose to one sodium ion. SGLT1 has a higher affinity than SGLT2. In the early proximal tubulus 95 % of the glucose is reabsorpted by the action of SGLT2. Together with the action of SGLT 1 at the end of the proximal tubulus, nearly all of the glucose is reabsorbed.

3.2.3 Protein and peptide transport

Di - and tripeptides are reabsorbed at the luminal membrane by peptide-H^+-symporters. Peptides with disulfide bridges and proteins are reabsorbed through endocytosis. First, these proteins are bound to specified receptors at the luminal membrane. Then the protein-receptor complexes are enclosed in small vesicles that are invaginated from the cellular plasma membrane [5]. Through the action of Na^+/H^+-antiporter and H^+-ATPase, protons are pumped into the protein containing vesicles. This leads to the dissociation of the protein-receptor complex. Finally, the vesicles are fused with lysosomes. The proteins are degraded to their corresponding amino acids and the receptors are recycled back to the luminal membrane. The resulting amino acids are transported through the cytosol and the basolateral membrane into the interstitium [2]. Less than 1% of proteins and peptides remain in the primary urine.

3.2.4 Water and chloride transport

Primary- and secondary active transport of solutes from the luminal fluid in the proximal tubular cells lead to a passive transport of water through water channels in the cell membrane and across the tight junctions. This transport of water drags along the water-solved ions such as chloride (solvent drag). In addition to the solvent drag, chloride is also transported through the “leaky” tight junctions.

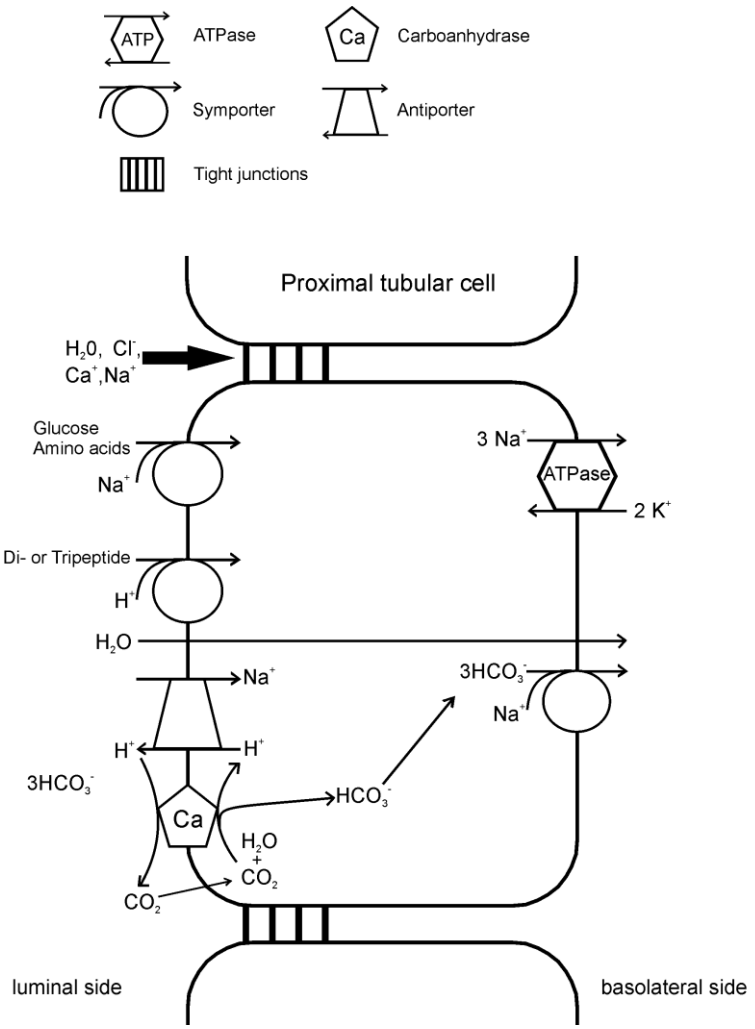

Figure 2: Schematic representation of the transport processes in the proximal tubular segment.

3.3 Fanconi´s syndrome

The Fanconi´s syndrome is named after the swiss pediatrician Guido Fanconi (1892-1979) and is a generalized disorder of the proximal tubule, leading to excessive urinary wasting of water, amino acids, glucose, electrolytes, and low-molecular-weight proteins.

First Abderhalden [6] described in 1903 a 21 month-old infant with cystine crystals infiltrated the inner organs at autopsy. Abderhalden called the disease familiar cystine diathesis, which is a common cause of Fanconi´s syndrome in children [7,8]. In 1924 Lignac [9] described cystinosis in three children who also presented severe rickets and growth retardation. Fanconi described in 1931 [10] a child with glucosuria and albuminuria in addition to cystinosis, which are additional aspects of Fanconi´s syndrome. Both, Lignac and Fanconi, also described degenerative changes in the proximal tubules [11]. Later on, De Toni [12] found hypophosphatemia to be a further clinical issue and Debré [13] determined also elevated levels of organic acids in urine in an 11-year old girl. In 1936, Fanconi [14] determined that all of the former described patients show similarities and described it as the nephrotic-glucosuric dwarfism with hypophosphatemic rickets [15,16]. McCune et al [17] and Stowers and Dent [18] confirmed the finding of Fanconi that the amino-aciduria and the other clinical issues originated within the kidney [11].

The Fanconi´s syndrome is manifested by a global disruption of sodium-coupled transporter systems. A low intracellular Na^+ concentration is established at the basolateral membrane by the action of the Na^+-K^+-ATPase. This low intracellular concentration is required for the maintenance of the lumen-to-cell gradient, which promotes the Na^+-coupled solute entry at the luminal membrane. An inhibition of the basolateral Na^+-K^+-ATPase or a decrease in the cellular ATP-ADP ratio will exert a tremendous influence on the reabsorption in the proximal tubule segment. In addition to the reabsorption of most solutes from the primary urine, the proximal tubule segment is also responsible for the uptake of low molecular weight proteins from the glomerular filtrate via receptor-mediated endocytosis. The receptors for this process are megalin and cubulin, which are present at the luminal membrane. Possible causes for proteinuria are a lack of the receptors at the luminal membrane, defective endocytosis, such as impaired acidification of early endosomes, and accumulation of toxic agents.

The Fanconi´s syndrome is a class of inherited or acquired diseases, or is caused by the action of exogenous substances.

Table 2: Range of different forms of Fanconi´s syndrome [4].

Inherited	Acquired
Lowe syndrom	Sjögren syndrome
Dent-1 disease	Nephrotic syndrome
Dent-2 disease	Renal transplantation
Cystinosis	Multiple Myeloma
Fanconi-Bickel syndrome	
Idiopathic Fanconi syndrome	**Exogenous substances:**
Wilson disease	Drugs
Mitochondriopathies	Chemical compounds
	Heavy metals

Understanding of the development of the different forms of inherited and acquired Fanconi´s syndrome provides important insights in proximal tubular transport.

3.3.1 Inherited Fanconi´s syndrome

Dent´s disease is a rare X-linked proximal tubulopathy with a full-blown Fanconi´s syndrome, but rare extrarenal symptoms except for rickets [4,19]. Depending on the genetic cause and pattern of signs and symptoms, two forms of Dent's disease are distinguished.

Dent-1 disease is caused by mutations in the *CLCN5* gene, which encodes for a renal specific voltage-dependent electrogenic chloride/proton antiporter. The CLC-5 antiporter is coexpressed with the vacuolar H^+-ATPase [4] and is involved in the acidification of early endosomes. The decreased acidification of the early endosomes during endocytosis leads to a diminished recycling of megalin and cubulin back to the luminal membrane, causing the low-molecular-weight proteinuria. In addition, patients with Dent-1´s disease also present with increased urinary excretion of phosphate and calcium, which lead to kidney stones, nephrocalcinosis and, eventually, progressive renal failure [20].

Dent-2 disease is caused by mutations in the classical Lowe oculocerebrorenal syndrome gene, *OCRL* [21]. Compared to classical Lowe syndrome, patients suffering

from Dent-2 disease present with milder extrarenal symptoms. Nephrocalcinosis is also seen less frequently than in Dent-1 disease [22].

Lowe syndrome is also a rare X-linked disorder. It is characterized by a complex phenotype involving major abnormalities of the eyes, central nervous system and an incomplete renal Fanconi´s syndrome [4]. The OCRL gene encodes for phosphatidylinositol 4,5-bisphosphate phosphatase (PIP_2 5-phosphatase), which colocalizes in proximal tubular cells with clathrin and megalin at the luminal membrane [22]. It interferes with the actin cytoskeleton, and is involved in the inositol phosphatase signaling pathway [4]. The involvement of PIP_2 5-phosphatase in endocytosis explains the similarities seen in renal involvement between Lowe syndrome and Dent´s disease. The decreased activity of PIP_2 5-phosphatase leads to an accumulation of phosphatidylinositol 4,5-bisphosphate (PIP_2) and actin stress fibres, which have an tremendous effect on epithelial function[4].

Mitochondriopathies are other inherited causes for Fanconi´s syndrome, as is the case with the Fanconi´s syndrome studied here. In proximal tubular cells, the major source of energy is fatty acid oxidation [23]. Proximal tubular cells reabsorb solutes and water from the glomerular filtrate close to the cellular energy demand as Beck et al. [24] showed an intracellular decrease in ATP after stimulation of sodium-dependent transport. Therefore, it is not surprising, that inherited mitochondriopathies, which are caused by mutation of mitochondrial or nuclear DNA encoding for functional or structural mitochondrial proteins, are often associated with Fanconi´s syndrome.

3.3.2 Acquired Fanconi´s syndrome

Fanconi´s syndrome can also occur secondary to certain diseases or after the administration of exogenous substances. The development of a Fanconi´s syndrome secondary to a disease is rarely seen. In patients with Sjögren syndrome, only 3 % manifest Fanconi´s syndrome [25]. Equally uncommon is the development of a Fanconi´s syndrome [4] after renal transplantation. In multiple myeloma, renal involvement mostly manifests as proteinuria and only rarely as full-blown Fanconi´s syndrome [26].

Exogenous substances such as drugs, chemicals and heavy metals, can also cause Fanconi´s syndrome. Drugs like valproic [27] acid, tenofovir [28], Chinese herbs [29,30] or

expired tetracycline [31] have been reported to cause a Fanconi´s syndrome. The decreased transport of proximal tubular cells after the administration of valproic acid originates from the fact that this drug causes respiratory chain defects and decreases lysosomal enzyme activity [4]. The major degradation products of expired tetracycline, namely epitetracycline, anhydrotetracycline and 4-epianhydrotetracycline, are also toxic to proximal tubular cells [32]. Antiviral agents, for example adefovir, which acts a reverse transcriptase inhibitor, interact with organic anion transporter and lead to mitochondrial damage and tubular toxicity. The non-specific herbicide paraquad, toluene and 6-mercaptopurine may also lead to Fanconi´s syndrome and renal failure. The kidney is the first organ of heavy metal toxicity, including lead, cadmium, mercury, chromium and platinum. Lead poisoning leads to the development of a Fanconi´s syndrome, with aminoaciduria and glucosuria which can persist for up to 13 years [4,33]. Lead thereby disrupts mitochondrial respiration, phosphorylation and can directly inhibit SLC3A1, which is a renal amino acid transporter for the transport of neutral and basic amino acids across the renal brush border [34]. The threshold for proximal tubular injury by lead is a blood lead level of 60 µg/dL [33]. Cadmium, on the other hand, causes Fanconi's syndrome via production of free radicals that alter mitochondrial activity or induce mitochondrial gene deletion following long time exposure and inhibits H^+-ATPase which leads to a Fanconi-like syndrome [4].

3.4 Mitochondria

The mitochondrion is a membrane bound organelle found in most eukaryotic cells. Mitochondria are mostly shaped like a rod. They are between 2 - 8 µm in length and 0.2 - 1 µm in diameter [5]. Especially cells with high energy-demand are rich in mitochondria, as seen in cardiac cells, muscle cells, cells of the central nervous system, sensory cells, ovocytes, sperm and cells of the proximal tubule. Furthermore, mitochondria are localized to specific cytoplasmic areas [35] for efficient provision of energy where it is needed, which is the basolateral membrane in the case of proximal tubule cells. The main function of mitochondria is to provide energy to the cell in the form of adenosine triphosphate (ATP). In mitochondria the main energy producing pathways are located: they include the oxidation of pyruvate, the mitochondrial fatty acid β-oxidation, tricarboxylic acid cycle and the oxidative phosphorylation. Biogenesis of mitochondria is a dynamic process, with constant mitochondrial fusion

and fission. When the energy demand of a cell increases, the number of mitochondria will be increased by mitochondrial fission. Mitochondria are inherited normally solely from the maternal side, however there are cases where also paternal mitochondria are found [36]. Healthy paternal mitochondria are eliminated usually during embryogenesis through a process that is not well understood. Consequently, the mitochondria found are solely of maternal origin. The endosymbiotic theory from 1883 postulates, that mitochondria originate from prokaryotes, which were incorporated into a so-called primordial cell as endosymbionts and, subsequently, reduced to organelles. Facts supporting this theory are that the phospholipid cardiolipin present in the inner mitochondrial membrane (IMM) is normally only seen in prokaryotes and that mitochondria have their own cyclic DNA.

3.4.1 Mitochondrial structure

Mitochondria are composed of four main components, the outer membrane, the intermembrane space, the inner membrane and the miochondrial matrix (Figure 3). The mitochondrium is separated from the cytosol by the outer mitochondrial membrane (OMM). The inner mitochondrial membrane (IMM) separates the intermembrane space from the mitochondrial matrix.

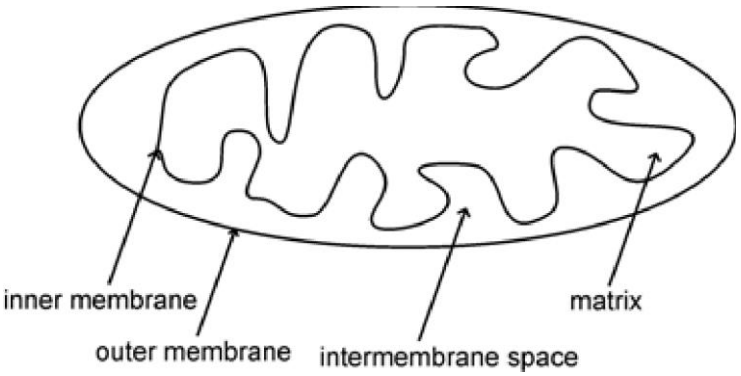

Figure 3: Schematic illustration of the mitochondrial structure.

The mitochondrial membranes are mainly composed of phosphatidyl choline, phosphatidyl ethanolamine, cardiolipin and phosphatidyl inositol [37]. Each component has a specific assignment in mitochondrial function. The OMM separates the intermembrane space from the cytosol and is freely permeable for small proteins up to 5,000 Da through protein complexes called porines [38]. Larger proteins, in contrast,

must be actively transported through the outer mitochondrial membrane by a transport complex called TOM (translocase of the outer membrane). The main function of the intermembrane space is oxidative phosphorylation. Other functions include the exchange of proteins, lipids, or metal ions between the matrix and the cytosol, the regulated initiation of apoptotic cascades, signalling pathways that regulate respiration and metabolic functions, and the prevention of reactive oxygen species produced by the respiratory chain [39]. The inner mitochondiral membrane (IMM) separates the intermembrane space from the mitochondrial matrix. The IMM is extensively folded in so-called cristae to increase its surface area, which is about five times as large as that of the OMM. The IMM is responsible for the import of proteins, lipids and other important metabolites into the mitochondrial matrix. In contrast to the OMM, it is completely impermeable, so that everything has to be transported actively. The impermeability is also a requirement for the maintenance of the proton gradient (ΔpH) and membrane potential ($\Delta\psi$), which are a requirement for the electrochemical gradient ($\Delta\mu H^+$). The mitochondrial matrix contains the cyclic double-stranded DNA and the whole machinery needed for the transcription and translation of the mitochondrial-encoded proteins. In addition, the enzymes for the important energy generating pathways are localized in the mitochondrial matrix or the IMM.

3.4.2 Mitochondrial energy metabolism

In mitochondria the main energy generating pathways are located, oxidation of pyruvate to acetyl-CoA, tricarboxylic acid cycle (TCA) cycle, mitochondrial fatty acid β-oxidation and oxidative phosphorylation. Mitochondria are also important for the controlling of the cellular redox state, Ca^{2+} homeostasis and apoptosis [40].

<u>Oxidation of pyruvate</u>

Pyruvate generated in glycolysis is transported into the mitochondria by the mitochondrial pyruvate carrier (MPC). In the mitochondrial matrix, pyruvate is irreversibly decarboxylated by the action of the pyruvate dehydrogenase complex to form acetyl-CoA, which enters the tricarboxylic acid cylce. Cofactors of this reaction are thiamine pyrophosphate, coenzyme A, α-lipoic acid, FAD, and NAD^+. This reaction links glycoylsis and the TCA cylce.

Tricarboxylic acid cycle

Enzymes of the TCA cycle are located in the mitochondrial matrix. In the first step of the TCA cycle, acetyl-CoA generated by the decarboxylation of pyruvate or the ß-oxidation of even-numbered saturated fatty acids reacts with oxaloacetate to from citrate. Citrate is transformed into isocitrate by isomerisation. In two subsequent oxidative decarboxylation reactions, first α-ketoglutarate and then succinyl-CoA are formed, with each reaction yielding NADH and H^+. Through the reaction of succinyl-CoA to succinate, the high phosphate transfer potential compound GTP is formed. Succinate is then FAD-dependent oxidized to fumarate, and through the addition of water malate is formed. In the last step, malate is oxidized to oxaloacetate in a reaction catalyzed by malate dehydrogenase, which also yields NADH and H^+. Oxalacetate reacts again with acetyl-CoA, providing citrate for another round of the TCA cycle.

The net reaction is:

$$\text{acetyl-CoA} + 3\ NAD^+ + FAD + GDP + P_i + 2\ H_2O \rightarrow 2\ CO_2 + CoA + 3\ NADH + 3H^+ + FADH_2 + GTP$$

The reducing equivalents NADH and $FADH_2$ directly enter oxidative phosphorylation.

Mitochondrial fatty acid β-oxidation

For mitochondrial β-oxidation, fatty acids are activated in the cytosol, generating membrane-impermeable acyl-CoAs, which are subsequently transported into the mitochondrial matrix by the carnitine carrier system, which is schematically depicted in Figure 4. Upon release into the mitochondrial matrix, the acyl-CoAs are broken down to generate acetyl-CoA, which enters the TCA cycle, and NADH and FADH2, which are used by the electron transport chain.

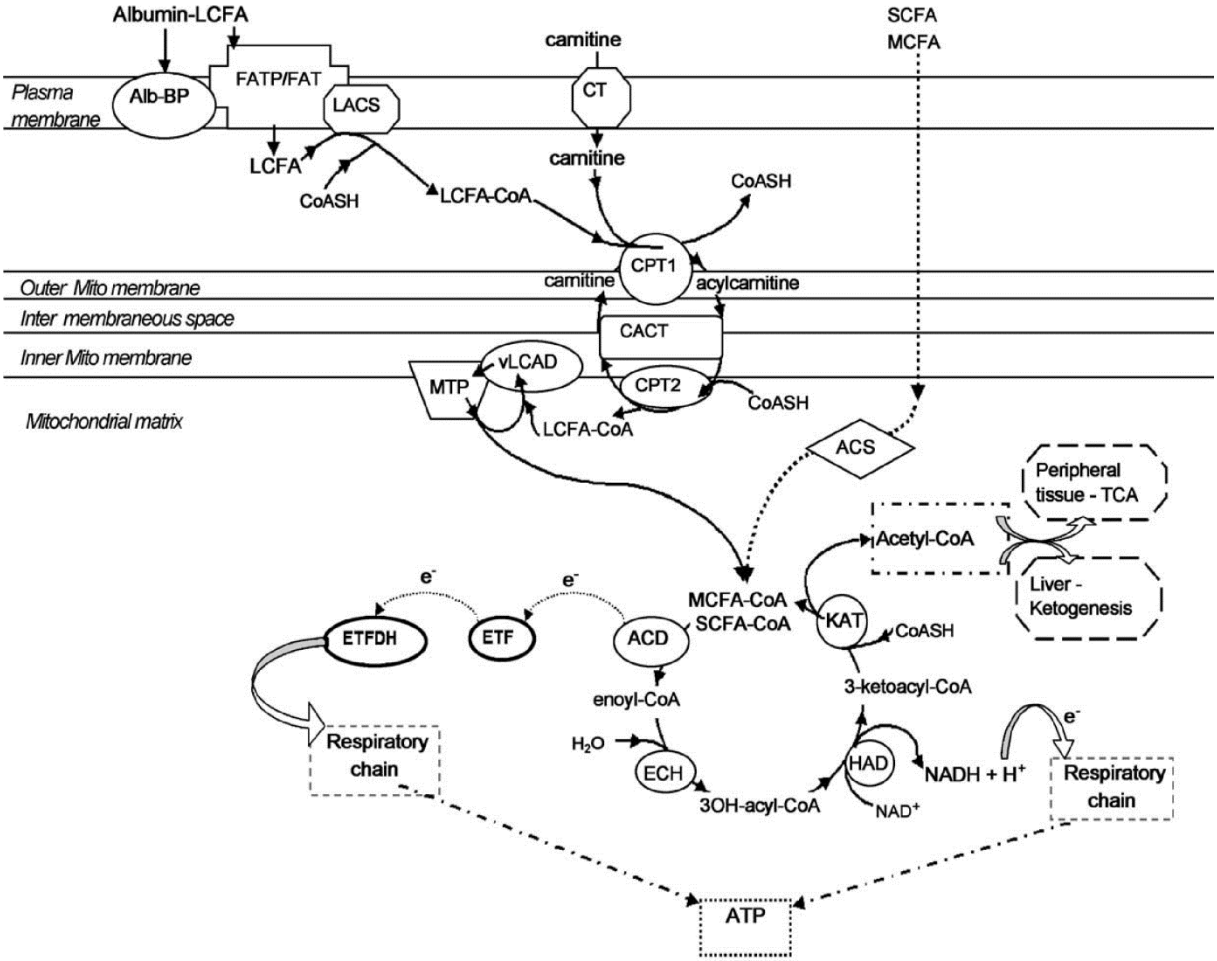

Figure 4: Scheme of the carnitine carrier system and subsequent fatty acid β-oxidation. The activated long-chain fatty acids (LCFA-CoA) are transported by the carnitine carrier system, which consists of the CPT1, CACT and CPT2, into the mitochondrial matrix. The LCFA-CoA are converted into their corresponding acylcarnitines by the CPT 1, transported across the IMM by CACT and, ultimately, reconverted into the activated long-chain fatty acids by CPT2. In the mitochondrial matrix, the LCFA-CoA subsequently undergoes the first round in the β-oxidation spiral. Chain shortening of LCFA-CoAs takes place by the repeated action of four enzymatic reactions, oxidation of an acyl-CoA by the acyl-CoA dehydrogenase (AD) with flavin adenine dinucleotide (FAD) as cofactor, hydration of enoyl-CoA by the enoyl-CoA hydratase, a second oxidation step using the cofactor nicotineamide adenine dinucleotide (NAD^+) and in the end a thiolytic cleavage by 3-keto-thiolase.
(Illustration taken from Sim, K.G:, Hammond, J., Wilcken, B. Strategies for the diagnosis of mitochondrial fatty acid beta-oxidation disorders. Clin Chim Acta 2002; 323:37-58)

Long-chain fatty acids represent the majority of the dietary fat undergoing ß-oxidation [41]. The latter plays an essential role in the energy metabolism of proximal tubular cells, which derive almost their entire energy from β-oxidation of mostly long-chain fatty acids [42]. The enzymes of mitochondrial fatty acid β-oxidation are located at the inner face of the inner mitochondrial membrane as well as are distributed in the

mitochondrial matrix [43]. Chain shortening of long-chain fatty acids takes place by the repeated action of four enzymatic reactions (Figure 4).

In the first reaction, an acyl-CoA is oxidized to a trans-2,3-enoyl-CoA by acyl-CoA dehydrogenases (ACADs). This reaction produces a $FADH_2$, which directly enters the oxidative phosphorylation at the electron transfer flavoprotein (ETF). The electrons form $FADH_2$ are transferred to ETF, the reduced ETF is then oxidized by the ETF:ubiquinone oxidoreductase transferring the electrons to ubiquinone, which is then reduced to ubiquinol. By the action of complex II of the respiratory chain ubiquinol is reoxidized to ubiquinone.

The second enzyme of the β-oxidation spiral is enoyl-CoA-hydratase, which forms L-3-hydroxyacyl-CoA by the addition of water to the double bond. The hydroxy-group is in the next step NAD^+-dependent oxidized to the corresponding ketoacyl-CoA. The reducing equivalent NADH is oxidized by the respiratory chain complex I.

In the last step of the β-oxidation, which is catalyzed by keto-thiolase, the terminal acetyl-CoA is cleaved off to yield an acyl-CoA shortenend by two carbon atoms. The cleaved acetyl-CoA can then enter into the TCA and electron transport chain (ETC).

In fatty acid β-oxidation, fatty acids are with each round shortened by two carbon atoms, which are released as acetyl-CoA, until the entire fatty acid is cleaved into acetyl-CoAs. The complete oxidation of palmitate yields 8 acetyl-CoA, 7 $FADH_2$, 7 NADH, yielding in total 106 ATP molecules [44].

In mitochondria, several enzymes are present for the different steps of β-oxidation, which vary in their chain-length specificity. For the acyl-CoA dehydrogenase (ACAD) four enzymes with overlapping chain-length specificity are known: short-chain acyl-CoA dehydrogenase (SCAD) for C4 and C6 fatty acids, medium-chain acyl-CoA dehydrogenase (MCAD) with high specificity for fatty acids of a chain length of C4 to C12, long-chain acyl-CoA dehydrogenase (LCAD) C8 to C20 fatty acids, which is important for unsaturated fatty acids, and very-long-chain acyl-CoA dehydrogenase (VLCAD) for fatty acids with a chain-length between C12 and C24 [43]. Of the known short-, medium- and long-chain keto-thiolases, only the latter two are important for β-oxidation [43]. Four subunits each of the long-chain enoyl-CoA hydratase / long-chain L-3-hydroxyacyl-CoA dehydrogenase (alpha-subunit) and the long-chain ketothiolase (beta-subunit) are assembled in the hetero-octameric mitochondrial trifunctional protein (MTP), which is bound to the inner face of the inner mitochondrial membrane.

Oxidative phosphorylation

Glycolysis, fatty acid β-oxidation, TCA cycle and the oxidative phosphorylation are tightly coupled processes, as reducing equivalents produced by glycolysis, β-oxidation and TCA cycle directly enter the oxidative phosphorylation. Oxidative phosphorylation is the main source for ATP production. The electrons from the reducing equivalents are transferred onto the respiratory complexes, and are used to reduce molecular oxygen together with protons from the mitochondrial matrix to water. In parallel protons are pumped from the matrix into the intermembrane space, leading to the formation of a pH-gradient and a membrane potential (voltage gradient). Both, the pH-gradient and the membrane potential, build up the electrochemical proton gradient [38]. The respiratory complex V (ATP synthase) drives protons back into the mitochondrial matrix by the electochemical gradient, which as a result generates ATP from ADP. The respiratory chain complexes, complex I - IV, the ATP synthase (complex V), and the adenine nucleotide translocase (ANT) are embedded in the IMM. The complete oxidation of glucose yields 30 ATP molecules, from which alone 26 ATP molecules are generated by oxidative phosphorylation. The complete oxidation of palmitate yields 106 ATP molecules through oxidative phosphorylation [44]. Four enzyme complexes are responsible for the electron flow and at the end for the reduction of oxygen to water.

NADH:ubiquinone-reductase (complex I)

Complex I is the biggest respiratory chain complex and consists of 44 subunits [45]. It needs the flavoprotein FMN and Fe-S-cluster as prosthetic groups. It is localized in the inner mitochondrial membrane in an L-shaped form, where the horizontal arm lies in the inner mitochondrial membrane and the vertical arm protrudes into the mitochondrial matrix. Complex I oxidizes NADH to NAD^+. The reaction leads in parallel to the pumping of four H^+ out of the mitochondrial matrix.

The net reaction is:

$$NADH/H^+ + \text{ubiquinone} + 4\ H^+_{matrix} \rightarrow NAD^+ + \text{ubiquinole} + 4\ H^+_{intermembrane}$$

Succinate:ubiquinone reductase (Complex II):

Complex II is the smallest of the four respiratory complexes and consists of four subunits and equals the succinate dehydrogenase acting in the tricarboxylic acid

cylce. Succinate dehydrogease catalyzes the oxidation of succinate to fumarate, with the formation of a $FADH_2$. Complex II does not pump protons out of the mitochondrial matrix.

The net reaction is:

Succinate + ubiquinone → Fumarate + ubiquinole

During mitochondrial β-oxidation also $FADH_2$ is formed. These electrons are not transferred onto complex II, but onto the electron transfer flavoprotein (ETF), which is reoxidized by the action of ETF:ubiquinone oxidoreductase. The electrons are transferred onto complex III.

Ubiquinole:cytochrome c reductase (complex III):

Complex III consists of 10 subunits and contains as electron carrier cytochrome b, cytochrome c1 and one Fe-S-cluster [46]. Through the transfer of the electrons from ubiquinole to cytochrom c, ubiquinone is reoxidized. The mechanism of the transfer of electrons from ubiquinole to cytochrome c and the coupled transport of protons, is also called the Q cycle [44]. Thereby, in total four protons are pumped into the intermembrane space.

The net reaction is:

$$\text{ubiquinole} + 2\ \text{cyt}\ c_{ox} + 2\ H^+_{matrix} \rightarrow \text{ubiquinone} + 2\ \text{cyt}\ c_{red} + 4\ H^+_{intermembrane}$$

Cytochrome c oxidase (complex IV):

Complex IV consists of 19 subunits and is the final proton pumping complex of the respiratory chain. It catalyzes the electron transport from cytochrome c to elemental oxygen (O_2). For electron transport, complex IV contains the prosthetic groups cytochrome a, cytochrome a_3 and two copper centers. The electron is transferred from cytochrome c to the first copper centre (Cu_A), and via cytochrome a and cytochrome a_3 to the second copper centre (Cu_B). Four molecules of cytochrome c are bound successively to complex IV. In the end, four electrons are transferred onto one molecule O_2, which is then completely reduced to water. In parallel, four protons are pumped into the intermembrane space.

The net reaction is:

$$4\ \text{Cyt}\ c_{red} + 8\ H^{+}_{Matrix} + O_2 \rightarrow 4\ \text{Cyt}\ c_{ox} + 2\ H_20 + 4\ H^{+}_{intermembrane}$$

Through the complexes I, III, and IV protons are pumped from the matrix into the intermembrane space, leading to the formation of the electrochemical proton gradient that drives ATP synthesis.

ATP synthase (complex V):

The ATP synthase consists of 19 subunits, which build two main units, the F_O-unit, which forms a proton channel across the inner mitochondrial membrane and the F_1-unit, which constitutes the catalytic unit of complex V. Protons flow through the F_O-unit down the electrochemical gradient back into the mitochondrial matrix and the F_1-unit catalyzes the reaction from ADP and organic phosphate to ATP. The function of the proton backflow is not the synthesis of ATP, but the release of ATP from the synthase [44]. The mechanism of the ATP synthesis with the F_1-unit is a binding-change mechanism, with three successive steps: the binding of ADP and organic phoshate, the synthesis of ATP and the release of the synthesized ATP from the F_1-unit [44]. The rotation of the γ-subunit of the F_1-unit drives these three steps into each other and is required for the release of the ATP from the F_1-unit. The rotation of the γ-subunit coheres with the rotation caused by the c-subunit of the F_O-unit, through the binding of proton from the proton-rich intermembrane space. The F_O-unit consists of 10 c-subunits and with every binding of a proton to the c-subunit, the subunits are rotated one step further. The c-subunit is firmly connected to the γ-subunit, so the active rotation of the c-subunit also rotates the γ-subunit. With each 360° rotation of the c-units, the γ-subunit comes to a full rotation, which correlates to the binding of 10 protons and leads to the synthesis and release of 3 ATP molecules [44].

The net reaction is:

$$ADP^{3-} + HPO_4^{2-} + 3\ H^{+}_{intermembrane} \rightarrow ATP^{4-} + H_20 + 2\ H^{+}_{matrix}$$

Respiratory chain supercomplexes:

The organization of the respiratory chain complexes within the IMM has been the subject of intense debate [47-52]. The first proposed model was the “solid state model”,

which suggested the arrangement of the respiratory chain complexes in an orderly sequence within the IMM [48]. This model was soon replaced by the “liquid state model”, which hypothesized that the individual respiratoy chain complexes diffuse freely and are randomly distributed within the lipid bilayer [47,49]. Today, based on the ovservations made by Bruet et al. [53], Boumans et al. [54] and Schägger et al. [55] in yeast *S. cerevisiae* and bovine it is believed that the respiratory chain complexes are organized into supercomplexes [52]. The two major supercomplexes in human mitochondria are I_1III_2 and $I_1III_2IV_1$ [56].

3.4.3 Mitochondrial protein import

Of the approximately 1,500 [57] mitochondrial proteins, only 13 are mitochondrially encoded. The remainder is encoded in the nucleus and imported into mitochondria during or after synthesis. These proteins are synthesized as preproteins and may feature either an N-terminal mitochondrial targeting sequence, also called presequence, which is cleaved post-import, or multiple internal mitochondrial targeting sequences. Mitochondrial matrix proteins feature the N-terminal targeting sequences, whereas hydrophobic proteins, which are implemented in the IMM, feature multiple internal targeting signals. In contrast to peroxisomal targeting sequences, mitochondrial targeting sequences do not have a known amino acid sequence, so the import machinery recognizes many different forms of different targeting sequences. The N-terminal presequence of proteins consists of about 20 – 40 amino acids residues, dotted with some positively charged amino acids (lysine, histidine or arginine) [58]. It is suggested that the presequence forms an amphipathic α-helix, with the positively charged amino acids lying on one side of the helix and the hydrophobic amino acids on the other, albeit the latter are not essential for mitochondrial targeting [58]. Hydrophobic proteins do not contain a cleavable N-terminal targeting sequence, but rather contain multiple internal targeting sequences, which are spread over the whole length of the protein. Three major translocase complexes are involved in the import of mitochondrial proteins, one located in the outer mitochondrial membrane, called translocase of the outer membrane (TOM) and two translocases in the inner mitochondrial membrane, called translocases of the inner mitochondrial membrane (TIMs), one for the import of matrix proteins (TIM23) and the other is responsible for the insertion of complexes in the inner membrane

(TIM22). The proteins are transported in an unfolded, linear state or a loop formation through the mitochondrial membranes, and the transport is driven by the membrane potential ($\Delta\psi$), which is built across the inner mitochondrial membrane and the ATP hydrolysis-driven action of the mitochondrial heat shock protein 70 (mtHsp70) [59].

Import of proteins with an N-terminal presequence:

For the import of proteins with a cleavable presequence, the proteins are first located to the OMM, where the presequence is first recognized by TOM20, then transferred to TOM22, TOM5 and translocated in a linear, unfolded state across OMM by the general import pore (GIP), which is formed by the pore-building protein TOM40. The translocation across the OMM is illustrated in Figure 5. In the intermembrane space, the preprotein is bound to the C-terminal end of TOM22 before further transport. The TIM23 protein exposes a domain into the intermembrane space to which the preprotein is bound after the translocation through the OMM. The membrane potential activates the channel formed by the TIM23 complex and exerts and electrophoretic effect on the positively charged presequence, which leads to the transport of the preprotein across the IMM. In the matrix, mtHsp70 binds to the unfolded preprotein in transit and drives the preprotein into the matrix, by the hydrolysis of ATP. The import of preproteins across the IMM is therefore driven by these two energy sources, the mitochondrial membrane potential ($\Delta\psi$) and the ATP hydrolysis-driven action of mtHsp70. In the matrix a mitochondrial processing peptidase removes the presequence and the mature matrix protein is folded. The heterodimeric mitochondrial processing peptidase (MPP) removes the N-terminal presequence proteolytically [59]. The process of translocation across the IMM and the processing in the matrix are shown in Figure 5.

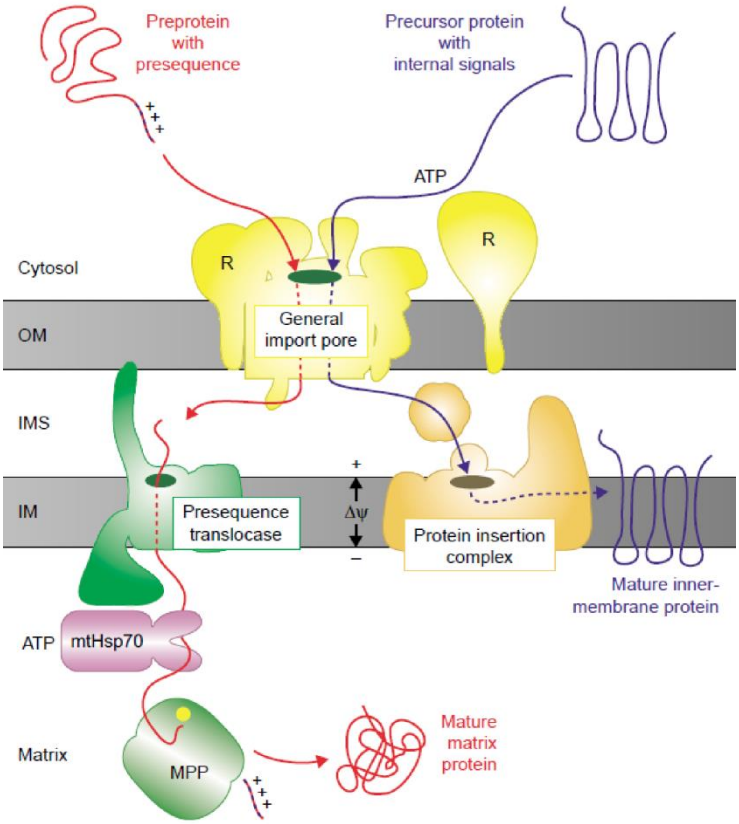

Figure 5: Mitochondrial protein import.

(Figure from Pfanner, N., Wiedemann, N. Mitochondrial protein import two membranes, three translocases. Current opinion in cell biology 2002; 14: 400-11)

Import of proteins with an internal targeting sequence:

Hydrophobic proteins, which feature internal targeting sequences are guided during their transport to the OMM by chaperons to prevent misfolding and aggregation in the aqueous environment. After their transport to the OMM, the internal targeting sequences are recognized by TOM70, which in an ATP-dependent manner transports the preprotein to TOM22 and TOM5, before the preprotein is translocated across the OMM by the GIP in a loop formation (Figure 5). Subsequent to the translocation across the OMM, the protein binds to the TIM9-TIM10-complex in a loop formation, which has chaperone-like characteristics, to prevent the aggregation and misfolding of proteins with internal targeting sequences. The TIM9-TIM10 complex then transports the protein across the intermembrane space to the IMM and binds to the TIM22 complex. The subsequent import of the protein into the IMM is carried out by the TIM22 complex, consisting of TIM22, TIM54 and TIM18, which is activated by the presence of a targeting signal. The mitochondrial membrane

potential ($\Delta\psi$) is the only energy source during this process. The schematic illustration of the transport and insertion at the IMM is shown in Figure 5.

3.5 Peroxisomes

3.5.1 Structure and Function

Peroxisomes are small spherical organelles, which are between 0.1 - 1 µm in diameter and are surrounded by a single membrane [60]. Peroxisomes are present in all eukaryotic cells and compared with mitochondria do not contain DNA or ribosomes, i.e., all peroxisomal proteins are encoded in the nucleus and have to be transported into the peroxisomes. Rhodin was the first to describe peroxisomes in 1954. He termed them microbodies [61], and later on the term peroxisome was used. Peroxisomes and mitochondria are replicated by the fission of already present peroxisomes or mitochondria, respectively. The important functions of peroxisomes are oxidation and detoxification metabolism, synthesis of plasmalogen and oxidation of fatty acids via α- and β-oxidation.

Oxidation fatty acids via α- and β-oxidation:

In plants cells, yeast and most fungal cells β-oxidation of fatty acids take place only in peroxisomes, whereas in mammalian cell the β-oxidation of fatty acids take place in both mitochondria and peroxisomes. Peroxisomes and mitochondria both have their own sets of enzymes for fatty acid β-oxidation, where peroxisomes are responsible for the shortening of very-long-chain fatty acids, medium- and long-chain dicarboxylic acids, bile acid precursors, branched chain fatty acids, prostaglandins, leukotrienes, xenobiotics and certain mono- and polyunsaturated fatty acids [40,62] and mitochondria are responsible for the oxidation of short-, medium- and long-chain fatty acids. The shortened fatty acids acyl-CoAs from the peroxisomes are exported to the mitochondria for complete oxidation, because the mitochondrial fatty acid β-oxidation is more efficient concerning energy generation. The enzymes for peroxisomal β-oxidation are distributed within the peroxisomal matrix. Only saturated very-long-chain fatty acids and 2-methyl-branched fatty acids can be directly activated and are available for peroxisomal β-oxidation. All other fatty acids have to be converted via different peroxisomal enzymes into suitable substrates for peroxisomal β-oxidation (Figure 6).

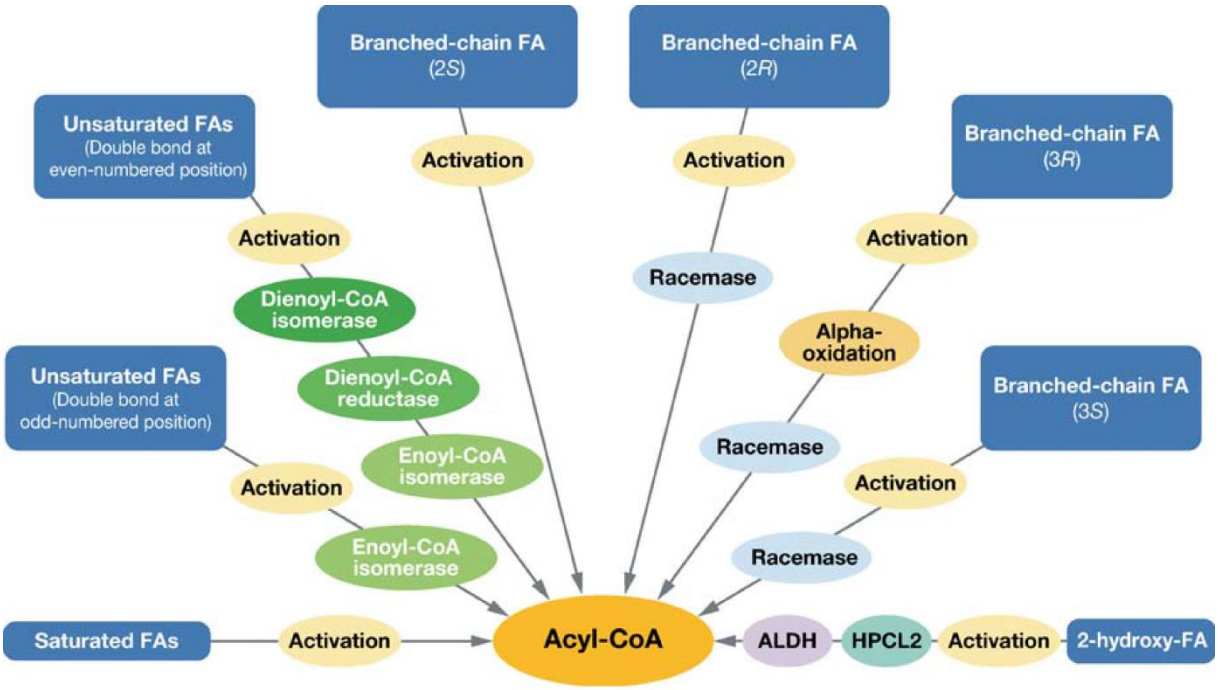

Figure 6: Enzymatic conversion of different fatty acids to their corresponding acyl-CoA, before the oxidation via peroxisomal β-oxidation.

(Figure from Wanders, R.J. Waterham, H.R. Biochemistry of mammalian peroxisomes revisited. Annu Rev Biochem 2008; 75: 295-332.)

After the transport of the activated acyl-CoAs across the peroxisomal membrane or the conversion into suitable substrates, the acyl-CoA chain is shortened by the repeated action of four enzymatic reactions (Figure 7). The first reaction is an oxidation by an acyl-CoA oxidase (ACOX) to form enoyl-CoA and H_2O_2, hydration of the double bond by the action of enoyl-CoA hydratase to from 3-hydroxyacyl-CoA, again an oxidation to from 3-ketoacyl-CoA and NADH and H^+ by the action of 3-hydroxyacyl-CoA dehydrogenase and in the last step the thiolytic cleavage of 3 ketoacyl-CoA to form an acetyl-CoA and an acyl-CoA chain shortened by two carbons. As in peroxisomes the electrons from FAD^+, which is bound to the ACOX, cannot be passed directly into respiratory chain, the electrons are directly transferred onto O_2 to from H_2O_2, and the chemical energy dissipated as heat by the action of catalase. The second and the third reaction of peroxisomal β-oxidation is catalyzed by a bifunctional protein, where in peroxisomes two types of bifunctional enzymes are present, the L-bifunctional enzyme and the D-bifunctional enzyme. The L-bifunctional

enyzme, also called EHHADH, forms and dehydrates L-3-hydroxyacyl-CoA, whereas the D-bifunctional enzyme forms and dehydrates D-3-hydroxyacyl-CoA [62].

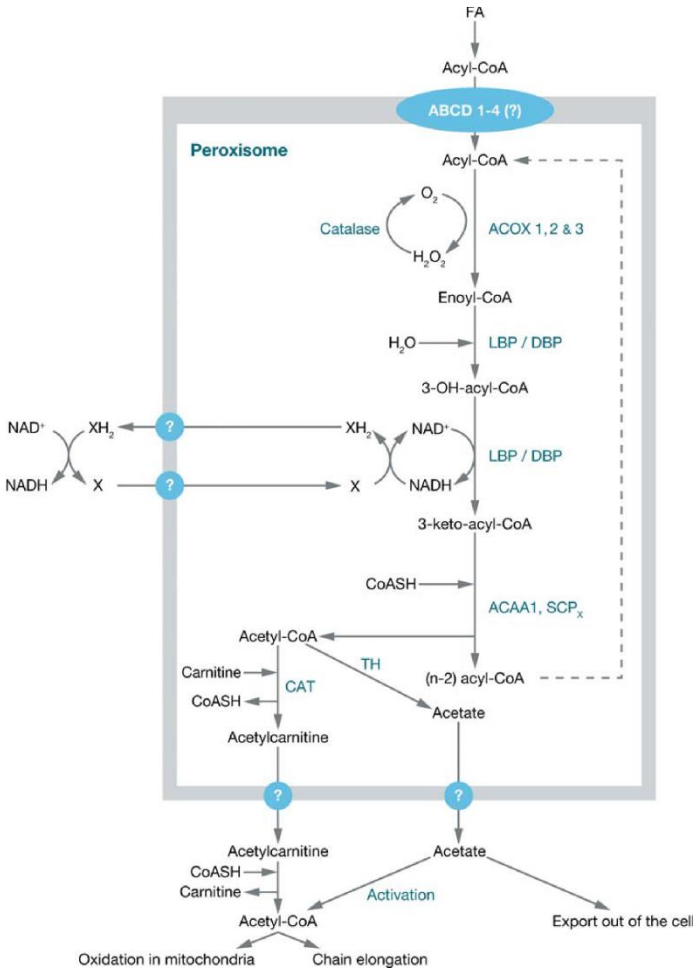

Figure 7: Schematic representation of peroxisomal β-oxidation.

(Figure from Wanders, R.J. Waterham, H.R. Biochemistry of mammalian peroxisomes revisited. Annu Rev Biochem 2008; 75: 295-332.)

The D-bifunctional enyzme is the main enzyme involved in the oxidation of polyunsaturated fatty acid and branched-chain fatty acids, whereas L-bifunctional enzyme (EHHADH) is mainly involved in the oxidation of straight-chain enyl-CoAs [62]. EHHADH features the enzymatic acitivities of enoyl-CoA hydratase and L-3-hydroxyacyl-CoA dehydrogenase. As already mentioned, the acyl-CoAs are not completely oxidized in peroxisomes, but shortened and subsequently transported over the peroxisomal carnitine acyltransferase as acylcarnitines into the mitochondria for complete oxidation.

Peroxisomal α-oxidation of fatty acids takes place whenever the Cβ is blocked by a methyl group and cannot be oxidized by β-oxidation. The fatty acid is then oxidized by α-oxidation (Figure 8), until the methyl-group no longer blocks the Cβ. The main substrate for α-oxidation is phytanic acid and after the first round the resulting pristanic acid is further oxidized by peroxisomal β-oxidation. First of all, phytanic acid is activated to the corresponding phytanoyl-CoA by an acyl-CoA synthase. The three steps from phytanoyl-CoA to pristanic acid are catalyzed by the enzymes phytanoyl-CoA 2-hydroxylase, 2-OH-phytanoyl-CoA lyase and pristanal dehydrogenase.

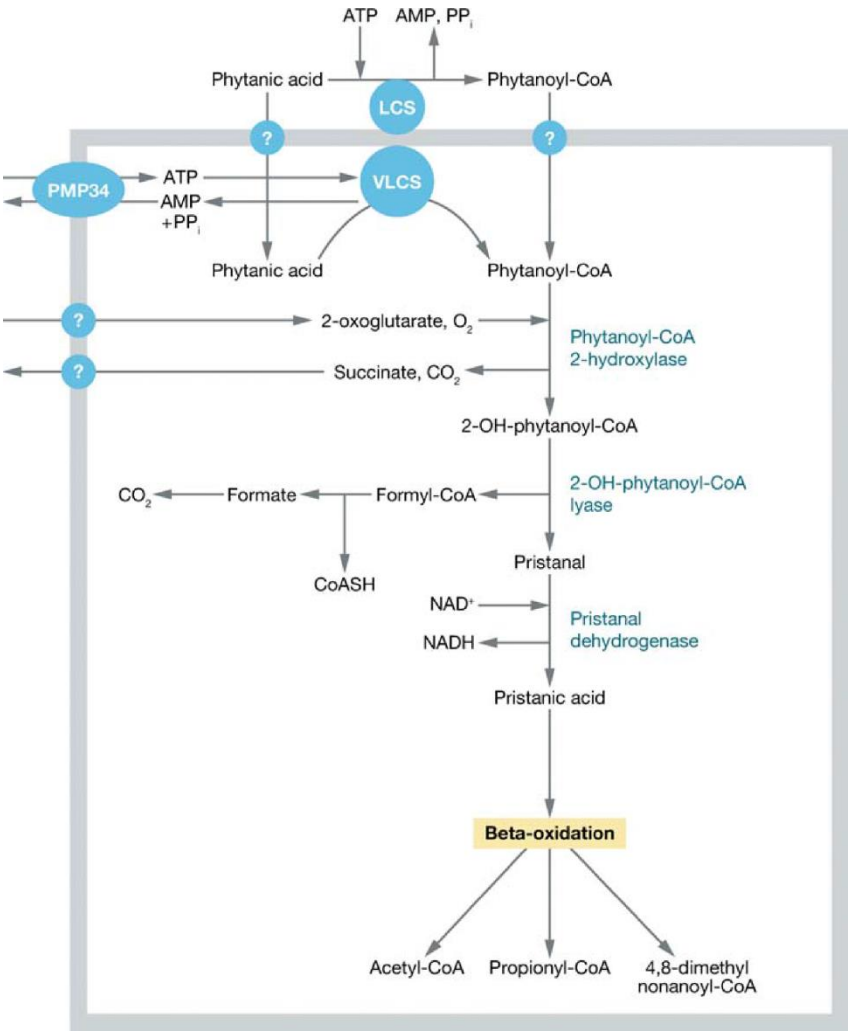

Figure 8: Peroxisomal α-oxidation of phytanic acid.

(Figure from Wanders, R.J. Waterham, H.R. Biochemistry of mammalian peroxisomes revisited. Annu Rev Biochem 2008; 75: 295-332.)

3.5.2 Peroxisomal protein import

As peroxisomes do not contain their own DNA, all proteins are encoded in the nucleus and are subsequently imported into the peroxisomes. The import of proteins into the peroxisomal matrix differs from the that of other organelles such as mitochondria or chloroplasts, as peroxisomes are capable of importing both fully folded and oligomeric proteins [60]. A schematic representation of peroxisomal protein import is shown in Figure 9. Peroxisomal proteins are synthesized with either peroxisomal targeting sequence type 1 (PTS1) or type 2 (PTS2). The majority of peroxisomal proteins carries the PTS1, a C-terminal tripeptide with the sequence SKL or variants thereof in the form of (S/A/C)-(K/R/H)-(L/A) [60]. A smaller number of proteins feature carries either in addition to PTS1 or solely the PTS2, which is a nona-peptide located within the first 20 amino acids of the N-terminus and exhibits a sequence of the type (R/K)-(L/V/I/Q)-XX-(L/V/I/H/Q)-(L/S/G/A/K)-X-(H/Q)-(L/A/F) [60]. As the majority of peroxisomal matrix proteins feature a PTS1 sequence, in the following only the import pathway of proteins featuring a PTS1 targeting sequence is described in detail.

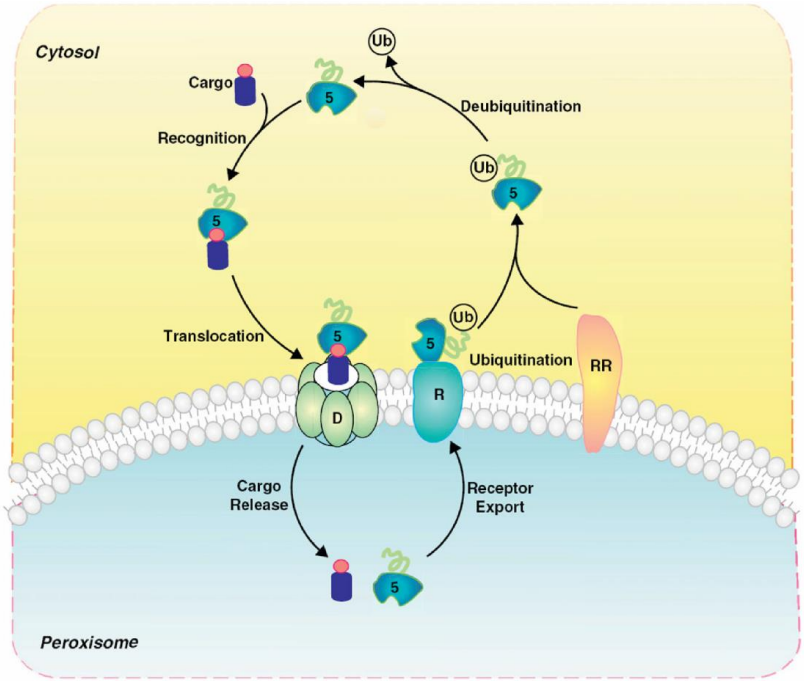

D = docking complex; R = Ring-peroxin complex; 5 = Pex5p; RR = AAA-complex; Cargo = peroxisomal protein; Ring associated with the Cargo = peroxisomal targeting sequence;

Figure 9: Schematic figure of peroxisomal protein import.

(Figure from Liu, S., Ma, C., Subramani, S., Recent advances in peroxisomal matrix protein import. Current opinion in cell biology 2012; 24: 484-9.)

The import of peroxisomal proteins can be divided into five steps, first the recognition of the peroxisomal protein by the receptor in the cytosol, the docking of the receptor-protein complex at the peroxisomal membrane, the subsequent translocation of the complex through the peroxisomal membrane, the release of the protein into the peroxisomal matrix and in the last step the recycling of the receptor. The receptor responsible for the recognition of the PTS1 is called Pex5p. Upon docking, the receptor-protein complex is translocated to the peroxisomal membrane, where it interacts with the docking complex composed of Pex13p and Pex14p, where Pex14p is the initial binding partner of the protein-receptor-complex [60]. The mechanism by which fully folded and oligomeric proteins are translocated across the peroxisomal membrane is not well understood, but over the last few years the model of a transient opened import pore has been favoured [60]. In the peroxisomal matrix the receptor and protein are dissociated and, afterwards, the receptor is recycled and a subset of imported proteins is processed by the peroxisomal protease Tysnd1. The receptor is at the peroxisomal membrane ubiquitinilated, which occurs at the N-terminal end at a conserved cysteine residue (C11), before the export. Before the next round of import and export, the ubiquitinated receptor must be deubiquitinated in the cytosol, by the action of USP9X, an ubiquitin hydrolase. The translocation of the receptor-protein complex across the peroxisomal membrane and the export of the ubiquitinated receptor are coupled by the so-called export-driven-import model. This means, that the persence of an ATP hydrolysis-driven export of the ubiquitinated receptor is a requirement for the import of the receptor-protein complex.

3.6 Enoyl-coenzyme A hydratase / L-3-hydroxyacyl-coenzyme A dehydrogenase (EHHADH)

The gene *EHHADH* is localized on the chromosome 3q26.3 – 3q28. The cDNA sequence extends over 3779 nucleotides [63] and encodes for the peroxisomal protein Enoyl-CoA hydratase / L-3-hydroxyacyl-CoA dehydrogenase (EHHADH). EHHADH gene expression is the highest in liver and kidney [63]. The C-terminal end of the protein features the typical peroxisomal targeting sequence SKL. Hence, EHHADH is exclusively localized in the peroxisomal matrix. EHHADH is imported without further processing and features a molecular weight of 79 kDa and a pI of 9.8 [64]. EHHADH is involved in peroxisomal fatty acid β-oxidation, catalyzing the second and third step,

namely hydration and NAD^+-dependent dehydrogenation. Therefore, it is also called peroxisomal L-bifunctional protein. Hydration and NAD^+-dependent dehydrogenation can also be catalyzed by the D-bifunctional protein Hsd17b4. Qi et al. [65] showed that the existence of a knockout mouse of $EHHADH^{-/-}$, did not lead to a phenotype and changes in lipid metabolism, which further support the fact, that Hsd17b4 can handle all peroxisomal substrates. As opposed to this, Houten et al. [66] reported recently that EHHADH is essential for peroxisomal ß-oxidation of long-chain dicarboxylic acid (DCAs) to medium-chain DCAs such as adipic (C6-DCA) and suberic acid (C8-DCA). Houten et al. could clearly show that the formation of long-chain DCAs are disturbed in $EHHADH^{-/-}$ knockout mouse after fasting and thereby demonstrate that EHHADH plays an essential role in the formation of fasting-induced medium-chain DCAs and their carnitine esters[66]. In addition, it is also shown that Hsd17b4 could not compensate for this EHHADH deficiency.

4 Aim of this work

The causes for development of renal Fanconi´s syndromes are diverse, and the renal Fanconi´s syndrome is still subject of intense research with all it is different inherited and acquired forms.

Recently, Kleta and coworkers [67] identified a novel form of an isolated autosomal dominant renal Fanconi´s syndrome in an extended family with eleven affected members. The causative mutation was mapped to chromosome 3q27 with an LOD > 3 via multipoint parametric linkage analysis, with the haplotype shared by all affected family members, whereas it was not found in any of the unaffected family members. The respective gene encodes for the peroxisomal protein EHHADH (Enoyl-CoA hydratase/3-Hydroxyacyl-CoA dehydrogenase), which is involved in β-oxidation of very long-chain fatty acids. The C-terminus of the protein features the typical peroxisomal targeting sequence SKL. Upon mutation, a negatively charged glutamic acid residue is exchanged for a positively charged lysine in the very N-terminus, leading to the heterozygous missense mutation p.E3K. As knock-out mice (L-EHHADH$^{-/-}$) did not show a phenotype, this mutation of EHHADH shows a dominant negative effect and leads to the monogenic disorder of Fanconi´s syndrome. The primary aim of this study is the elucidation of the molecular consequences caused by EHHADH mutation, thus facilitating the analysis of the respective pathomechanism.

The working hypothesis is that mistargeting of $EHHADH_{MUT}$ into mitochondria upon mutation leads to an interference of $EHHADH_{MUT}$ with members of the mitochondrial energy metabolism. This impairment leads to the development of a mitochondriopathy causing diminished energy supply, which in turn causes the observed Fanconi´s syndrome

I will investigate the impact of the *EHHADH* mutation in LLC-PK1 cells, a cell line of proximal tubule cells of porcine origin, which have been transfected with either inducible $EHHADH_{WT}$ or $EHHADH_{MUT}$ using the TetOn-system. In a first step, it has to be shown that mistargeting of EHHADH into mitochondria indeed occurs upon mutation. Subsequently, possible interaction partners of $EHHADH_{MUT}$ will be identified by co-immunoprecipitation against EHHADH from isolated mitochondria. Additionally, quantitative differential proteome analyses will be accomplished. The results will give a first hint on possible impaired energy metabolism pathways. These

analyses will be complemented by metabolomic measurements of the metabolic state of the cells to show diminished energy supply within the cells and verify the reduced throughput in the affected pathways identified by the proteomic analyses Furthermore, functional analyses will be used to determine the impact of $EHHADH_{MUT}$ on mitochondrial energy production in more detail. Thereby, I aim to elucidate the underlying molecular mechanisms of this novel Fanconi´s syndrome.

5 Materials and Methods

5.1 Material

5.1.1 Cell line

The porcine kidney proximal tubule cell line LLC-PK1 was used for all cell experiments. This cell line had been transfected stably by our cooperation partner R. Kleta at the University College London with either $EHHADH_{WT}$ or $EHHADH_{MUT}$ cDNA using the inducible Tet-on gene expression system. The LLC-PK1 cell line is an adherent cell line.

5.1.2 Media

Routine cell culture medium:	500 mL Memα + 10 % FCS (heat-inactivated) + 2 mM L-glutamine, 1 mM sodium pyruvate + 0.5% penicillin/streptomycin
Stimulation medium 1:	500 mL RPMi 1640 (without glucose) + 10 % FCS (heat inactivated) + 2 mM L-glutamine + 0.5% penicillin/streptomycin + 5 mM caproic acid
Stimulation medium 2:	500 mL RPMI 1640 (without glucose) + 10 % FCS (heat inactivated) + 2 mM L-glutamine + 0.5% penicillin/streptomycin + 0.5 mM L-carnitine + 0.3 mM palmitic acid bound to BSA

5.1.3 Buffers and Solutions

5.1.3.1 Cell culture

Mitochondria isolation buffer	250 mM Sucrose, 1 mM EDTA, 10 mM MOPS, pH 7.2
Ringer solution	5 mM HEPES, 1.45 M NaCl, 1.6 mM K_2HPO_4, 0.4 mM KH_2PO_4, 5 mM glucose, 1 mM $MgCl_2$, 1.3 mM $CaCl_2$, pH 7.4

5.1.3.2 Two-dimensional gel electrophoresis

Acrylamide gel (10%)	16.5 mL Acrylamide solution 30 % (37.5:1), 12.5 mL 1.5 M Tris- HCl pH 8.8, 0.5 mL 10 % SDS solution, 0.5 mL 10 % APS solution, 0.085 mL 10 % TEMED solution, 20 mL A. bidest.
Agarose solution	0.5 % agarose in 25 mL anode buffer
Anode buffer	SDS running buffer (1x)
Bromophenol blue (1%)	50 mM Tris, 1 % bromophenol blue
Cathode buffer	SDS running buffer (2x)
DIGE stop solution	10 mM lysine
Labeling buffer	7 M urea, 2 M thiourea, 2 % CHAPS, 30 mM Tris-Base
Rehydration buffer	7 M urea, 2 M thiourea, 2 % CHAPS, 50 µl bromophenol blue 1 %
Rehydration solution	500 µL rehydration buffer + 10 µl IPG-Puffer pH 7-11 + 12.5 µl DeStreak
SDS equilibration buffer	50 mM Tris-HCl pH 8,8, 30 % glycerol (99 %), 6 M urea, 0,002 % bromophenol blue, 2 % SDS
SDS running buffer (10x)	250 mM Tris, 1,92 M glycine, 1 % SDS

5.1.3.3 Immunoblotting analysis

NativePAGE™ Running Buffer (1x)	50 mM BisTris, 50 mM Tricine pH 6.8
Coomassie Brilliant Blue	0.165 g Coomassie G-250, 85 mL methanol, 5.8 mL phosphoric acid, 42.5 g ammonium sulfate, filled up to 250 mL with deionized water
Dark blue cathode buffer	10 mL NativePAGE™ Running Buffer (20x), 10 mL NativePAGE™ Cathode Additive, filled up to 180 mL with deionized water
Digitonin solution	20 % digitonin in deionized water
Light blue cathode buffer	10 mL NativePAGE™ Running Buffer (20x), 1 mL NativePAGE™ Cathode Additive, filled up to 189 mL with deionized water
TBS-T	10 mM Tris-HCl, pH 7.4; 150 mM NaCl; 0.02% Tween 20

5.1.3.4 SERVA Purple protein stain

Solution 1	850 mL deionized water, 10 g citric acid, 150 mL ethanol
Solution 2	1 L deionized water, 6.2 g boric acid, 3.85 g NaOH; pH > 9.4
Solution 3	850 mL deionized water, 150 mL ethanol

5.1.3.5 LC-MS/MS for metabolic analysis

Solvent A	0.1 % acetic acid and 0.025 % HFBA in water
Solvent B	0.1 % acetic acid, 0.025 % HFBA, in acetonitrile

5.1.3.6 High-resolution respirometry

Mitochondria respiration medium (MiR05)	0.5 M EGTA, 3mM $MgCl_2 \cdot 6H_20$, 60 mM potassium lactobionate, 20 mM taurine, 10 mM KH_2PO_4, 20 mM HEPES, 110 mM sucrose, 1 g/L BSA, pH 7.1

5.1.3.7 LC-MS/MS for proteomic analysis

Solvent A	0.1% formic acid in water
Solvent B	0.1% formic acid in acetonitrile

5.1.4 Antibodies

Primary antibody	**Supplier**	**Dilution**
Custom-made Anti-EHHADH rabbit polyclonal IgG Epitope: EPSDYLRRLVAQGSPPLK	Davids Biotechnologie GmbH, Regensburg, Germany	1 : 1,000 1 : 1,250
Anti-HADHB	Santa Cruz Biotechnolgy, Heidelberg, Germany	1 : 200
Anti-HADHA	Santa Cruz Biotechnolgy, Heidelberg, Germany	1 : 1,000
Anti-EHHADH antibody (ab93172)	Abcam plc, Cambridge, United Kingdom	1 : 160

Secondary antibody	Supplier	Dilution	Modification
Alexa Fluor® 488 goat anti-rabbit	Invitrogen, Karlsruhe, Germany	1 : 400	Alexa Fluoro® 488
ECL Rabbit IgG, HRP-linked whole antibody from donkey	GE Healthcare Europe GmbH, Munich, Germany	1 : 4,500	HRP conjugated
ECL Mouse IgG, HRP-linked whole antibody from sheep	GE Healthcare Europe GmbH, Munich, Germany	1 : 4,500	HRP conjugated
Bovine anti-goat IgG-HRP conjugated	Santa Cruz Biotechnolgy, Heidelberg, Germany	1 : 2,500	HRP conjugated

5.1.5 Kits, turnkey solution, marker

10 % DDM solution	Invitrogen GmbH, Darmstadt, Germany
Amersham ECL Plus ™ Western Blotting Detection Reagents	GE Healthcare Europe GmbH, Munich, Germany
Amersham ECL Plus™ Western Blotting Detection Reagents	GE Healthcare Europe GmbH, Munich, Germany
ATP Colorimetric/Fluorometric Assay Kit	BioVision Inc., Milpitas, CA, USA
Casy®ton electrolyte	Roche Diagnostics Deutschland GmbH, Mannheim, Germany
DeStreak	GE Healthcare Europe GmbH, Freiburg, Germany
Fetal Bovine Serum Gold	GE Healthcare Europe GmbH, Freiburg, Germany
Fluorescence mounting medium	Dako Deutschland GmbH, Hamburg, Germany
FluoroProfile Kit	Sigma-Aldrich Chemie GmbH, Taufkirchen, Germany
HOE33342 (Stockkonz.: 5x10-4 M); Dilution 1 : 400	Invitrogen, Karlsruhe, Germany
Hygromycine B solution	Merck KGaA, Darmstadt, Germany
IPG-Buffer pH 7-11	GE Healthcare Europe GmbH, Munich, Germany
L-glutamine	PAN Biotech GmbH, Aidenbach, Germany
MassChrom® internal standard labeled amino acids and acylcarnitines	Chromsystems Instruments & Chemicals GmbH, Gräfelfing, Germany
MEM alpha medium	GE Healthcare Europe GmbH, Freiburg, Germany
MitoTracker® Orange	Invitrogen, Eugene, Oregon USA
NativePAGE™ Cathode Additive (20x)	Invitrogen GmbH, Darmstadt, Germany
NativePAGE™ Running Buffer (20x)	Invitrogen GmbH, Darmstadt, Germany
NativePAGE™ sample buffer	Invitrogen GmbH, Darmstadt, Germany
NuPAGE® Antioxidant	Invitrogen GmbH, Darmstadt, Germany
NuPAGE® LDS sample buffer (4x)	Invitrogen GmbH, Darmstadt, Germany
NuPAGE® MOPS SDS Running Buffer (20x)	Invitrogen, Karlsruhe, Germany
NuPAGE® Transfer Buffer (20x)	Invitrogen, Karlsruhe, Germany
PBS buffer	Sigma-Aldrich Chemie GmbH, Taufkirchen, Germany
Penicillin/streptomycin	PAN Biotech GmbH, Aidenbach, Germany
Phosphatase Inhibitor Cocktail 2	Sigma-Aldrich Chemie GmbH, Taufkirchen, Germany

Pierce® Protein A/G Magnetic IP/Co-IP Kit	Thermo Fisher Scientific, Bonn, Germany
Ponceau staining ready-to-use solution	Carl Roth GmbH + Co KG, Karlsruhe, Germany
Proteinase Inhibitor Cocktail	Sigma-Aldrich Chemie GmbH, Taufkirchen, Germany
Refraction-2D Labeling kit	NH DyeAGNOSTICS GmbH, Halle, Germany
RotiBlock®	Carl Roth GmbH + Co KG, Karlsruhe, Germany
RPMI 1640 without L-glutamine	PAN Biotech GmbH, Aidenbach, Germany
RPMI 1640 without L-glutamine and glucose	PAN Biotech GmbH, Aidenbach, Germany
SERVA Purple protein stain	SERVA Electrophoresis GmbH, Heidelberg, Germany
Tetracycline solution	Bioline GmbH, Luckenwalde, Germany
Trypsin	Promega GmbH, Mannheim, Germany
Trypsin-EDTA	PAN Biotech GmbH, Aidenbach, Germany

5.1.6 Consumable Material

1.5-mL and 2-mL Eppendorf microcentrifuge tube	VWR International GmbH, Darmstadt, Germany
10-kDa spin column	Pall GmbH, Dreieich, Germany
15 mL and 50 mL Röhrchen	Greiner Bio-One GmbH, Frickenhausen, Germany
96-well microplate	Greiner Bio-One GmbH, Frickenhausen, Germany
Axxygen® Microcentrifuge Tube 0.7 mL	Fisher Scientific GmbH, Schwerte, Germany
CASY® cups	Roche Diagnostics Deutschland GmbH, Mannheim, Germany
Cell culture flask	Greiner Bio-One GmbH, Frickenhausen, Germany
Cell scraper	Techno Plastic Products AG, Trasadingen, Switzerland
Cover glasses, 24 mm diameter	VWR International GmbH, Darmstadt, Germany
Immobiline™ DryStrip pH	GE Healthcare Europe, München, Germany
Myco Trace	PAA Laboratories, Cölbe, Deutschland
NativePAGE™ 3-12% Bis-Tris gel	Invitrogen GmbH, Darmstadt, Germany
NativePAGE™ 4-16% Bis Tris gels	Invitrogen GmbH, Darmstadt, Germany
NuPAGE® Novex® 12% Bis Tris 2D well gel	Invitrogen GmbH, Darmstadt, Germany
NuPAGE® Novex® 4-12% Bis-Tris protein gel	Invitrogen GmbH, Darmstadt, Germany
ProteoGel™ IPG Strip, 7 cm, pH 8-11 linear	Sigma-Aldrich Chemie GmbH, Munich, Germany
PVDF membrane Immobilon P	Merck Millipore GmbH, Schwalbach, Germany
Sample cups	GE Healthcare Europe, München, Germany
Sterile syringe filter 0.45 µm and 0.2 µm	VWR International GmbH, Darmstadt, Germany
Whatman® Paper	Biometra, Göttingen, Germany

LC columns

SLB-IL59 column (30 m x 0.25 mm inner diameter, 0.2 µm film thickness)	Supelco, Belafonte, PA, USA
Acclaim PepMap column (75 µm I.D. x 25 cm, 3 µm, C18)	Dionex, Idstein, Germany
Atlantis T3 (3 µm, 2.1 mm i.d. x 150 mm) reversed phase column	Waters, Eschborn, Germany
Acclaim PepMap Precolumn (100 µm I.D. x 2 cm, 5 µm, C18)	Dionex, Idstein, Germany

5.1.7 Chemicals

1,4-dithio-D-threitol (DTT)	Sigma-Aldrich Chemie GmbH, Munich, Germany
Acetic acid, LC-MS grade	Sigma-Aldrich Chemie GmbH, Munich, Germany
Acetonitrile, LC-MS grade	Fisher Scientific GmbH, Schwerte, Germany
Acetyl coenzyme A lithium salt	Sigma-Aldrich Chemie GmbH, Munich, Germany
Acrylamide 4K-Lösung 37.5:1 (30%)	AppliChem, Darmstadt, Germany
Adenosine 5 diphosphate monopotassium salt dihydrate from bacterial source	Sigma-Aldrich Chemie GmbH, Munich, Germany
Agarose, low-melting	Bio-Rad Laboratories GmbH, Munich, Germany
Ammonium persulfate	Carl Roth GmbH + Co KG, Karlsruhe, Germany
Ammoniumsulfate	Merck KGaA, Darmstadt, Germany
Antimycin A from Streptomyces sp.	Sigma-Aldrich Chemie GmbH, Munich, Germany
Boric acid	SERVA Electrophoresis GmbH, Heidelberg, Germany
Bovine serum albumin	Sigma-Aldrich Chemie GmbH, Munich, Germany
Bovine serum albumin, fatty acid free	GE Healthcare Europe GmbH, Freiburg, Germany
Bromophenol blue	GE Healthcare Europe GmbH, Freiburg, Germany
$CaCl_2$	Sigma-Aldrich Chemie GmbH, Munich, Germany
Caproic acid	Sigma-Aldrich Chemie GmbH, Munich, Germany
CHAPS	AppliChem, Darmstadt, Germany
Citric acid	SERVA Electrophoresis GmbH, Heidelberg, Germany
Coomassie Brilliant Blue G-250	Sigma-Aldrich Chemie GmbH, Munich, Germany

Cytochrome C from Horse Heart	Sigma-Aldrich Chemie GmbH, Munich, Germany
Digitonin	Sigma-Aldrich Chemie GmbH, Munich, Germany
Dimethyl sulfoxide (DMSO)	Sigma-Aldrich Chemie GmbH, Munich, Germany
DTNB	Sigma-Aldrich Chemie GmbH, Munich, Germany
EDTA, Disodium salt Dihydrat	Carl Roth GmbH + Co KG, Karlsruhe, Germany
EGTA	Sigma-Aldrich Chemie GmbH, Munich, Germany
Ethanol p.a.	J.T. Baker, Deventer, Netherlands
FCCP	Sigma-Aldrich Chemie GmbH, Munich, Germany
Formic acid p.a.	Sigma-Aldrich Chemie GmbH, Munich, Germany
Glucose	Carl Roth GmbH + Co KG, Karlsruhe, Germany
Glycerol	AppliChem, Darmstadt, Germany
Glycine	Merck KGaA, Darmstadt, Germany
HEPES	Sigma-Aldrich Chemie GmbH, Munich, Germany
HFBA	Sigma-Aldrich Chemie GmbH, Munich, Germany
Iodoacetamide	Sigma-Aldrich Chemie GmbH, Munich, Germany
K_2HPO_4	Merck KGaA, Darmstadt, Germany
KH_2PO_4	Carl Roth GmbH + Co KG, Karlsruhe, Germany
L-ascorbic acid	Sigma-Aldrich Chemie GmbH, Munich, Germany
L-carnitine	Sigma-Aldrich Chemie GmbH, Munich, Germany
L-lysine	Sigma-Aldrich Chemie GmbH, Munich, Germany
Malic acid	Sigma-Aldrich Chemie GmbH, Munich, Germany
Methanol	VWR International GmbH, Darmstadt, Germany
$MgCl_2*6H_20$	Sigma-Aldrich Chemie GmbH, Munich, Germany
MOPS	AppliChem, Darmstadt, Germany
NaCl	Merck KGaA, Darmstadt, Germany
NaOH	Merck KGaA, Darmstadt, Germany
NaOH pellets	SERVA Electrophoresis GmbH, Heidelberg, Germany
Oligomycin	Sigma-Aldrich Chemie GmbH, Munich, Germany
Oxaloacetic acid	Sigma-Aldrich Chemie GmbH, Munich, Germany
Palmitic acid	Sigma-Aldrich Chemie GmbH, Munich, Germany

Palmitoylcarnitine	Sigma-Aldrich Chemie GmbH, Munich, Germany
Palmitoyl-CoA	Sigma-Aldrich Chemie GmbH, Munich, Germany
Paraformaldehyde	Sigma-Aldrich Chemie GmbH, Munich, Germany
Ortho-phosphoric acid	Merck KGaA, Darmstadt, Germany
Potassium lactobionate	Sigma-Aldrich Chemie GmbH, Munich, Germany
Rotenone	Sigma-Aldrich Chemie GmbH, Munich, Germany
SDS	Carl Roth GmbH + Co KG, Karlsruhe, Germany
Skimmed milk powder	Carl Roth GmbH + Co KG, Karlsruhe, Germany
Sodium pyruvate	Sigma-Aldrich Chemie GmbH, Munich, Germany
Succinic acid	Sigma-Aldrich Chemie GmbH, Munich, Germany
Sucrose	Sigma-Aldrich Chemie GmbH, Munich, Germany
Taurine	Sigma-Aldrich Chemie GmbH, Munich, Germany
TEMED	GE Healthcare Europe GmbH, Freiburg, Germany
TMPD	Sigma-Aldrich Chemie GmbH, Munich, Germany
Tris	USB Corporation, Cleveland, OH USA
Tris-HCl	Carl Roth GmbH + Co KG, Karlsruhe, Germany
Trition X-100	Sigma-Aldrich Chemie GmbH, Munich, Germany
Tween 20	Merck KGaA, Darmstadt, Germany
Urea	GE Healthcare Europe GmbH, Freiburg, Germany

5.1.8 Devices

4000 Qtrap® LC/MS/MS System	AB SCIEX GmbH, Framingham, MA, USA
Agilent 1200 SL HPLC system	Böblingen, Germany
Agilent model 6890 GC with a Mass Selective Detector (MSD) model 5975 Inert XL	Agilent, Palo Alto, CA, USA
Amersham Biosciences Ultrospec 3100 pro	GE Healthcare Europe GmbH, Munich, Germany
Autoklav Systec VX-55	Systec, Wettenberg, Germany
Bandelin Sonorex Ultraschallbad	Schalltec, Mörfelden-Walldorf, Germany
Bio-Rad VersaDoc Imaging System 4000 MP	Bio-Rad Laboratories GmbH, Munich,Germany
CASY® TT Cell Counter + Analyzer	Schärfe System GmbH, Reutlingen, Germany
Concentrator 5301	Eppendorf, Hamburg, Germany
ECL Semi-Dry Tranfer Unit TE 77	GE Healthcare Europe GmbH, Munich, Germany
Ettan™ IPGphor™ 3 IEF System	GE Healthcare Europe, München, Germany
Fluorostar Optima microplate reader	BMG Labtech GmbH, Ortenberg, Germany
Heraeus® HERAcell 240 CO_2 Inkubator	Thermo Fisher Scientific, Langenseldbold, Germany
Heraeus® HERAsafe HSP12	Thermo Fisher Scientific, Langenseldbold, Germany
Heraeus® Multifuge3S-R	Thermo Fisher Scientific, Langenseldbold, Germany
Micromax RF Microcentrifuge	Thermo Fisher Scientific, Langenseldbold, Germany
Oroboros-2k Oxygraph	OROBOROS Instruments, Innsbruck, Austria
pH meter Lab 850	SI Analytics, Mainz, Germany
Purelab plus	USF Deutschland, Ransbach-Baumbach, germany
Qstar XL MS/MS System	AB SCIEX Germany GmbH, Darmstadt, Germany
Shaker Rotamax 120	Heidolph, Schwabach, Germany
Shaker with tumbling motion 3012	Gesellschaft für Labortechnik, Burgwedel, Germany
TripleTOF® 5600+ System	AB SCIEX Germany GmbH, Darmstadt, Germany
Ultimate3000 nano-RP-HPLC-system	Dionex, Idstein, Germany
vacuum evaporator	CombiDancer, Hettich AG, Bäch, Switzerland
Wilovert S inverse microscope with phase contrast	Helmut Hund, Wetzlar, Germany
XCell II™ Blot Module CE Mark	Invitrogen, Karlsruhe, Germany
XCell SureLock™ Mini-Cell	Invitrogen, Karlsruhe, Germany

5.1.9 Software

Analyst version 1.5	AB SCIEX Germany GmbH, Darmstadt, Germany
Analyst version 1.6TF	AB SCIEX Germany GmbH, Darmstadt, Germany
DatLab software version 4.3.4.70	OROBOROS Instruments, Innsbruck, Austria
MarkerView™ version 1.2.1	ABSciex, Darmstadt, Germany
Mascot 2.3 Search Algorithm	Matrix Science Inc, Boston, MA, USA
PeakView™ 2.1	ABSciex, Darmstadt, Germany
Progenesis SameSpots 4.1	Nonlinear Dynamics Limited, Newcastle upon Tyne, United Kingdom
Quantity One	Bio-Rad Laboratories GmbH, Munich, Germany
Protein Pilot 4.5	ABSciex, Darmstadt, Germany

5.2 Methods

5.2.1 Cell culture work

5.2.1.1 Cell culture conditions

The LLC-PK1 cell line was cultivated in the respective media at 37 °C, 5% CO2, in a saturated humid air incubator. All cell culture work was carried out under sterile conditions in a biological safety cabinet. The cell culture was tested regularly for mycoplasma infection using the PCR-based Myco Trace kit.

5.2.1.2 Thawing and cultivation of the cell line

The cell line was stored in liquid nitrogen in a mixture consisting of 90% heat-inactivated FCS and 10% DMSO. Following removal from liquid nitrogen, the cells were transported on ice. The cell line was rapidly thawed, transferred into a 75-cm^2 cell culture flask with prewarmed routine cell culture medium, and placed in the incubator. The next day, the medium was exchanged for fresh medium and the cells were incubated at 37 °C for another day.

Cell culture medium was exchanged every other day. At a confluence of 80 – 90%, cells were split for further subcultivation. For subcultivation, the confluent cells were washed twice with prewarmed PBS and trypsinized for 8 min at 37 °C by adding 3 mL Trypsin-EDTA. The reaction was stopped by the addition of 8 mL medium, before transfer of the cells into a sterile 15-mL Falcon tube. The tube was centrifuged at 125 x g, 5 min, 8 °C. The cells were resuspended in prewarmed fresh medium and

seeded in a 75-cm^2 flask at a subcultivation ratio of 1:3 to 1:8, as required for further stimulation or cultivation.

5.2.1.3 Cell count measurement

For cell counting, the CASY® cell counter + analyzer was used. The cells were passaged, resuspended in fresh medium, and diluted 1:200 in Casy®ton electrolyte. Care was taken to prevent the formation of cell aggregates, as cells have to pass individually through the capillary for accurate counting. The CASY® cell counter + analyzer makes use of the resistance measurement principle.

5.2.1.4 Stimulation of LLC-PK1 cells

The LLC-PK1 cell line had been stably transfected with either $EHHADH_{WT}$ or $EHHADH_{MUT}$ cDNA using the inducible Tet-on gene expression system. For stimulation, the cells were seeded in either stimulation medium 1 or 2 at a density of 0.25×10^6 cells / mL and grown for seven days. Tetracycline was added at a final concentration of 1 µg / mL with every changing of the medium. During the 7-day stimulation period, cells were allowed to grow to confluency.
Stimulation medium 1 was employed for Western blot analysis of EHHADH on a 2D-gel and co-immunoprecipitation experiments. For all other experiments, stimulation medium 2 was used.

5.2.1.5 Selection of transfected cell line

The cells were regularly controlled for mistargeting of $EHHADH_{MUT}$ into mitochondria and overexpression of both $EHHADH_{WT}$ and $EHHADH_{MUT}$ by means of immunofluorescence staining.
For selection, if necessary, cells were grown for 3-4 weeks in routine cell growth medium containing 200 µg / mL hygromycin B and checked for successful selection by means of immunofluorescence staining.

5.2.2 Immunofluorescence staining

For immunofluorescence staining, cells were stimulated for seven days on sterile cover glasses with a diameter of 24 mm. Cells were then incubated for 4 additional hours in stimulation medium supplemented with tetracycline and 1:50,000 diluted MitoTracker® Orange, which stains selectively mitochondria in living cells. Afterwards,

the cells were washed for 5 min with Ringer solution. For fixation of the cells, the cover glass with the adherent cells was incubated in 3 % PFA in PBS buffer for 30 min and then washed three times 5 min each with Ringer solution. For the subsequent antibody incubation, cells were permeabilized for 5 min in PBS/0.1 % SDS and washed three times, 5 min each, with PBS. For incubation with primary antibody, anti-EHHADH was used at a dilution of 1:1,000 in PBS/0.04 % Triton X-100 and incubated for 90 min at room temperature. The cells were washed between the primary and secondary antibody three times for 5 min each with PBS. The secondary antibody incubation (Alexa 488 goat anti-rabbit at a 1:400 dilution in PBS/0.04 % Trition X-100) was done for 1 hour at room temperature. Simultaneously, the cell-permeant nuclear counterstain Hoechst 33342 was added at a 1:400 dilution. Hoechst 33342 shows blue fluorescence when bound to double-strand DNA. Finally, cells were washed for 5 min with PBS, before the cover glasses were mounted with aqueous mounting medium and stored at 4 °C in the dark until inverse fluorescence microscopy.

While I carried out the immunfluorescence staining myself, the mounting of the cover glasses and the detection of the stain by microscopy were performed at the Institute of Medial Cell Biology by Carsten Broecker (PhD student).

The excitation and emission wavelengths used are shown in Table 3.

Table 3: Filter used for immunoflurescence staining.

	Excitation wavelength	**Emission wavelength**
MitoTracker® Orange	530 – 555 nm	575 – 630 nm
Hoe333422	365 nm	420 – 470 nm
Anti-EHHADH with secondary antibody Alexa Fluor® 488 goat anti-rabbit	465 – 495 nm	515 – 555 nm

5.2.3 Isolation of mitochondria

For isolation of mitochondria, a subcellular fractionation was performed. To that end, cells were washed three times with ice cold PBS and centrifuged at 500 x g and 4 °C for 5 min. The pellet was resuspended in 3 mL of mitochondria isolation buffer containing 1 % phosphatase and 0.1 % proteinase inhibitor cocktail, respectively.

Cells were disrupted by sonification (2x20 seconds / 20 % pulsation) and centrifuged at 1,500 x g and 4 °C for 5 min to pellet nuclei and intact cells. In the following, a centrifugation step with the supernatant at 12,000 x g, 15 min, 4 °C was conducted to obtain the cytoplasmic fraction in the supernatant and the mitochondria in the pellet. The mitochondria fraction was resuspended in 500 µL of isolation buffer and spun at 12,000 x g for 15 min. The resulting mitochondria containing pellet was resuspended in 300 µL of isolation buffer. Isolated mitochondria and an aliquot of whole-cell-lysate were stored at -80 °C until further analysis. A scheme of the differential centrifugation is shown in Figure 10. Protein amount was quantified using the FluoroProfile® kit according to the manufacturer´s protocol.

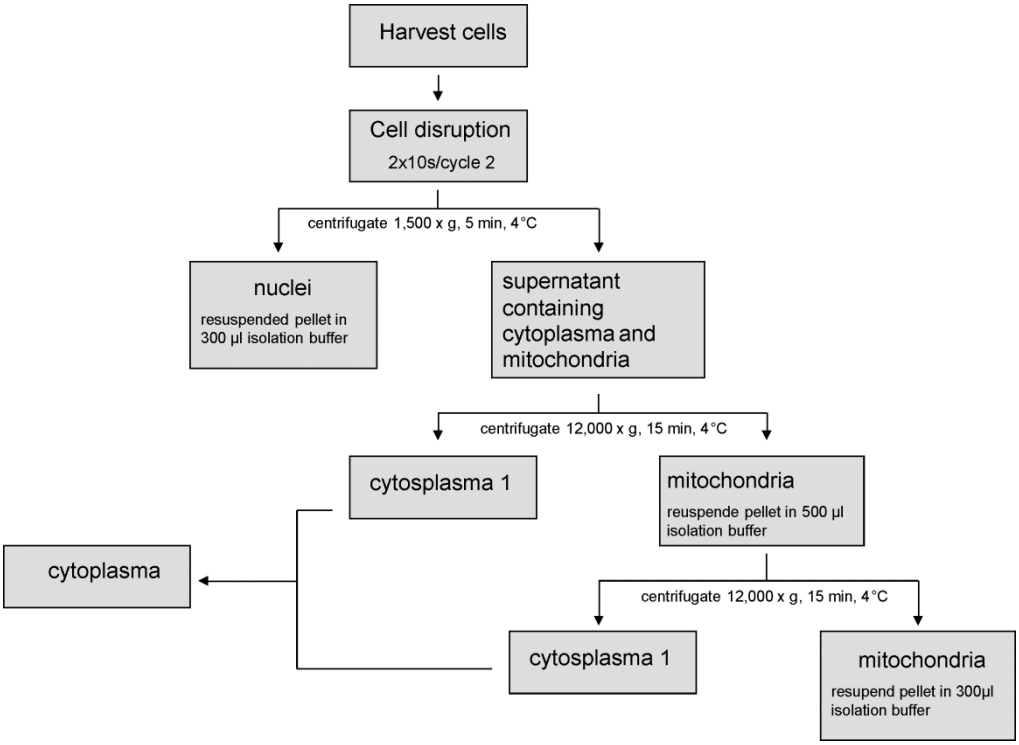

Figure 10: Scheme of the differential centrifugation procedure used.

5.2.4 BSA-fatty acid complex

Palmitic acid presents the bulk of the dietary fatty acids and is β-oxidized within the mitochondria. As palmitic acid is water insoluble, it is bound to bovine serum albumin as a carrier for cellular experiments. For the preparation of the BSA-fatty acid complex, 40 µL of 1 M NaOH were added to 2 mL stock solution of 0.125 M palmitic acid in 100% ethanol. The solution was dried for 30 min in a vacuum concentrator. The residuum was dissolved in 500 µL of hot (60 – 70 °C) water and slowly added to

glucose-free RPMI 1640 containing 0.2% fatty acid free BSA under continuous stirring at 37 °C. Thereafter, the medium was sterile filtered through a filter with a pore size of 0.2 µm, The absolute concentration of palmitic acid in the medium was determined by GC-MS and adjusted to 0.3 ± 0.02 mM.

5.2.5 SDS-PAGE with subsequent immunoblot analysis

5.2.5.1 Time series for EHHADH overexpression

A stimulation time series over six days was performed with the LLC-PK1 cell line to investigate the time-dependent expression of EHHADH within six days of stimulation. For immunoblot analysis, 20 µg of total protein were separated on a 4-12% Bis-Tris gel run for 20 min and 60 min each at 50 V and 200 V, respectively. Afterwards, the gel was blotted for one hour at 25 V on a PVDF membrane (0.45 µm). Transfer efficiency was monitored by Ponceau staining. The blot was blocked first overnight at 4 °C in TBS-T + 5% milk powder, and then incubated for an additional hour at room temperature, before it was washed in TBS-T once for 15 min and then two times for 5 min. Subsequently, the blot was incubated with a 1:1,250 dilution of anti-EHHADH-antibody for 90 min at room temperature followed by three washing steps with TBS-T (once 15 min and twice 5 min). For binding of the secondary antibody (ECL Rabbit IgG, HRP-linked whole antibody from donkey) a 1:4,500 dilution and an incubation period of one hour at room temperature were used. After further washing steps, the blot was developed using Amersham ECL Plus™ Western Blotting Detection Reagents, and after 5 min the chemiluminescence signal was detected by means of a Bio-Rad VersaDoc 4000 MP imaging system.

5.2.5.2 Analysis of mistargeting of EHHADH by immunoblotting

Immunoblot analyses of whole cell lysate and purified mitochondria of $EHHADH_{WT}$ and $EHHADH_{MUT}$ were performed. On a NuPAGE® Novex 4-12% Bis Tris gel, 3 µg of whole cell lysate and 3 µg of purified mitochondria were loaded and run at 50 V for 20 min and at 200 V for 60 min. After the run, proteins were blotted from the gel with the XCell II™ Blot Module CE Mark onto a 0.45 µm PVDF membrane for 1 hour at 25 V. Further analysis was carried out as described above.

5.2.6 Two-dimensional differential in-gel electrophoresis

A 2D-DIGE approach was used to determine EHHADH on a 2D gel. To that end, 25 µg of whole cell lysate in labelling buffer from either *EHHADH$_{WT}$* or *EHHADH$_{MUT}$* cells were labeled with cyanine dyes (Cy3 and Cy5) before the analysis, according to manufacturer´s protocol. In this analysis, EHHADH$_{WT}$ and EHHADH$_{MUT}$ were labeled with Cy3 and Cy5, respectively. The IPG strip was rehydrated in rehydration solution overnight. For the first dimension, a 7-cm IPG-strip with a pH range from pH 8 to 11 was used. Isoelectric focussing was performed using the Ettan IPGphor 3 for a total of 28.5 kVhrs, with cup loading on the acidic end of the IPG strip, using the gradient shown in Table 4. After isoelectric focusing, the IPG strips were equilibrated first in SDS equilibration buffer containing 130 mM DTT for 20 min to reduce disulfide bonds followed by incubation in SDS equilibration buffer containing 280 mM iodoacetamide for 20 min to alkylate the thiol groups. The equilibrated IPG strips were laid on a 10% acrylamide gel and the second dimension was run for 20 min at 50 V and then for 100 min at 120 V in a XCell SureLock® Mini-Cell Electrophoresis System. After the run, images were taken by the Bio-Rad VersaDoc 4000 MP imaging system.

Table 4: Program for isoelectric focussing on the Ettan IPGphor 3.

Voltage (V)	time (h)	Step and voltage methode
40	2	Step´n´Hold
100	1	Step´n´Hold
500	4	Gradient
1000	3	Gradient
1000	2	Step´n´Hold
4000	12	Step´n´Hold

In addition, an immunoblot analysis of the same gel was performed to localize EHHADH on the 2D-gel. To that end, proteins were blotted after imaging from the gel for one hour at 25 V onto a PVDF membrane (0.45 µm) by means of the XCell II™ Blot Module CE Mark. Protein transfer was monitored by Ponceau staining and the blot was blocked overnight at 4 °C using Rotiblock®. The blot was incubated for an additional hour at room temperature in TBS-T + 5% milk powder and washed in TBS-T for 15 min and two times for 5 min. For the anti-EHHADH-antibody, a dilution of 1:1,250 and an incubation time of 90 min at room temperature were used, followed

by three washing steps with TBS-T (once for 15 min and twice for 5 min each). For binding of the secondary antibody (ECL Rabbit IgG, HRP-linked whole antibody from donkey), a dilution of 1:4,500 and an incubation time of one hour at room temperature were used. After further washing steps, the blot was developed using Amersham ECL Plus™ Western Blotting Detection Reagents, and after 5 min the chemiluminescence signal was detected using a Bio-Rad VersaDoc 4000 MP imaging system. Using the Quantity One software an overlay picture was generated (Figure 2B).

5.2.7 Co-Immunoprecipitation

5.2.7.1 Co-immunoprecipitaton of EHHADH

To find possible mitochondrial interaction partners of $EHHADH_{MUT}$, a co-immunoprecipitation with a commercial EHHADH antibody and the Pierce® Protein A/G Magnetic IP/Co-IP Kit was performed. First, an immune complex was formed by adding 10 µg of EHHADH antibody to 360 µg of isolated mitochondria from either *EHHADH*$_{WT}$ or *EHHADH*$_{MUT}$ cells and overnight incubation at 4 °C. Next, 25 µg of Pierce Protein A/G Magnetic beads were transferred to a 1.5-mL microcentrifuge tube and washed by adding 175 µL of IP Lysis/Wash Buffer and gentle mixing. The tube was placed in a magnetic stand to collect the magnetic beads against one side of the tube and the supernatant was discarded. Two further washing steps were performed by adding each time 1 mL of IP Lysis/Wash Buffer and repeated inversion of the tube for 1 min, before the magnetic beads were collected and the supernatant was discarded. Subsequently, the antigen sample/antibody mixture was added to the prewashed magnetic beads and incubated at room temperature for 3 h under continuous mixing. After the incubation, the beads were collected with a magnetic stand. The unbound proteins were removed and the magnetic beads were washed three times. In the last washing step, 500 µL of ultrapure water was added to the magnetic beads, which were then collected by a magnetic stand. For the elution step, 100 µL of 2x LDS sample buffer was added to the magnetic beads and incubated for 10 min under continuous mixing. The resulting supernatant, including the protein-protein complex of interest, was saved for further analysis. A scheme of the working procedure is shown in Figure 11.

Afterwards, a diagonal two-dimensional SDS-PAGE was performed with the co-immunoprecipitated samples. Briefly, 20 µL of sample was loaded on a NuPAGE® Novex 4-12% Bis Tris gel and run under non-reducing conditions at 50 V for 20 min and at 200 V for 60 min. After the first gel run, the lanes for $EHHADH_{WT}$ and $EHHADH_{MUT}$ were cut out, equilibrated for 15 min in NuPAGE® LDS sample buffer with 0.05 M DTT, and placed on top of a NuPAGE® Novex 12% Bis Tris gel. The second gel runs were performed under reducing conditions with the addition of NuPAGE® Antioxidant to the cathode buffer chamber. The gels were run as described above and stained with Coomassie Brilliant Blue over night before they were placed in deionized water for destaining. Images of the gels were acquired using the Bio-Rad VersaDoc 4000 MP imaging system. Every visible spot was excised, washed, digested with trypsin and extracted with 5% formic acid before analysis by nano-HPLC-QTOF-MS/MS. Proteins were identified using the Mascot Distiller software.

Analyses were accomplished by means of a QStar XL MS/MS system (AB Sciex, Darmstadt, Germany) coupled to an Ultimate 3000 nano-HPLC-system with precolumn concentration (100 µm I.D., 2 cm length, 5 µm Acclaim PepMap, flow-rate 5 µL/min). The samples were separated on a 25 cm-column (75 µm I.D., 3 µm Acclaim PepMap) at a flow-rate of 300 µL/min using a 212-min gradient from 4-40% B. The QStar XL mass spectrometer was operated in IDA-mode acquiring first a TOF-scan from 350-1250 Da for 1 s, followed by product ion scans for 2.5 s for the two most intense ions. MS/MS spectra were searched against the NCBInr database (August 2013) using the ProteinPilot software (version 4.5) applying a 1% FDR.

5.2.7.2 Co-immunoprecipitation of HADHB

Co-immunoprecipitation against HADHB was performed, as both subunits, HADHA and HADHB, are possible interaction partners of mislocalized EHHADH. The Pierce® Protein A/G Magnetic IP/Co-IP Kit was used in this experiment. For the formation of the immune complex 500 µg of isolated mitochondria from either $EHHADH_{WT}$ or $EHHADH_{MUT}$ cells were incubated with 10 µg HADHB antibody over night at 4 °C. Further steps of co-immunoprecipitation were performed as described above. Afterwards, immunoblot analyses against HADHA, HADHB and EHHADH were performed. Briefly, 15 µL of co-immunoprecipitation sample of either $EHHADH_{WT}$ or

EHHADH$_{MUT}$ was separated on a 4-12% Bis-Tris gel for every antibody used for the immunoblot analysis. Afterwards, the gel was blotted for one hour at 25 V on a PVDF membrane (0.45 µm Immobilon P). Transfer efficiency was monitored by Ponceau staining, and the blot was blocked over night at 4 °C in TBS-T + 5% skimmed milk powder. After incubation for an additional hour at room temperature, the membrane was washed three times in TBS-T, once for 15 min and twice for 5 min each, and incubated with anti-EHHADH antibody (1:1,250), anti-HADHB antibody (1:200), and for the anti-HADHA antibody (1:1,000), respectively, for 90 min at room temperature. The membrane was washed again trice with TBS-T and incubated with an appropriate HRP-linked secondary antibody to anti-EHHADH and anti-HADHA (ECL Rabbit IgG, whole antibody from donkey, 1:4,500 dilution) and anti-HADHB (Bovine anti-goat IgG-HRP, 1:2,500 dilution) for one hour at room temperature. After further washing steps, the blot was developed using Amersham ECL Plus™ Western Blotting Detection Reagents, and after a 5-min incubation the chemiluminescence signal was detected using the Bio-Rad VersaDoc 4000 MP imaging system.

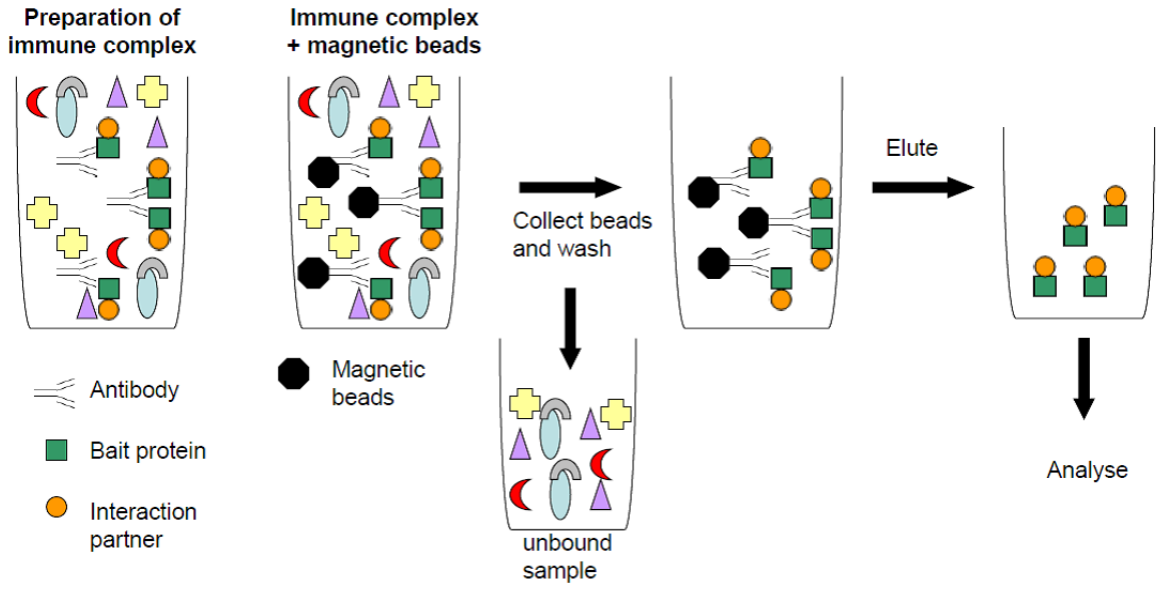

Figure 11: Working procedure for co-immunoprecipitation with the Pierce® Protein A/G Magnetic IP/Co-IP Kit

5.2.8 Blue native PAGE analysis

5.2.8.1 Incorporation of $EHHADH_{MUT}$ into MTP

For blue native PAGE, 125 µg of isolated mitochondria from either mutated or wild-type transfected LLC-PK1 were centrifuged at 12,000 x g and 4 °C for 15 min to pelletize intact mitochondria. The organelle proteins were solubilized in cold NativePAGE™ sample buffer containing 0.5% DDM by pipetting up and down and repeated inversion. After incubation on ice for 15 min, samples were centrifuged at 20,000 x g and 4 °C for 30 min to pelletize the non-solubilised organelle proteins. The supernatant was transferred to an Eppendorf tube and stored at -80 °C until further use. Before loading of the samples, the wells of the NativePAGE™ 4-16% Bis-Tris gels were filled with dark blue native cathode buffer for better visualization of sample wells. Samples were first run at 150 V for 20 min, then the dark blue cathode buffer was replaced with light blue cathode buffer, before the gel was run at 50 V and 250 V, respectively, for 1 hr each. The gel was then electroblotted to a PVDF membrane (0.45 µm) at 25 V for one hour using the XCell II™ Blot Module CE. Subsequently, the membrane was incubated in 20 mL of 8% acetic acid for 15 min rinsed with deionized water and, finally, air-dried. Prior to immunoblot analysis, the membrane was rewetted in 100% methanol, rinsed with deionized water, and incubated overnight in TBS-T + 5% skimmed milk powder. After incubation for an additional one hour at room temperature, the membrane was washed in TBS-T once for 15 min and two times for 5 min each, and then incubated with anti-EHHADH-antibody (1:1,250) and anti-HADHB-antibody (1:200), respectively, for 90 min at room temperature, followed by repeated washing with TBS-T (once for 15 min and twice 5 min each). The membrane was then incubated with the appropriate secondary antibody to anti-EHHADH (ECL Rabbit IgG, HRP-linked whole antibody from donkey) and anti-HADHB (bovine anti-goat IgG-HRP conjugated) at dilutions of 1:4,500 and 1:2,500, respectively, for one hour at room temperature. After further washing steps the blot was developed using Amersham ECL Plus™ Western Blotting Detection Reagents. After 5 min of incubation the chemiluminescence signal was detected using a Bio-Rad VersaDoc 4000 MP imaging system.

5.2.8.2 2D blue native / SDS-PAGE analysis

For 2D blue native / SDS-PAGE with subsequent immunoblot analysis, 75 µg of isolated mitochondria form either *EHHADH$_{WT}$* or *EHHADH$_{MUT}$* LLC-PK1 cells were prepared as outlined above using a digitonin concentration of 4 g / g protein. Mitochondrial proteins were separated on a NativePAGE™ 3-12% Bis-Tris gel for 30 min at 150 V with dark blue cathode buffer and, subsequently, 2 h 50 min, at 250 V, with light blue cathode buffer. Lanes were cut out of the blue native gel, equilibrated first for 15 min in SDS equilibration buffer with 54 mM DTT, followed by 15-min equilibration in SDS equilibration buffer supplemented with 0.1 M IAA. Lanes were then rotated by 90° and laid onto a 12% Bis Tris 2D well gel. The gels were run in the second dimension for 40 min at 50 V and for 2 hours at 200 V. Subsequently, the separated proteins were transferred by semi-dry electroblotting to a PVDF membrane (0.45 µm) for two hours at 45 mA and blocked overnight with RotiBlock®. For subsequent immunoblot analysis, blots were washed once in TBS-T for 15 min and two times for 5 min each. Blots were then incubated with anti-EHHADH-antibody (1:1,250) for 90 min at room temperature followed by washing with TBS-T (once for 15 min and twice for 5 min each). For binding of the secondary antibody to anti-EHHADH a dilution of 1:4,500 was used (ECL Rabbit IgG, HRP-linked whole antibody from donkey) and incubated for one hour at room temperature. After further washing steps, the blot was developed using Amersham ECL Plus™ Western Blotting Detection Reagents, and after 5 minutes incubation the chemiluminescence signal was detected using a Bio-Rad VersaDoc 4000 MP imaging system.

5.2.9 Metabolic analysis

5.2.9.1 ATP measurement

Measurement of ATP content was achieved using the ATP Colorimetric/Fluorometric Assay Kit from BioVision Inc. according to the manufacturer's instructions. Briefly, stimulated cells were lysed with ATP Assay Buffer and deproteinized using a 10-kDa spin column. Fifthy µL of either EHHADH$_{WT}$ or EHHADH$_{MUT}$ cell lysate were added to a 96-well plate. For every sample of EHHADH$_{WT}$ or EHHADH$_{MUT}$ an ATP measurement and a background measurement were carried out. A standard curve was prepared ranging from 0.025 to 1.0 nmol ATP / well, with six calibrations points,

and water as control. To each sample and standard, 50 µL of reaction mixture were added, containing 45.8 µL ATP Assay Buffer, 0.2 µL ATP Probe, 2.0 µL ATP Converter and 2.0 µL Developer. For the background, 50 µL of reaction mixture was added, containing 47.8 µL ATP Assay Buffer, 0.2 µL ATP Probe and 2.0 µL Developer.

Protected from light, the reactions were incubated for 30 min at room temperature. Fluorescence was measured using the Fluorostar Optima plate reader, with an excitation wavelength of 535 nm and an emission wavelength of 587 nm. The measurements were replicated four times each for the *EHHADH*$_{WT}$ or *EHHADH*$_{MUT}$ LLC-PK1 cells.

5.2.9.2 Acylcarnitine measurement

For acylcarnitine analysis, an aliquot of 1 mL of cell culture stimulation medium with palmitic acid was centrifuged at 1,500 x g, 4 °C for 5 min to pelletize the cells. The supernatant was then transferred to a new Eppendorf tube. Acylcarnitines were extracted by adding 300 µL of 80% aqueous methanol and 100 µL of MassChrom® internal standard labeled amino acids and acylcarnitines to 100 µL of cell culture supernatant, followed by centrifugation at 10,000 x g, 8 °C, for 5 min. The supernatant was dried for 75 min in a vacuum evaporator, reconstituted in 100 µL of 50 % aqueous methanol, and analyzed by LC-ESI-MS/MS. The experiment was replicated four times.

5.2.9.3 Acetyl-CoA measurement

For acetyl-CoA analysis, the cell culture medium was replaced by ice cold PBS and washed three times, before 2 mL cold 80% aqueous methanol was added and the cells were detached using a cell scraper as described previously [68]. For experiments with unlabeled palmitic acid, a 5 µM internal standard of acetyl-1,2-$^{13}C_2$-CoA was added, for experiments with ^{13}C-labeled palmitic acid no internal standard was added. Extracts were evaporated and reconstituted in 70 µL of ultrapure water immediately prior to LC-ESI-MS/MS analysis.

5.2.9.4 Palmitic acid uptake

For determination of the fatty acid uptake rates of EHHADH$_{MUT}$ and EHHADH$_{WT}$, the uptake of palmitic acid from cell culture medium was measured. The cells were

incubated with stimulation medium 2 for 48 hrs. Subsequently, culture supernatants obtained from *EHHADH*$_{MUT}$ and *EHHADH*$_{WT}$ cells, respectively, were centrifuged at 1,500 x g, 4 °C, for 5 min to pelletize the cells and the supernatants were transferred to new tubes. The palmitic acid content of the supernatants and a medium control incubated for 48 hrs was measured by GC-MS after transesterification of palmitic acid with methanol to its corresponding methyl ester according to Masood et al. [69]. The working group of Katja Dettmer-Wilde at the Institute of Functional Genomics performed the GC-MS analysis on an Agilent model 6890 GC that was equipped with a Mass Selective Detector (MSD) model 5975 Inert XL. GC was performed using an SLB-IL59 column (30 m x 0.25 mm inner diameter, 0.2 µm film thickness). Samples were injected in splittless modet at 280 °C, with an injection volume of 1 µL. The gradient for the GC separation was ramped at 5 °C/min from an initial oven temperature of 50 °C to 290 °C and held for 5 min. As carrier gas, helium was used at a constant flow rate of 0.7 mL/min. The mass spectrometer was operated in full scan mode from 50-550 m/z. Quantification was performed using a calibration curve for palmitic acid methyl ester with [U-^{13}C]palmitic acid methyl ester serving as an internal standard.

5.2.9.5 LC-ESI MS/MS analysis

LC-ESI-MS/MS was carried out on an Agilent 1200 SL HPLC system using an Atlantis T3 (3 µm, 2.1 mm i.d. x 150 mm) reversed phase column (Waters, Eschborn, Germany). The flow-rate was 350 and 400 µL*min^{-1} for the acylcarnitine and acetyl-CoA analysis, respectively. The gradient for the former was 0-8 min 0% B, 8-11 min 100% B, 11-11.1 min from 100% to 0% B, and 0% B for 8.9 min. The gradient for the acetyl-CoA measurement was as follows: 0-5 min 5 % B, 5-17 min linear increase from 5 to 30% B, 17-19 min hold 30% B, 19-20 min linear increase from 30 to 90% B, 20-21 min increase from 90 to 95% B, 21-24 min hold 95 % B, 24-25 min decrease from 95 to 5% B, 25-30 min hold 5% B. The injection volume was 10 µL for both methods. The HPLC system was directly coupled to an AB-Sciex 4000 QTrap® mass spectrometer. Acylcarnitines and acetyl-CoA were quantified by multiple reaction monitoring (MRM) in positive ionization mode with a dwell time of 300 ms, using the parameters listed in Supplemental Table 1. Data analysis was performed by Analyst version 1.5 (AB-Sciex).

5.2.10 High resolution respirometry

5.2.10.1 Substrate-uncoupler-inhibitor titration protocol

High-resolution respirometry was performed at the Chair of Medical Cell Biology to check whether the transfected *EHHADH*$_{MUT}$ cell line showed a phenotype in respiration comparable to that of the wild-type transfected cell line. For high-resolution respirometry, cells were harvested as described under the cell culture work section and resuspended in MiR05. Cell density was measured by means of a Casy® Cell Counter + Analyser System. Respiration per cell was measured with an Oroboros-2k oxygraph, which features two chambers, for the parallel measuring of two samples. Prior to use, both chambers of the oxygraph were filled with 2.1 mL of MiR05 medium each, equilibrated with oxygen at 37 °C, and calibrated for oxygen saturation. Next, the media were replaced with 2.8 mL cell suspension in MiR05 at 37 °C, of which 700 µL were removed and directly frozen in liquid nitrogen for citrate synthase activity measurements. The chambers were closed with stoppers and the respiration rates were measured. The cell suspensions were continuously stirred at 750 rpm. The measurements were corrected for instrumental background, which had been determined in a separate experiment, and the data were recorded and analyzed using the DatLab software (version 4.3.4.70). For high-resolution respirometry, the substrate-uncoupler-inhibitor titration protocol shown in Table 5 was used. The experiments with the *EHHADH*$_{WT}$ and *EHHADH*$_{MUT}$ cell lines were repeated a minimum of n = 10. Oxygen flux was normalized to citrate synthase activity.

Table 5: Substrate-uncoupler-inhibitor titration protocol for high-resolution respirometry measurements.

Substrate/Uncoupler/Inhibitor	Volume (µL)	Final concentration
Malate	5	2 mM
Digitonin	3	12.2 µM
Palmitoylcarnitine	2	1 µM
Adenosine diphosphate (ADP)	20	5 mM
Glutamate / Pyruvate	10 / 5	10 mM / 5 mM

Table 5 (continued)

Substrate/Uncoupler/Inhibitor	Volume (µL)	Final concentration
Cytochrome C	5	10 µM
Succinate	20	10 mM
Oligomycin	2	4 µg/ml
FCCP	1 / 1 / 1	0.5 µM / 1 µM / 1.5 µM
Rotenone	2	0.1 µM
Antimycin A	1	2.5 µM
Ascorbate / Tetramethyl-*p*-phenylenediamine (TMPD)	20 / 5	8 mM / 0.5 mM

5.2.10.2 Inhibition of palmitoyl-CoA on respiration

In a second experiment, high-resolution respirometry was employed to measure the inhibition of respiration by long-chain acyl-CoAs. The cells were stimulated by the substrate-uncoupler-inhibition titration protocol shown in Table 5, except for the addition of palmitoylcarnitine. After the induction of maximal phosphorylation capacity by the addition of succinate, palmitoyl-CoA was added at a final concentration range of 10 – 60 µM to the oxygraph chamber, and the decrease in respiration was measured. In addition, controls were included, but measured in the absence of palmitoyl-CoA. The inhibition experiments with the $EHHADH_{WT}$ and $EHHADH_{MUT}$ cell lines were repeated a minimum of n = 4.

5.2.11 Citrate synthase activity measurement

The activity of citrate synthase was measured spectrophotometrically by means of an Amersham Biosciences Ultrospec 3100 pro. Seven hundred µL of cell suspension were prewarmed for 10 min at 37 °C. One hundred µL of cell suspension were added to 900 µL of prewarmed (37 °C) incubation medium containing 700 µL ultrapure water, 100 µL 0.1 mM DTNB in 1 M Tris-HCl buffer, pH 8.1, 25 µL 10 % Trition X-100, 50 µL 10 mM oxaloacetate in 0.1 mM triethanolamine-HCl-buffer, pH 8.0, 25 µL acetyl-CoA, mixed carefully and the linear increase in absorbance was measured every 20 s at 412 nm over 200 s [70]. The device automatically calculated the slope of the enzyme kinetics. Citrate synthase activity was then used for normalization of oxygen flux.

5.2.12 Respiratory chain supercomplex assembly

For the quantification of supercomplex formation, a blue native PAGE of isolated *EHHADH$_{WT}$* or *EHHADH$_{MUT}$* mitochondria was performed. For blue native PAGE, 200 µg of sample were prepared as stated above, with a digitionin concentration of 4 g / g protein. The samples were separated on a NativePAGE™ 3-12% Bis-Tris gel according to the manufacturer´s protocol and, subsequently, stained with the SERVA Purple protein stain. For staining of the 1D gel, the gels were fixed for 1 h at room temperature in Solution 1. The gels were then stained for 1.5 h in Solution 2, to which the SERVA Purple concentrate had been added at a 1:250 dilution immediatedly prior to staining. The gels were washed by gentle rocking in Solution 3 for 30 min prior to acidification of the gels in Solution 1 for 30 min. The stain was visualized using the VersaDoc 4000 MP imaging system and quantified by the Bio-Rad software Image Lab. The analysis was repeated seven times and values normalized to complex V.

5.2.13 SWATH™ analysis

One hundred µg of total cell lysate were used for filter-aided sample preparation using 30 kDa centrifugal filter units as described by Wisniewski et al. [71]. Ten µL of total cell lysate of either *EHHADH$_{WT}$* or *EHHADH$_{MUT}$* cells were used for nano-LC-MS/MS-analysis. Analyses were accomplished by means of a TripleTOF 5600+ QTOF mass spectrometer (AB Sciex, Darmstadt, Germany) coupled to an Ultimate 3000 nano-HPLC-system with precolumn concentration (100 µm I.D., 2 cm length, 5 µm Acclaim PepMap, flow rate 5 µL/min). The samples were separated on a 25 cm-column (75 µm I.D., 3 µm Acclaim PepMap) at a flow rate of 300 µL/min using a 212-min gradient from 4-40% B. For generation of the peptide library, the mass spectrometer was operated in independent data acquisition (IDA) mode, acquiring first a TOF-scan from 350-1250 Da for 250 ms, followed by product ion scans of the 25 most intensive signals for 100 ms each (m/z-range 230-1500 Da). MS/MS spectra were searched against the NCBInr database (August 2013) using the ProteinPilot software (version 4.5) applying a 1% FDR. For SWATH™-analyses the same HPLC-conditions were applied, but the mass spectrometer conducted a 50 ms TOF-scan

followed by 37 SWATH-windows (100 ms each; m/z-range 230-1500 Da) spanning a precursor-m/z-range of 350-1250 Da. SWATH™-data was processed using the PeakView™- and MarkerView™-software. Up to six unique, unmodified peptides per protein with six transitions per peptide were used for quantification, data was normalized to total intensity, and pairwise t-tests were conducted. Analyses were carried out in triplicate.

5.2.14 Statistical analysis

A one-way ANOVA test was used for comparison between more than two groups. Statistical analysis between two groups were made using the paired Student´s t-test. A p-value ≤ 0.05 was considered to be statistically significant. For multiple testing, the method of Benjamin and Hochberg [72] was used to adjust the p-value by controlling the false discovery rate (FDR).

6 Results

6.1 Stable overexpression and localization of EHHADH

6.1.1 Time series for EHHADH overexpression

A stable overexpression of $EHHADH_{WT}$ and $EHHADH_{MUT}$ is a requirement for all following analyses. Therefore, over the first six days of stimulation, every day whole cell lysate was taken and separated on a 4-12% Bis Tris gel, followed by immunoblot analysis using a custom-made anti-EHHADH. As shown in Figure 12, after 48 hours of stimulation, EHHADH was detected by immunoblot analysis. At day 4, EHHADH overexpression reached a plateau-phase that persisted thru day 6.

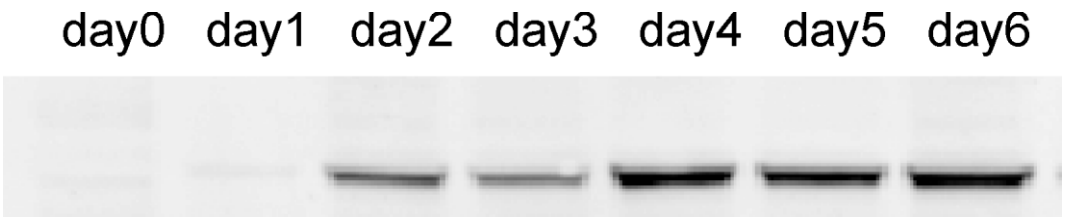

Figure 12: Immunoblot analysis of stable overexpression of EHHADH during the first six days of stimulation.

6.1.2 Analysis of mistargeting of EHHADH by immunoblotting

The mistargeting of $EHHADH_{MUT}$ into mitochondria was confirmed by immunoblot analysis. The whole cell lysate of *$EHHADH_{MUT}$* cells yielded a well resolved double band (Figure 13A), while the mitochondrial fraction of *EHHADHwt* cells did not yield any band. Only the lower band is obtained in isolated mitochondria of the *$EHHADH_{MUT}$* cell line (Figure 13B).

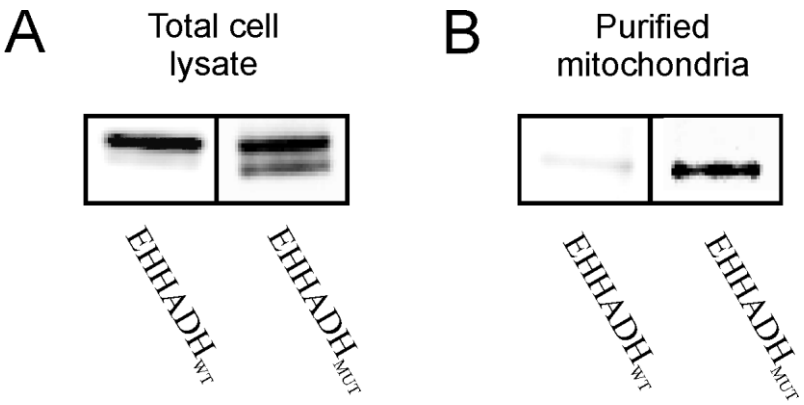

Figure 13: Immunoblot analysis of total cell lysate and purified mitochondria of EHHADH$_{WT}$ and *EHHADH$_{MUT}$* cells. Analyses of total cell lysates by immunoblotting showed a single band for *EHHADH$_{WT}$* cells and a well-resolved double band for *EHHADH$_{MUT}$* cells. In a purified mitochondrial protein extract of *EHHADH$_{WT}$* cells, no EHHADH could be detected, whereas the extract of EHHADH$_{MUT}$ cells showed the lower molecular weight band of EHHADH.

(Source: Assmann et al., Unravelling the pathomechanism of an autosomal dominant Fanconi´s Syndrome: a mitochondriopathy caused by mistargeting of a peroxisomal protein, Cell Rep., in revision)

6.1.3 Control of mistargeting of EHHADH$_{MUT}$ by immunofluorescence staining

The mistargeting of EHHADH$_{MUT}$ was verified regularly by immunofluorescence staining. An exemplary immunofluroescence staining is shown in Figure 14. For the *EHHADH$_{WT}$* cell line, immunohistochemical staining against EHHADH showed a clear peroxisomal localization, as seen by the dotted pattern in green (Figure 14A). In Figure 14B the mitochondrial staining with MitoTracker® Orange of *EHHADH$_{WT}$* cell line is shown. In the respective overlay of the peroxisomal protein EHHADH and MitoTracker® Orange (Figure 14C) it is obvious that no localization of EHHADH$_{WT}$ into mitochondria has occurred. In the *EHHADH$_{MUT}$* cell line, the staining against EHHADH showed a more widespread localization (Figure 14D) compared to the *EHHADH$_{WT}$* cell line. Figure 14E showed the mitochondrial staining of *EHHADH$_{MUT}$* cell line. The overlay (Figure 14F) of *EHHADH$_{MUT}$* cells showed, that EHHADH$_{MUT}$ was mistargeted to the mitochondria in addition to the expected peroxisomal localization, as shown by the yellow areas in the overlay.

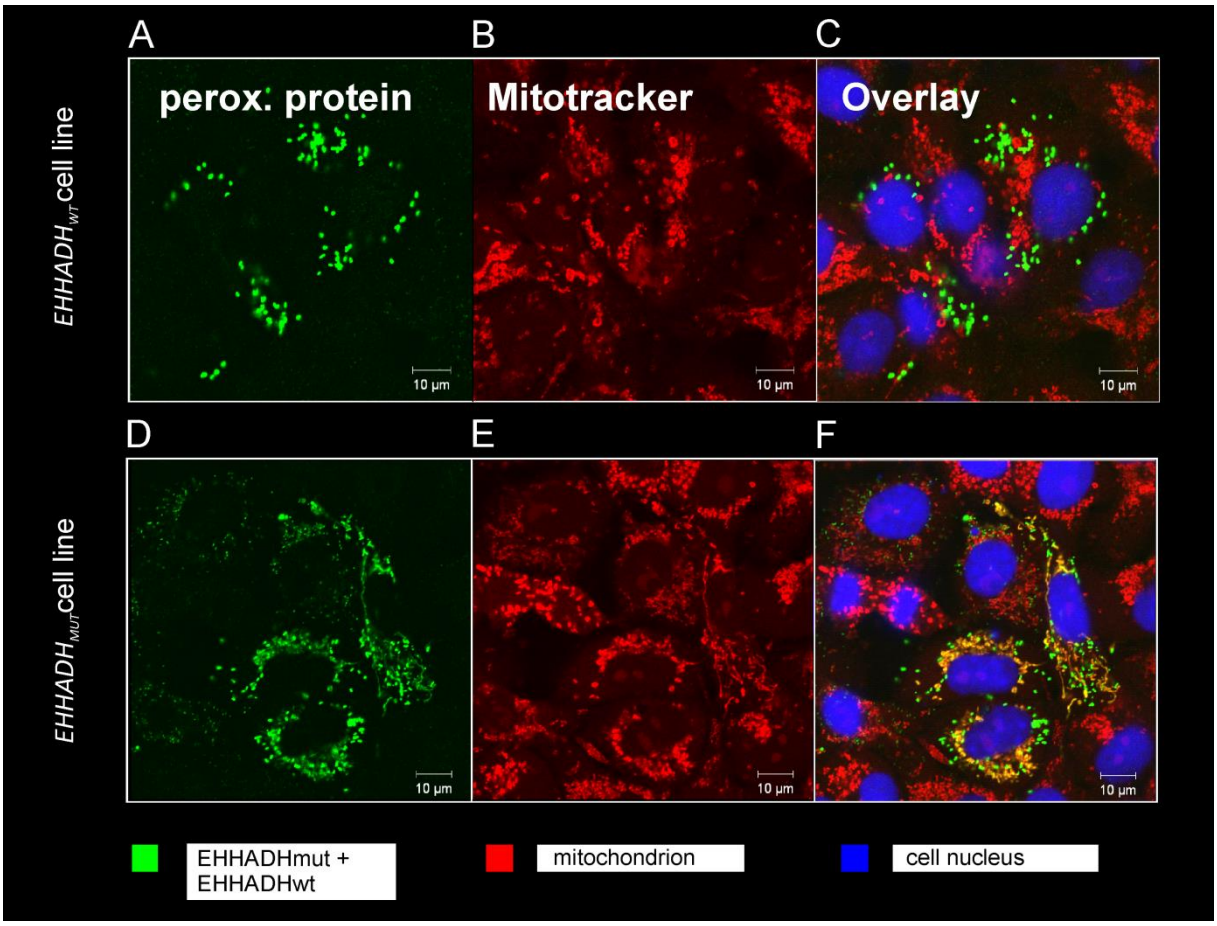

Figure 14: Immunfluorescence staining of *EHHADH$_{WT}$* cells shown in A-C *and EHHADH$_{MUT}$* cells in D-F. A and D: Staining of EHHADH with a custom-made anti-EHHADH antibody; B and E: Staining of mitochondria with MitoTracker® Orange; C and F: Staining of nuclei with DAPI and overlay of staining for EHHADH and MitoTracker® Orange for the respective cell line; Scale bars are 10 µm.

6.1.4 Two-dimensional differential in-gel electrophoresis

In two-dimensional differential in-gel electrophoresis (2D-DIGE), up to three samples are labeled with fluorescence dyes (Cy2, Cy3 and Cy5). The labeled samples are mixed prior to classical 2D gel electrophoresis. 2D-DIGE overcomes some limitations of traditional 2D gel electrophoresis, like gel-to-gel variation, which facilitates the direct comparison of different specimens. In addition, small differences between wild type and mutated proteins, like a shift in pI between EHHADH$_{WT}$ and EHHADH$_{MUT}$, can be distinguished.

Therefore, 2D DIGE analysis of whole cell lysate of *EHHADH$_{WT}$* cell line and *EHHADH$_{MUT}$* cell line was performed. Figure 15A shows an overlay of the Cy3 and Cy5 images of the 2D DIGE gel, revealing a shift in pI between EHHADH$_{WT}$ and EHHADH$_{MUT}$, with the latter being more basic. For the determination of the

localization of EHHADH in the 2D gel, an immunoblot analysis was carried out. Figure 15B shows the position of EHHADH on the 2D gel, which tallies with the protein spots for $EHHADH_{WT}$ and $EHHADH_{MUT}$ in Figures 15A.

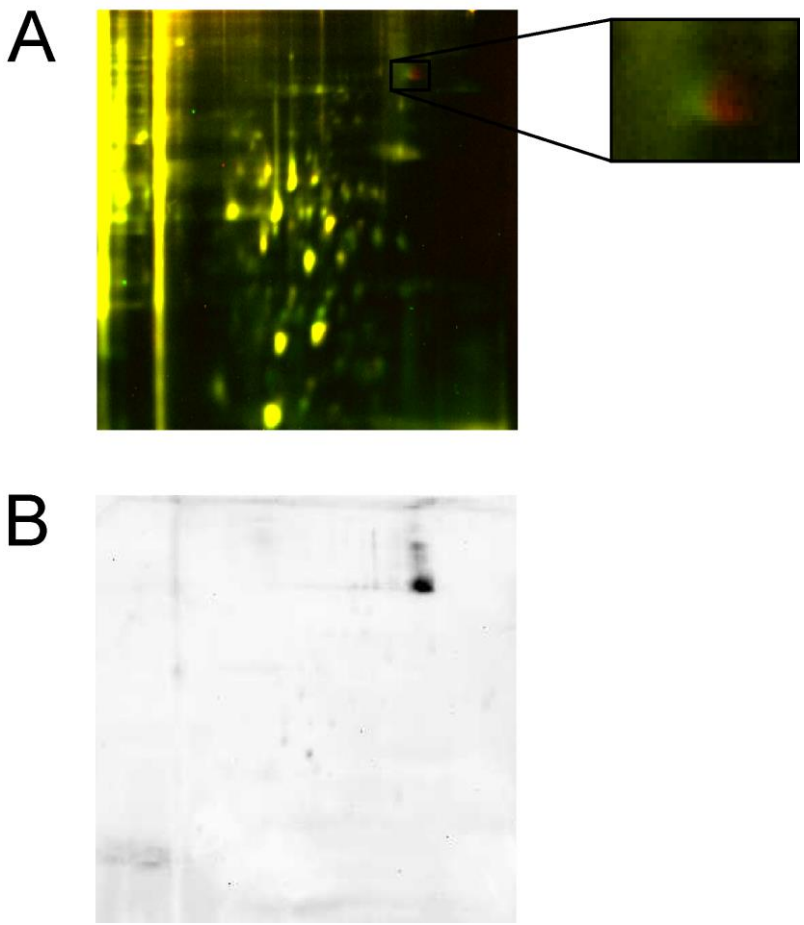

Figure 15: Two-dimensional differential in-gel electrophoresis of whole cell lysates of *$EHHADH_{WT}$ and $EHHADH_{MUT}$* cell lines, respectively. A: Overlay image of 2D-DIGE gel of Cy3-labeled *$EHHADH_{WT}$* cell line (green) and Cy5-labled *$EHHADH_{MUT}$* cell line (red). The overlay reveals a shift in pI between *$EHHADH_{WT}$* cell line and *$EHHADH_{MUT}$* cell line, where the latter shifts slightly to a basic pI. B: Immunoblot with custom-made anti-EHHADH antidody for detection of EHHADH in the 2D-gel.

6.2 Incorporation of mutated EHHADH into the mitochondrial trifunctional protein

6.2.1 Co-immunoprecipitation of EHHADH and HADHB

To find possible mitochondrial interaction partners of $EHHADH_{MUT}$, co-immunoprecipitation experiments with a commercial EHHADH-antibody were performed on mitochondrial protein extracts of *$EHHADH_{WT}$* and *$EHHADH_{MUT}$* cells,

respectively. The co-immunoprecipitates were subsequently used for diagonal two-dimensional SDS-PAGE (non-reducing / reducing). The gel was stained with coomassie dye and every visible spot was cut out and prepared for nano-HPLC-QTOF-MS/MS analysis.

The subunits of the heterooctameric mitochondrial trifuctional protein (MTP), HADHA and HADHB, were identified as potential mitochondrial interaction partners of $EHHADH_{MUT}$. Next, a co-immunoprecipitation of HADHB was conducted, followed by immunoblot analysis with anti-EHHADH, anti-HADHA, and anti-HADHB, respectively (Figure 16). Immunoblot analysis of mitochondria purified from *EHHADH*$_{WT}$ and *EHHADH*$_{MUT}$ cells, respectively, revealed HADHA to co-immunoprecipitate with HADHB. In addition, $EHHADH_{MUT}$ co-immunoprecipitated with HADHB, whereas no band was visible in mitochondria purified from *EHHADH*$_{WT}$ cells.

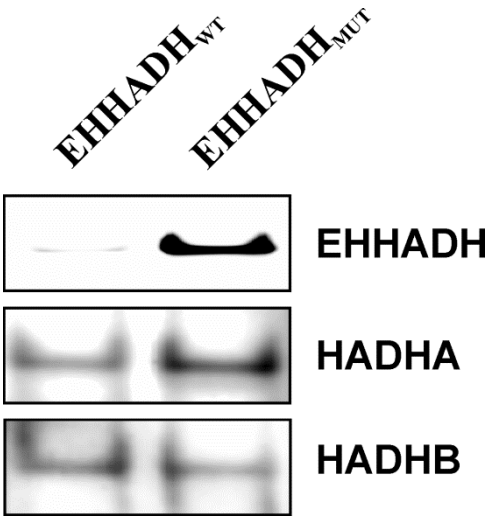

Figure 16: Co-immunoprecipitation of HADHB from purified mitochondria of *EHHADH*$_{WT}$ and *EHHADH*$_{MUT}$ cells, respectively, with subsequent immunoblot analysis using anti-EHHADH, anti-HADHA, and anti-HADHB antibodies. The immunoblot analysis shows a band for EHHADH in the *EHHADH*$_{MUT}$ cell line, whereas no band is visible for the *EHHADH*$_{WT}$ cell line. For HADHA and HADHB, similar levels are found in both the *EHHADH*$_{WT}$ and the *EHHADH*$_{MUT}$ cell line.

(Source: Klootwijk ED, Reichold M, Helip-Wooley A, et al. Mistargeting of peroxisomal EHHADH and inherited renal Fanconi's syndrome. N Engl J Med 2014;370:129-38.)

6.2.2 Blue native PAGE analysis

Blue native PAGE enables the separation of native protein complexes according to their mass. Purified mitochondria from *EHHADH*$_{WT}$ and *EHHADH*$_{MUT}$ cells were

analysed by blue native page followed by immunoblot analysis against HADHB and EHHADH (Figure17). The immunoblot against HADHB showed a band at about 500 kDa for both the *EHHADH$_{WT}$* and the *EHHADH$_{MUT}$* cells in concordance with the expected molecular weight of native MTP complex (Figure 17A). In contrast, only the *EHHADH$_{MUT}$* cell line yielded positive immunostaning against EHHADH at about 500 kDa, whereas the *EHHADH$_{WT}$* cell line lacked such signal (Figure 17B).

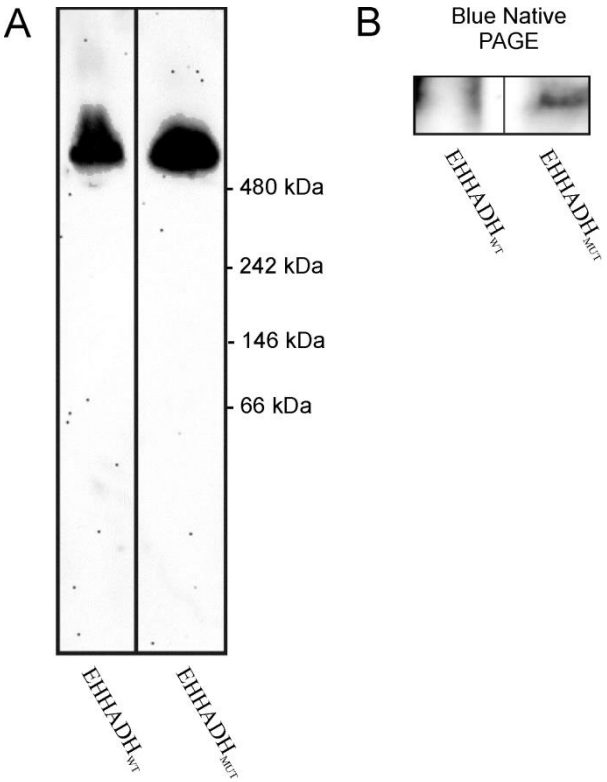

Figure 17: Immunoblot analysis of mitochondria purified from *EHHADH$_{WT}$* and *EHHADH$_{MUT}$* cells. A: Immunoblot analysis of blue native PAGE against HADHB. B: Immunoblot analysis of blue native PAGE against EHHADH.

(Source: Assmann et al., Unravelling the pathomechanism of an autosomal dominant Fanconi´s Syndrome: a mitochondriopathy caused by mistargeting of a peroxisomal protein. Cell Rep, in revision)

6.3 Respiratory chain analysis

6.3.1 High-resolution respirometry

High-resolution respirometry is a method to analyse mitochondrial respiration in intact cells, permeabilized cells or isolated mitochondria. By means of substrate-uncoupler-

inhibitor titration, it is possible to measure the function of individual complexes of the respiratory chain, or a combination of two or more complexes to exactly specify the site of disturbance in the respiratory chain. Results of high-resolution respirometry are shown in Figure 18. Endogeneous respiration of *EHHADH*$_{WT}$ and *EHHADH*$_{MUT}$ cell lines did not show a significant difference. Next, malate was added to stabilize the cells for subsequent permeabilization by the mild detergent digitonin. Following digitionin addition, the respiration was slightly decreased due to the absence of oxygen consuming side reactions that are not related to mitochondrial respiration. As substrate for β-oxidation, palmitoylcarnitine is added and the oxidative phosphorylation capacity via the electron transfer flavoprotein (ETF) is measured after the addition of ADP. The *EHHADH*$_{MUT}$ cell line showed a lower oxidative phosphorylation capacity than the *EHHADH*$_{WT}$ cell line. The addition of glutamate and pyruvate stimulates both complex I and ETF, so that one can determine their combined oxidative phosphorylation capacity. The oxygen consumption after the addition of glutamate and pyruvate did not increase further. *EHHADH*$_{MUT}$ cells still showed significantly decreased ($p = 0.003$) oxygen consumption compared to the *EHHADH*$_{WT}$ cell line. Cytochrome c is added to the chamber as a control for the integrity of the OMM. Damage done to the OMM during permeabilization causes leakage of cytochrome c into the buffer, with respiration becoming rate limiting as a consequence. A strong increase in respiration after the addition of exogeneous cytochrome c would therefore hint at damage of the OMM. Here, oxygen consumption after the addition of exogenous cytochrome c was hardly altered, thus confirming integrity of the OMM. Succinate is added as a substrate for complex II to reveal the maximum oxidative phosphorylation capacity in the coupled state. As before, the *EHHADH*$_{MUT}$ cell line showed a significant reduction ($p = 0.001$) in oxidative phosphorylation capacity compared to the *EHHADH*$_{WT}$ cell line. After the addition of succinate the difference in oxidative phosphorylation capacity between *EHHADH*$_{WT}$ and *EHHADH*$_{MUT}$ cell line was reduced to only 19 %, pointing towards a slight compensation in respiration differences, as the difference after the addition of palmitoylcarntine and pyruvate and glutamate (complex I) was 30 % and 33 %, respectively. ATP synthase is inhibited by the addition of oligomycin and the oxygen consumption which contributes to the LEAK respiration, is measured. The *EHHADH*$_{MUT}$ cell line showed a significantly decreased ($p = 0.005$) LEAK respiration compared to the *EHHADH*$_{WT}$ cell line. The addition of FCCP (Carbonyl cyanide p-

trifluoro-methoxyphenyl hydrazine) uncouples the electron transport of the respiratory chain from oxidative phosphorylation system. The mitochondrial respiration is typically limited by the oxidative phosphorylation system and, thus, after uncoupling the maximum respiration possible is measured. As the oxygen consumption of *EHHADH$_{MUT}$* cell line is still significantly decreased even after uncoupling, this displays that the defect in respiration is located in the oxidative phosphorylation machinery as well as in the electron transport system. After the rotenone-induced inhibition of complex I, the respiration of complex II in the uncoupled state was also reduced in the *EHHADH$_{MUT}$* cell line. The oxygen consumption linked to ATP production was calculated for the substrates pyruvate/glutamate and palmitoylcarnitine for complex I and ETF, respectively. For both substrates, oxygen consumption was reduced by 22 % and 35 % in *EHHADH$_{MUT}$* cells, respectively.

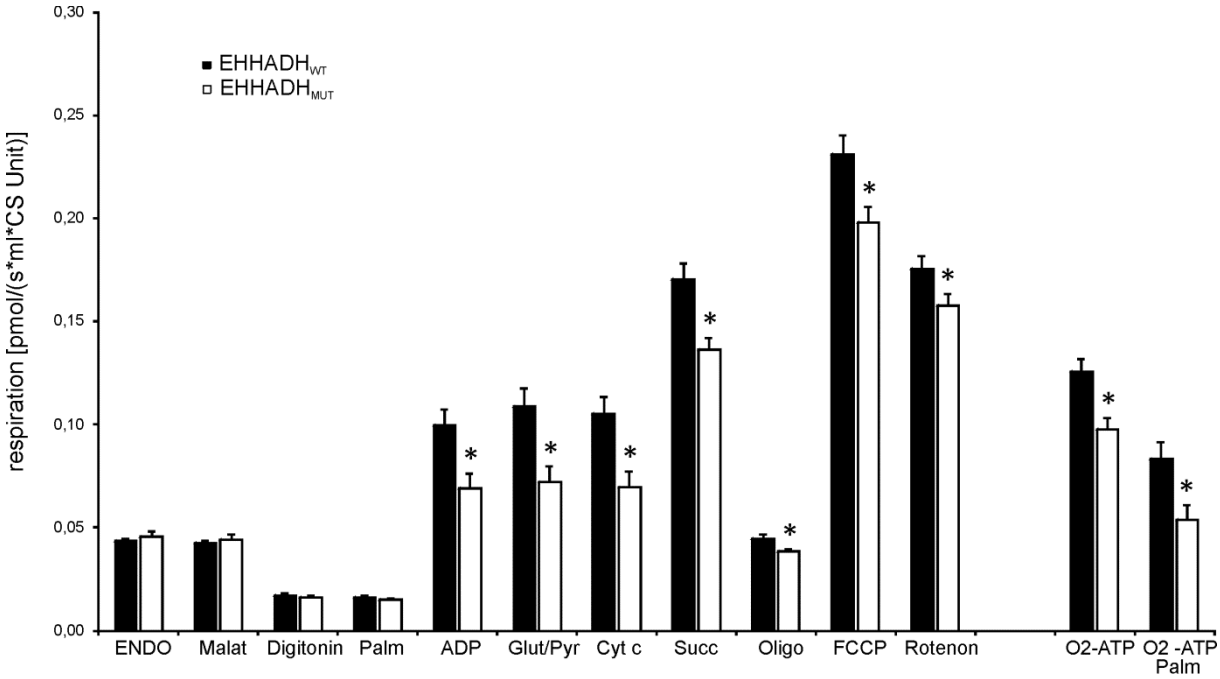

Figure 18: High-resolution respirometry analysis *of the EHHADH$_{WT}$* and *EHHADH$_{MUT}$* cell lines. Endo: enodgeneous respiration; Palm: palmitoylcarnitine; Glut/Pyr: glutamate and pyruvate; Cyt C: cytochrome c; Succ: succinate; Oligo: oligomycin; O2-ATP: calculated oxygen consumption linked to ATP production for the substrates glutamate and pyruvate; O2-ATP Palm: calculated oxygen consumption linked to ATP production for the substrate palmitoylcarnitine; values are means ± SEM; * FDR adjusted p-value ≤ 0.05.

The addition of palmitoyl-coenzyme A as an inhibitor of mitochondrial respiration is shown in Figure 19. Palmitoyl-CoA was exogeneously added to the chamber and led

to a significant, dose-dependent decrease in respiration at a concentration as low as 20 µM.

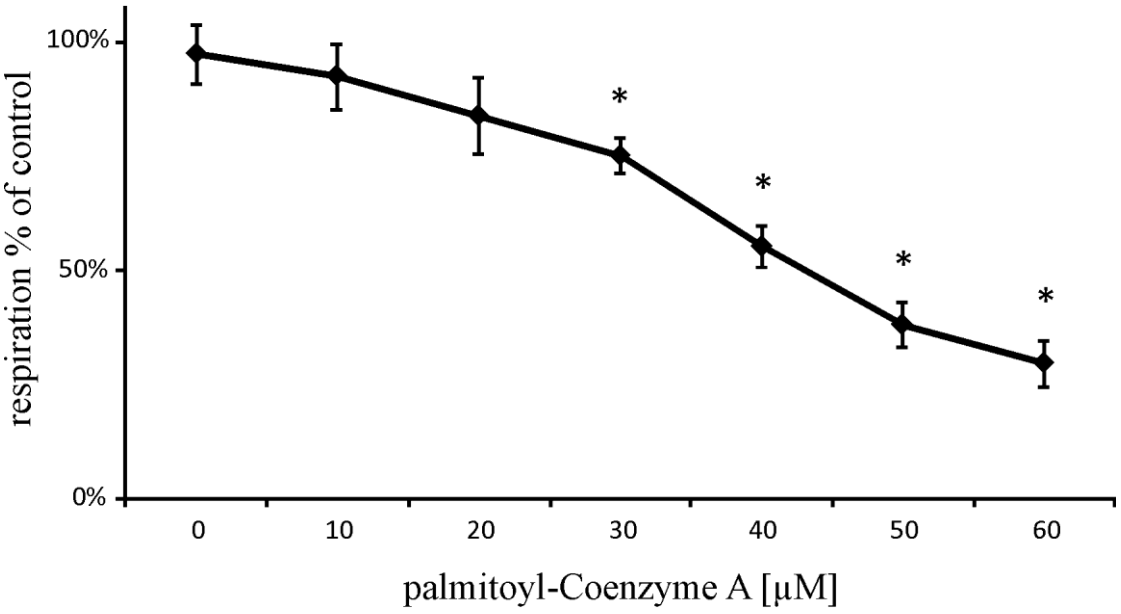

Figure 19: Inhibition of respiration by palmitoyl-CoA. The addition of palmitoyl-CoA to actively respiring permeabilized cells shows at a concentraton of 20 µM palmitoyl-CoA and higher a significant, dose-dependent decrease in respiration; shown are the means ± SEM of four independent measurements each; * ANOVA with pairwise t-test and FDR adjusted $p \leq 0.05$ (in relation to control).

An artificial inhibition, by palmitoyl-CoA, to the same level as *EHHADH*$_{MUT}$ cell line, was also accomplished. Thereby the impact of palmitoyl-CoA on mitochondrial respiration was investigated. Both cell lines showed the same percentage of inhibition of respiration for complex I and II in both the coupled and the uncoupled state.

6.3.2 Interaction analysis of EHHADH with the respiratory chain by 2D-blue native/ SDS-PAGE with subsequent immunoblot analysis

For the analysis of the interaction of EHHADH with the respiratory chain complexes and supercomplexes, 2D blue-native / SDS-PAGE was carried out. Isolated mitochondria from both the *EHHADH*$_{WT}$ and the *EHHADH*$_{MUT}$ cell line were separated according to their mass in their native state in the first dimension. In the second dimension, the respiratory chain complexes and supercomplexes were resolved into their individual subunits. The incorporation of EHHADT$_{MUT}$ within the respiratory

chain supercomplexes and the interaction of $EHHADH_{MUT}$ with complex I are shown by means of immunoblot analysis against EHHADH, whereas no band is visible for EHHADH in the *$EHHADH_{WT}$* cell line (Figure 20). In addition, a band was visible at ~ 500 kDa, the molecular mass of MTP, supporting once again the incorporation of $EHHADH_{MUT}$ into the MTP.

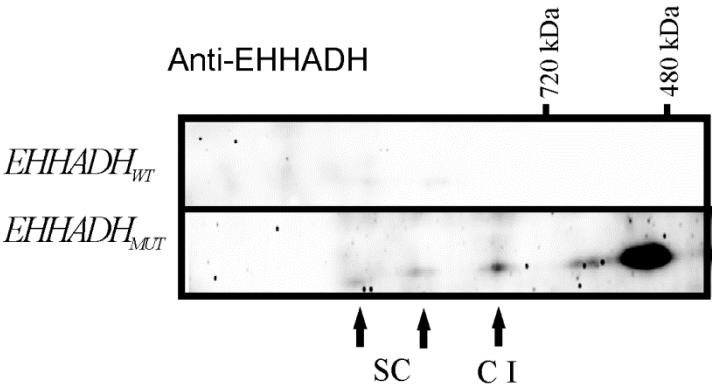

Figure 20: 2D blue native / SDS-PAGE analysis of isolated mitochondria from *$EHHADH_{WT}$* and *$EHHADH_{MUT}$* cell line with subsequent immunoblot analysis against EHHADH. In *$EHHADH_{MUT}$* cells a band for EHHADH is visible within the individual subunits of respiratory chain complex I and supercomplexes, indicating the interaction of $EHHADH_{MUT}$ with complexe I and respiratory chain supercomplexes. Also a band at ~ 500 kDa, the molecular mass of MTP, is visible in *$EHHADH_{MUT}$* cells.

(Source: Assmann et al., Unravelling the pathomechanism of an autosomal dominant Fanconi´s Syndrome: a mitochondriopathy caused by mistargeting of a peroxisomal protein. Cell Rep, in revision)

6.3.3 Quantification of supercomplex assembly

An exemplary 1D blue native PAGE, which was stained with SERVA Purple protein stain for quantification of supercomplex assembly, is shown in Figure 21A. Densitometric analysis (Figure 21B) with the Image Lab software showed a 44% decrease in supercomplex formation in the *$EHHADH_{MUT}$* cell line, from a supercomplex / complex V ratio of 0.7 ± 0.09 to 0.39 ± 0.05.

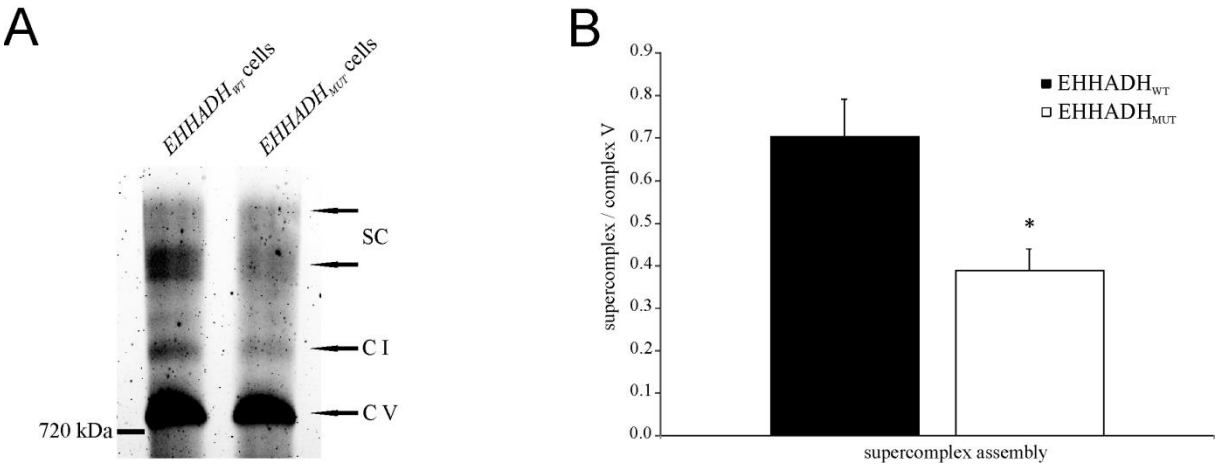

Figure 21: Quantification of supercomplex formation in mitochondria isolated from the EHHADH$_{WT}$ and *EHHADH$_{MUT}$* cell line, respectively. A: Exemplary 1D blue native PAGE stained with SERVA Purple protein stain. B: Densitometric analysis of supercomplex formation with the Image Lab software. Values represent means ± SEM; * $p \leq 0.05$.

(Source: Assmann et al., Unravelling the pathomechanism of an autosomal dominant Fanconi´s Syndrome: a mitochondriopathy caused by mistargeting of a peroxisomal protein. Cell Rep, in revision)

6.4 Metabolic analysis

6.4.1 Palmitic acid uptake

To calculate uptake rates of palmitic acid in *EHHADH$_{MUT}$* and *EHHADH$_{WT}$* cells, changes in palmitic acid levels in cell culture media over 48 hours were measured by means of GC-MS. The *EHHADH$_{MUT}$* cell line took up significantly less ($p = 0.016$) palmitic acid (Fig 22).

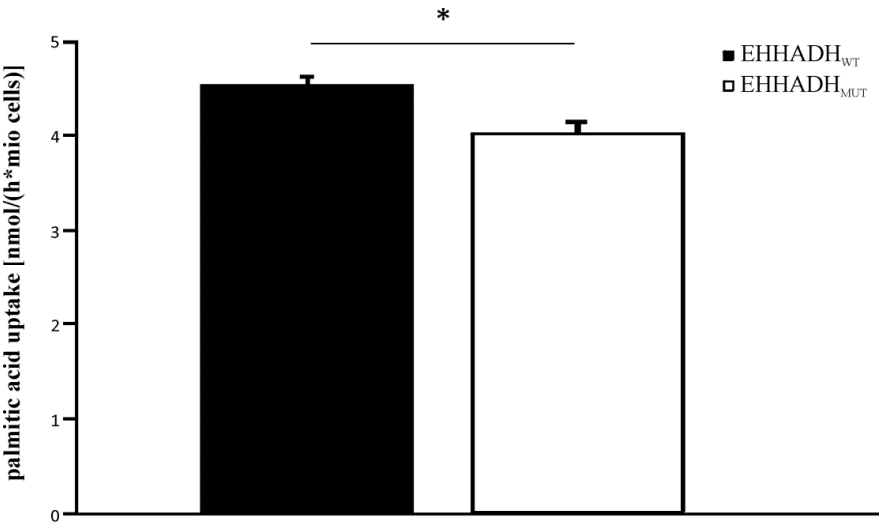

Figure 22: Analysis of palmitic acid uptake by *EHHADH$_{WT}$* and *EHHADH$_{MUT}$* cells. The *EHHADH$_{MUT}$* cell line takes up significantly less palmitic acid. Values are means ± SEM; * $p \leq 0.05$.

(Source: Assmann et al., Unravelling the pathomechanism of an autosomal dominant Fanconi´s Syndrome: a mitochondriopathy caused by mistargeting of a peroxisomal protein. Cell Rep, in revision)

6.4.2 Metabolic analysis of acetyl-CoA

LC-MS/MS analysis of unlabeled, intracellular levels of acetyl-CoA did not show a significant difference between the *EHHADH$_{WT}$* and the *EHHADH$_{MUT}$* cell line. However, the analysis of ^{13}C-labelled acetyl-CoA in cells grown on ^{13}C-labelled palmitic acid, showed a significantly reduced level ($p < 0.04$) of ^{13}C-labelled acetyl-CoA in the *EHHADH$_{MUT}$* cell line upon normalization to total acetyl-CoA (Fig 23).

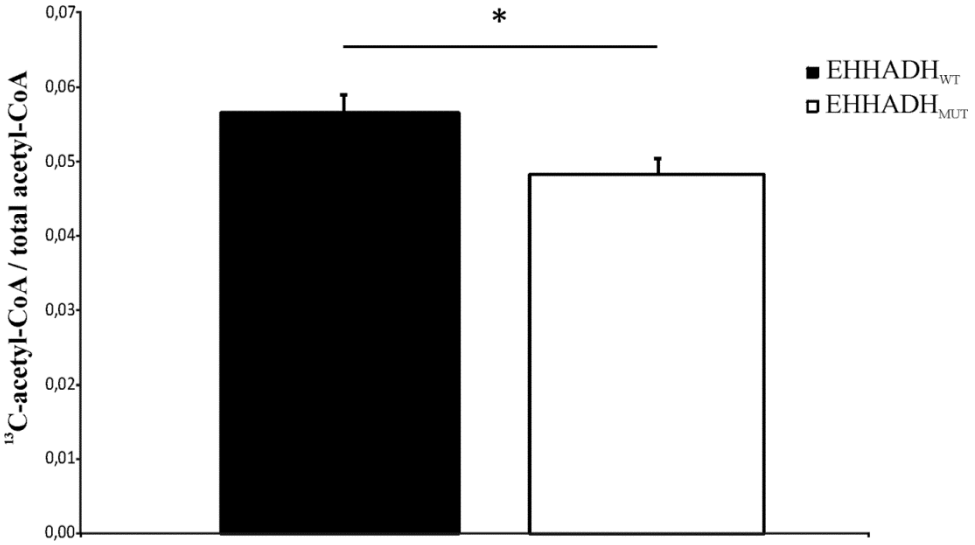

Figure 23: LC-MS/MS analysis of ^{13}C-labelled acetyl-CoA in the *EHHADH$_{WT}$* and *EHHADH$_{MUT}$* cell lines. *EHHADH$_{MUT}$* cell line showed a decreased level of ^{13}C-labelled acetyl-CoA, when grown on ^{13}C-labelled palmitic acid, compared to *EHHADH$_{WT}$* cell line. Values are means ± SEM; * p-value ≤ 0.05.

(Source: Assmann et al., Unravelling the pathomechanism of an autosomal dominant Fanconi´s Syndrome: a mitochondriopathy caused by mistargeting of a peroxisomal protein. Cell Rep, in revision)

6.4.3 Acylcarnitne analysis

Acylcarnitine analysis is an essential tool for screening of fatty acid β-oxidation defects. The analysis of long-chain acylcarnitines in cell culture supernatant (Figure 24) showed a significant increase in long-chain acylcarnitines as well as long-chain ketoacyl- and hydroxyacylcarntines in *EHHADH$_{MUT}$* cells compared to *EHHADH$_{WT}$* cells. The extracellular concentration of 3-hydroxyhexadecanoylcarnitine ((4S)-4-[(3-hydroxyhexadecanoyl)oxy]-4-(trimethylazaniumyl)butanoate) was even below the detection limit of the method in the *EHHADH$_{WT}$* cell line.

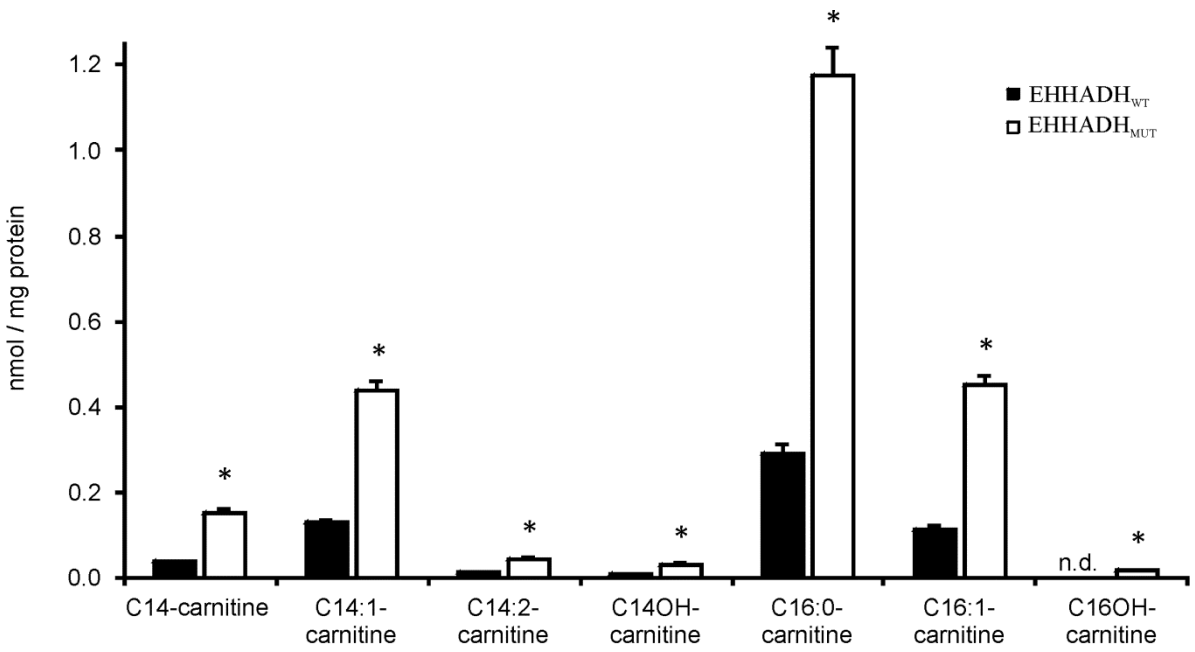

Figure 24: Analysis of long-chain acylcarnitines in cell culture supernatants. Compared to *EHHADH$_{WT}$* cells, levels of long-chain acylcarnitines as well as ketoacyl- and hydroxyacyl carnitines were significantly elevated in *EHHADH$_{MUT}$* cells. In *EHHADH$_{WT}$* cells, 3-hydroxyhexadecanoylcarntine could not be quantified. Values are means ± SEM; * FDR adjusted p-value ≤ 0.05.

(Source: Assmann et al., Unravelling the pathomechanism of an autosomal dominant Fanconi´s Syndrome: a mitochondriopathy caused by mistargeting of a peroxisomal protein. Cell Rep, in revision)

6.4.4 Measurement of ATP content

The *EHHADH$_{MUT}$* cell line showed a significantly decreased ($p < 0.012$) content of ATP (1.74 ± 0.26 nmolATP / mg protein) compared to the *EHHADH$_{WT}$* cell line (3.15 ± 0.14 nmol ATP / mg protein).

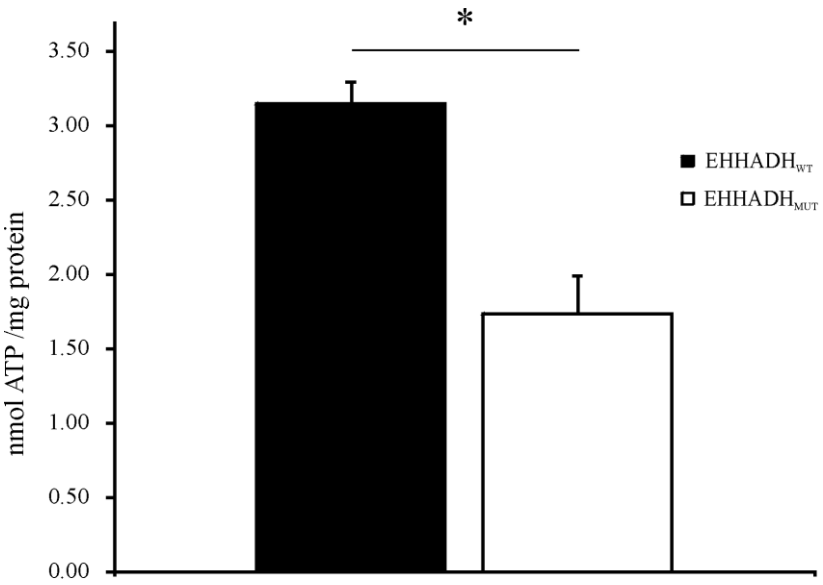

Figure 25: Measurment of ATP content in the *EHHADH$_{WT}$* and *EHHADH$_{MUT}$* cell lines. Values are means ± SEM; * p ≤ 0.05. As glycerol phosphate generates background in this assay, for every measured sample a background measurement was carried out from the same sample. Afterwards, the value of the background was substracted from the value of the sample prior to further calculations.

(Source: Assmann et al., Unravelling the pathomechanism of an autosomal dominant Fanconi´s Syndrome: a mitochondriopathy caused by mistargeting of a peroxisomal protein. Cell Rep, in revision)

6.5 Proteomic analysis

The SWATH-MS™ analysis revealed a significant regulation of proteins involved in the respiratory chain, fatty acid β-oxidation and the tricarboxylic acid cycle (Table 6). Seven out of ten identified subunits of complex I were significantly downregulated in the *EHHADH$_{MUT}$* cell line. For complex III, no clear trend in regulation was obvious: one of the two out of five subunits identified was significantly downregulated, while the other one was markedly up-regulated in the *EHHADH$_{MUT}$* cell line. For complex IV, two out of six identified subunits were significantly down-regulated in the *EHHADH$_{MUT}$* cell line. Only four out of fourteen complex V subunits were significantly regulated, but they did not show the same trend of regulation, as two subunits each were either significantly down- or upregulated. In addition, several constituents of fatty acid β-oxidation were significantly regulated. The peroxisomal multifunctional protein type 2 was significantly downregulated in the *EHHADH$_{MUT}$* cell line, whereas peroxisomal bifunctional isoform 1 and acyl-CoA binding protein were significantly

upregulated. In addition, the ADP/ATP translocase 2 and mitochondrial dicarboxylate carrier isoform 2 were significantly downregulated in *EHHADH$_{MUT}$* cell line.

Table 6: Results of Swath™ analysis. The table lists the respective NCBI accession numbers, the functional class membership of a protein, the fold-change observed in the *EHHADH$_{MUT}$* cell line, and the calculated p-values. Negative fold-changes mean a down-regulation and positive fold-changes an up-regulation in the *EHHADH$_{MUT}$* cell line.

NCBInr Accession	Protein Functional Class	Fold-change	p-value
Respiratory Chain			
gi|311276243	PREDICTED: NADH dehydrogenase [ubiquinone] 1 beta subcomplex subunit 11, mitochondrial-like isoform 2 [Sus scrofa]	-3,7	5,3844E-06
gi|511887496	PREDICTED: NADH dehydrogenase [ubiquinone] 1 subunit C2 [Mustela putorius furo]	-8,0	8,6342E-05
gi|432102533	NADH dehydrogenase [ubiquinone] 1 beta subcomplex subunit 10 [Myotis davidii]	-8,2	0,00087
gi|516267059	NADH dehydrogenase subunit I [Blastomonas sp. AAP53]	-5,4	0,01125
gi|311272935	PREDICTED: NADH-ubiquinone oxidoreductase 75 kDa subunit, mitochondrial isoform 1 [Sus scrofa]	-2,1	0,01273
gi|83286812	NADH-ubiquinone oxidoreductase complex [Bos taurus]	-2,2	0,01676
gi|335310208	PREDICTED: NADH dehydrogenase [ubiquinone] 1 beta subcomplex subunit 4-like [Sus scrofa]	-2,5	0,03047
gi|73994981	PREDICTED: cytochrome b-c1 complex subunit 9 isoform 2 [Canis lupus familiaris]	-4,1	0,00029
gi|350581652	PREDICTED: cytochrome b-c1 complex subunit 2, mitochondrial-like [Sus scrofa]	7,6	0,02365
gi|350584800	PREDICTED: cytochrome c oxidase subunit 4 isoform 1, mitochondrial-like [Sus scrofa]	-3,3	0,00017
gi|471368705	PREDICTED: cytochrome c oxidase subunit 5A, mitochondrial-like [Trichechus manatus latirostris]	-5,6	0,02243
gi|529007286	PREDICTED: ATP synthase subunit f, mitochondrial isoform X2 [Bos taurus]	-12,8	0,00106
gi|113205874	ATP synthase subunit O, mitochondrial precursor [Sus scrofa]	-12,6	4,3098E-07
gi|350580769	PREDICTED: ATP synthase subunit delta, mitochondrial-like [Sus scrofa]	2,2	0,00214
gi|465982382	PREDICTED: ATP synthase subunit e, mitochondrial [Orcinus orca]	2,4	0,01472

Table 6 (continued)

NCBInr Accession	Protein Functional Class	Fold-change	p-value
Fatty acid β-oxidation			
gi|47523670	peroxisomal multifunctional enzyme type 2 [Sus scrofa]	-2,4	0,01141
gi|68989263	peroxisomal bifunctional enzyme isoform 1 [Homo sapiens]	6,3	0,00032
gi|47523046	acyl-CoA-binding protein [Sus scrofa]	3,0	0,01409
Mitochondrial transporters			
gi|512904223	PREDICTED: ADP/ATP translocase 2 [Heterocephalus glaber]	-20,6	0,00025
gi|470595839	PREDICTED: mitochondrial dicarboxylate carrier isoform 2 [Tursiops truncatus]	-2,8	0,00254

7 Discussion

7.1 Localization and mistargeting of $EHHADH_{MUT}$

Proteins containing a peroxisomal targeting sequence are imported into peroxisomes in their fully folded or oligomeric state [60], with further processing occurring only for a subset of proteins. In contrast, proteins featuring a mitochondrial targeting sequence are imported in their unfolded state and the N-terminal mitochondrial targeting sequence is cleaved after the import into the mitochondrial matrix, leading to a shortened mature protein [59].

The peroxisomal protein EHHADH, which is involved in peroxisomal fatty acid oxidation, features the typical peroxisomal C-terminal targeting sequence SKL. The mutation p.E3K, which replaces a negatively charged glutamic acid residue with a positively charged lysine, generates a novel mitochondrial targeting sequence at the N-terminal end. Cleavage of this mitochondrial targeting sequence upon import is indicated by the well-resolved double band on gels of whole cell lysate, indicating a shift of ~ 2 kDa in size (Figure 13). Actually, $EHHADH_{MUT}$ is only partly mistargeted into mitochondria. Most is still targeted to peroxisomes, as shown by immunofluorescence staining (Figure 14F), where in addition to the mislocalized $EHHADH_{MUT}$ (yellow areas), $EHHADH_{MUT}$ was mainly localized to the peroxisomes. Furthermore, in immunoblot analysis of *$EHHADH_{MUT}$* cells was shown that in addition to the mitochondrial localized $EHHADH_{MUT}$, indicated by the band in the mitochondrial fraction of *$EHHADH_{MUT}$* cells, we also saw a band for the peroxisomal localized $EHHADH_{MUT}$, appearing at the same height as the wild type EHHADH. The erroneous localization of $EHHADH_{MUT}$ is not a specific phenomenon of the cell line LLC-PK1, as transfection of COS7 and HEK293 cells also showed mistargeting of $EHHADH_{MUT}$ [67].

Mutation of EHHADH also causes changes in the proteins´ properties. The isoelectric point of a protein is defined at the pH, at which the protein carries no electric net charge. For $EHHADH_{WT}$ protein, the pI is 9.8 [64], and through the exchange of a negatively changed amino acid against a basic amino acid, the pI of the protein shifts to a slightly more basic value. However, taking into account the import of $EHHADH_{MUT}$ into mitochondria and the cleavage of the mitochondrial targeting sequence, the pI will become more acidic. In 2D-DIGE, a shift of $EHHADH_{MUT}$ to the

basic is seen. The major part of $EHHADH_{MUT}$ is still localized to the peroxisomes, thereby the exchange of an amino acid influencing the pI is apparent more than the cleavage of the mitochondrial targeting sequence. Thus, an overall shift of the pI of $EHHADH_{MUT}$ is seen more to the basic.

7.2 Erroneous interaction of $EHHADH_{MUT}$ with the mitochondrial trifunctional protein

Mistargeting of $EHHADH_{MUT}$ into mitochondria leads to the interaction of $EHHADH_{MUT}$ with the mitochondrial trifunctional protein (MTP) as shown by co-immunoprecipitation. As part of the mitochondrial β-oxidation spiral of fatty acids, MTP catalyzes the last three steps of mitochondrial β-oxidation of long-chain fatty acids. The MTP consists of four alpha subunits, HADHA, bearing the enoyl-CoA hydratase and the L-3-hydroxyacyl-CoA dehydrogenase activity, and four beta subunits, HADHB, bearing the ketoacyl-CoA thiolase activity. Together, they build a heterooctamer, which is located in the IMM. Co-immunoprecipitation against EHHADH led to the identification of HADHA and HADHB as potential interaction partners of $EHHADH_{MUT}$. For verification of this interaction, co-immunoprecipitation against HADHB was performed. The corresponding immunoblot yielded a band for *$EHHADH_{MUT}$* cells, whereas no band was visible for *$EHHADH_{WT}$* cells, indicating an interaction of $EHHADH_{MUT}$ with MTP.

This interaction was investigated in more detail by means of blue native PAGE, which separates protein complexes according to their native state. Blue native PAGE of mitochondria purified from both *$EHHADH_{WT}$* and *$EHHADH_{MUT}$* cells with subsequent immunoblot analysis against EHHADH and HADHB was performed. The immunoblot analysis against EHHADH (Figure 17B) showed for $EHHADH_{WT}$ no band, whereas for $EHHADH_{MUT}$ a band was visible at ~ 500 kDa, corresponding to the expected molecular weight of intact MTP complex, thus confirming once more the interaction of $EHHADH_{MUT}$ with the native MTP complex.

Interaction of $EHHADH_{MUT}$ with MTP may occur in two ways, either by the additional attachment of an $EHHADH_{MUT}$ subunit to the MTP complex, or via the replacement of an MTP subunit against an $EHHADH_{MUT}$. An additional attachment of $EHHADH_{MUT}$ to the complex will enlarge the molecular mass of the complex by ~ 77 kDa. The fact,

that no such shift was observed in the immunoblot against HADHB (Figure 17A), points towards an exchange of $EHHADH_{MUT}$ for a subunit of the MTP, instead of an additional attachment of $EHHADH_{MUT}$ to the complex.

The native EHHADH has a mass of 79 kDa, and $EHHADH_{MUT}$ after processing in the mitochondrial matrix has a mass of ~ 77 kDa. The masses of the alpha and beta subunits of MTP are 79 kDa and 47 kDa, respectively. While an exchange for a beta-subunit will result in an increase of ~ 30 kDa, an exchange for an alpha-subunit will increase the mass of the MTP complex by only ~ 2 kDa. Therefore, the observed result points towards an exchange of $EHHADH_{MUT}$ for the alpha-subunit of the complex rather than an additional attachment of $EHHADH_{MUT}$ to the complex or the exchange of a beta-subunit.

7.3 Effects of mistargeting of $EHHADH_{MUT}$ on mitochondrial fatty acid β-oxidation

Incorporation of $EHHADH_{MUT}$ into the MTP leads to impairment of mitochondrial β-oxidation of long-chain fatty acids. As a consequence, long-chain acylcarnitines accumulate in the cell culture supernatant (Figure 25). A well-known clinical parameter for fatty acid oxidation disorders is acylcarnitine profiling in neonates by tandem mass spectrometry (MS/MS) [73-78]. As fatty acid oxidation disorders (FAOD) are an often fatal inherited group of metabolic disorders, it is important to diagnose these disorders pre-symptomatically by newborn screening, to reduce infant mortality rate and start early with an appropriate diet. The *$EHHADH_{MUT}$* cell line showed increased amounts of tetradecanoylcarnitne and hexadecanoylcarnitine and their corresponding long-chain enoyl- and hydroxyacylcarnitines in the cell culture supernatant. This increase in long-chain acylcarnitines and their fatty oxidation intermediates are indicative for an impairment of mitochondrial β-oxidation in the *$EHHADH_{MUT}$* cell line. Impaired mitochondrial β-oxidation leads to accumulation of imported long-chain acyl-CoAs and intermediates of mitochondrial β-oxidation. As these compounds are harmful to cellular functions, they are exported via the CPT II and CACT in the reverse direction out of the mitochondria into the cytosol and are excreted from the cell as their corresponding long-chain acylcarnitine, by a yet unknown mechanism [79]**.** Ventura et al. [79] showed that CPT II accepts palmitoyl-CoA as well as its β-oxidation intermediates as substrates, which are transported by the

carnitine-acylcarnitine translocase into the cytosol and exported out of the cell. This reverse action of CPT II and CACT lowers the intramitochondrial amount of cytotoxic long-chain acyl-CoAs and recycles coenzyme A (CoA). Zierz et al. [80] also showed, that the forward reaction of total CPT was inhibited by 0.1 mM D,L-palmitoylcarnitine by 55 %. This inhibtion of the total CPT forward reaction was only present for L- and D,L-palmitoylcarntinine but not for D-palmitoylcarnitine, indicating that the effect was due to a substrate inhibition and not a detergent-like effect [80]. In addition, they also stated that the CPT fraction, which showed the inhibition by palmitoylcarnitine, represented the CPT II activity [80].

Further, both Zierz et. al. [80] and Ventura et. al. [79] showed, that the accumulation of long-chain acylcarnitines led to substrate inhibition of the forward reaction of CPT II and increased the reverse reaction of CPT II and CACT leading to the export of long-chain acylcarnitines into the cytosol and out of the cell. The extracellular level of long-chain acylcarnitines and their fatty acid oxidation intermediates resemble the situation in patients with MTP deficiency [81], although in a less severe form. This is not surprising, as in contrast to MTP deficiency not all MTP complexes are expected to contain $EHHADH_{MUT}$. Consequently, mitochondrial β-oxidation is affected less than in classical cases of inherited MTP deficiency.

7.4 Impact of impaired mitochondrial fatty acid β-oxidation on other cellular mechanisms

The disturbance of mitochondrial fatty acid β-oxidation affects other pathways and molecular mechanisms up- and downstream of β-oxidation.

7.4.1 Uptake of exogeneous long-chain fatty acids

The uptake of palmitic acid over a period of 48 hours was reduced significantly in the $EHHADH_{MUT}$ cell line (Figure 22). Import of fatty acids (FA) across the cellular membrane is facilitated by two processes, diffusion and protein-mediated import by FATPs. Diffusion is one possible way to support metabolism, when FAs are present at high concentrations. However, under physiological conditions, diffusion is not sufficient to supply enough FA for energy generation, so that a protein-mediated mechanism is required to efficiently mediate transbilayer transport of FAs [82,83]. Integral membrane-bound fatty acid transport proteins (FATPs) facilitate the transport

of FAs into the cell. To prevent the efflux of the FAs, they are activated by the action of acyl-CoA synthetases. This process is ATP dependent and, therefore, depletion of ATP may cause decreased uptake of FAs. The uptake of long-chain fatty acids via protein-mediated mechanisms are also regulated by downstream factors, like mitochondrial long-chain fatty acid uptake, re-esterification, and β-oxidation [83]. These downstream factors can lead to a saturation of cytosolic fatty acid binding proteins (FABP) and acyl-coA binding proteins (ACBP). The uptake and subsequent activation of long-chain fatty acids are strongly regulated by long-chain acyl-CoAs, intracellular ATP and the mitochondrial carnitine transport system.

Product-inhibition of long-chain acyl-CoA synthetases

Acyl-CoA synthetases are inhibited by the product of the reaction, acyl-CoAs, and by a decrease in the intracellular CoA pool [84,85]. Inhibition of acyl-CoA synthetase by accumulation of long-chain β-oxidation intermediates has been reported [86,87]. Impaired β-oxidation in the *EHHADH*$_{MUT}$ cell line might thereby lead to a decreased activation of FAs and to an increased efflux. As a consequence, the actual uptake of palmitic acid into the *EHHADH*$_{MUT}$ cells is decreased. *In vivo*, this event is unlikely to occur, as the presence of FABPs and ACBPs sequester long-chain fatty acids and, thereby, eliminate their inhibiting action. In the *EHHADH*$_{MUT}$ cell line, an increase in acyl-CoA binding protein is shown, which in part counter-regulates in *EHHADH*$_{MUT}$ cells the accumulation of β-oxidiation intermediates.

Regulation of cellular long-chain fatty acid uptake by the intracellular ATP level

Activation of long-chain fatty acids is an ATP-dependent process. Lowering the intracellular ATP content decreases acyl-CoA synthetase activity and thereby activation of long-chain fatty acids to their acyl-CoAs [82,84]. The *EHHADH*$_{MUT}$ cell line shows a decreased level of cellular ATP compared to *EHHADH*$_{WT}$ cells. This fact also fits the decreased uptake of palmitic acid in *EHHADH*$_{MUT}$ cells.

Decreased activation of the mitochondrial carnitine transport system

Accumulation of β-oxidation intermediates inhibits β-oxidation by product inhibition. This accumulation inhibits the forward reaction of CPT II and activates the reverse reaction for the export of the corresponding long-chain acylcarnitines. The inhibition of the forward reaction of CPT II leads to a saturation of cytosolic FABPs and ACBPs

and, thereby, to a decreased uptake of long-chain fatty acids across the cellular membrane.

In summary, mistargeted $EHHADH_{MUT}$ is incorporated into MTP and impairs mitochondrial β-oxidation, shown by the accumulation of long-chain acylcarnitines. This accumulation inhibits the forward reaction of CPT II and enhances the export of long-chain acylcarnitines out of the cell. These cellular mechanisms downstream of long-chain fatty acid uptake, lead overall to a decreased uptake of long-chain fatty acids (Figure 26).

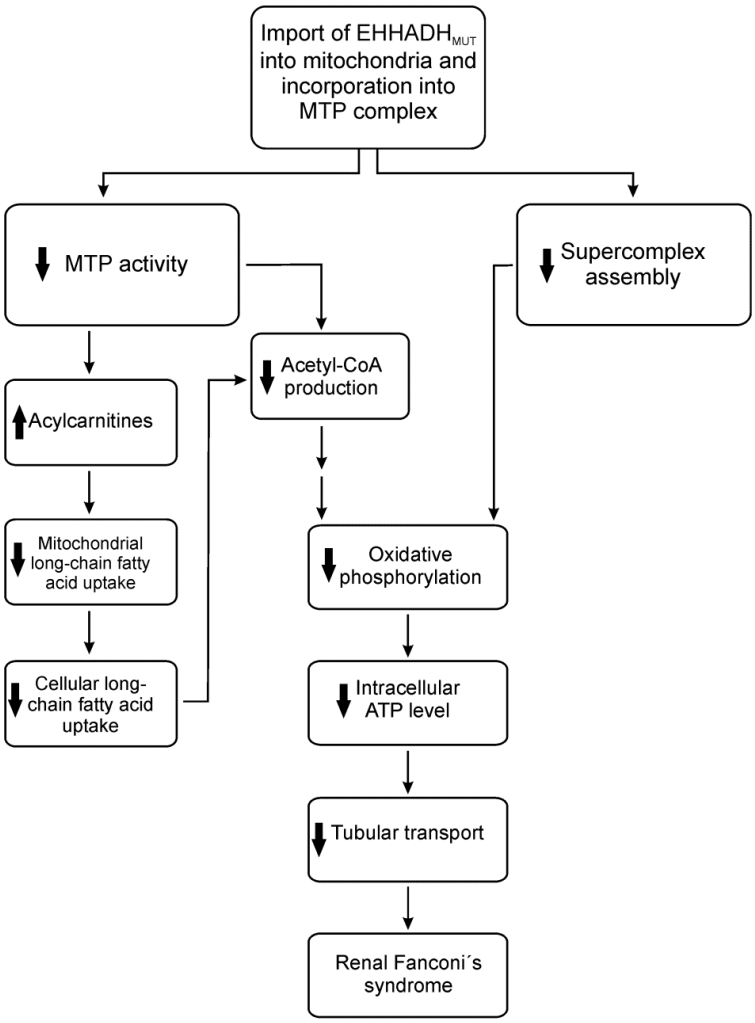

Figure 26: Schematic representation of impaired mitochondrial function due to $EHHADH_{MUT}$ mistargeting. Mistargeting of $EHHADH_{MUT}$ into mitochondria and incorporation into MTP complex leads to an impaired mitochondrial β-oxidation and a decreased mitochondrial supercomplex assembly. Both result in reduced oxidative phosphorylation and, thereby, in a reduced intracellular ATP level in the *$EHHADH_{MUT}$* cell line. This in turn decreases proximal tubular reabsorption of

electrolytes, amino acids, glucose and other low molecular weight compounds, leading to the Fanconi´s syndrome (↑↓: up/down-regulation).
(Source: Assmann et al., Unravelling the pathomechanism of an autosomal dominant Fanconi´s Syndrome: a mitochondriopathy caused by mistargeting of a peroxisomal protein. Cell Rep, in revision)

7.4.2 Formation of acetyl-CoA from β-oxidation

Acetyl-CoA, as the endproduct of mitochondrial β-oxidation, is directly fed into the tricarboxylic acid cycle for further metabolisation to produce reducing equivalents (NADH and $FADH_2$) and ATP. Normal mitochondrial β-oxidation of one molecule palmitic acid leads to the formation of 8 molecules of acetyl-CoA [88]. Impaired mitochondrial β-oxidation leads to decreased levels of acetyl-CoA. Its flux through the tricarboxylic acid cycle is decreased and, as a result, less energy is produced.
Impaired mitochondrial β-oxidation in *EHHADH*$_{MUT}$ cells was demonstrated by cell culture experiments with palmitic acid. Subsequent analysis showed decreased formation of ^{13}C-labelled acetyl-CoA in *EHHADH*$_{MUT}$ cells. Absolute intracellular levels of acetyl-CoA, however, did not differ between *EHHADH*$_{WT}$ and *EHHADH*$_{MUT}$ cells, as shown by the measurement of unlabeled acetyl-CoA. The *EHHADH*$_{MUT}$ cell line appears to compensate for the decreased formation of acetyl-CoA from mitochondrial β-oxidation by deriving acetyl-CoA from other pathways, such as its generation from ketogenic amino acid (lysine, tryptophan, leucine, and isoleucine).

7.4.3 Generation of ATP

In renal proximal tubular cells, the ion gradient across the plasma membrane is a precondition for renal tubular reabsorption. It is generated by ATP-dependent sodium-potassium pump, Na^+/K^+-ATPase. The energy needed is generated by oxidative metabolism in proximal tubular cells.
Fatty acids are the main source of energy in proximal tubules even in the presence of other metabolites [23,42]. Gullans et al. [89] showed, that after the addition of 0.1 µM rotenone, the oxygen consumption and ATP content in cortical tubule suspension of rabbits are reduced to the same degree. This demonstrates, that ATP in renal proximal tubular cells is mainly supplied by oxidative phosphorylation, as addition of

the respiratory chain complex I inhibitor rotenone decreased the ATP level decreased to the same degree as oxidative phosphorylation was inhibited. In addition, the decrease in ATP content after the addition of rotenone correlated with reduced proximal tubular cell transport. Further, Beck et al. [24] showed a reduction in intracellular ATP level by approximately 40 % after the stimulation of sodium transport in isolated rabbit proximal convolute tubule for eight minutes. This drop in intracellular ATP after stimulation of sodium transport shows that the level of ATP is close to the cellular energy demand in proximal tubular cells. The continuous supply with ATP for proximal tubular cells is thus of great importance, as the stored ATP can maintain tubular transport for a few seconds only [90]. The intracellular ATP levels in *EHHADH*$_{WT}$ cells are in good accordance with former published data on ATP levels in the LLC-PK1 cell line [91], isolated renal tubules [92], and Madin-Darby canine kidney cells [93], whereas intracellular ATP is decreased in the *EHHADH*$_{MUT}$ cell line, which is likely to explain the decreased transport activity observed in EHHADH$_{MUT}$ overexpressing cells [67].

7.5 Global proteomic analysis of the *EHHADH$_{WT}$* and *EHHADH$_{MUT}$* cell lines

The proteomic analysis of different physiological states, e.g. wild type and mutated cell lines, is a common means to elucidate the molecular mechanisms underlying cellular processes [94]. SWATH-MS™ analysis of the *EHHADH$_{WT}$* and *EHHADH$_{MUT}$* cell lines revealed significant differences in the abundance of constituents of the mitochondrial respiratory chain, mitochondrial and peroxisomal β-oxidation, and mitochondrial transporters.

The decreased amounts of several complex I members shown by SWATH-MS™ analysis in *EHHADH$_{MUT}$*-transfected cells can be explained by the decreased supercomplex formation, as the formation of mitochondrial supercomplexes is important for the stability of complex I [95-97]. In these publications, mutation of complex III led to decreased stability of complex I and its subsequent degradation.

SWATH-MS™ analysis also showed a down-regulation of peroxisomal multifunctional enzyme type 2 (D-bifunctional protein) and an up-regulation of peroxisomal bifunctional enzyme isoform 1 (EHHADH) and acyl-CoA binding protein in whole cell lysate of the *EHHADH$_{MUT}$* cell line. Down-regulation of D-bifunctional protein is presumably an overexpression artefact in the *EHHADH$_{WT}$* cell line, as due to the strong increase in EHHADH protein amount in peroxisomes, the cell counter-regulates the amount of D-bifunctional protein. This effect is not as strong in the *EHHADH$_{MUT}$* cell line due to the dual localization of EHHADH$_{MUT}$, thereby reducing the effective concentration within the peroxisomes. Up-regulation of EHHADH is also explained by the mistargeting of mutated EHHADH into mitochondria. As EHHADH in *EHHADH$_{WT}$* cell line is only localized to peroxisomes, the overexpression leads to a saturation of EHHADH in peroxisomes and to subsequent degradation of the protein. In contrast, in the *EHHADH$_{MUT}$* cell line, EHHADH is localized to both, peroxisomes and mitochondria. Therefore, EHHADH overexpression in *EHHADH$_{MUT}$* cell line is not as limited as in the *EHHADH$_{WT}$* cell line. The increase in acyl-CoA binding protein in *EHHADH$_{MUT}$* cell line may be explained by the accumulation of β-oxidation intermediates and thereby by an increased demand of acyl-CoA binding proteins for the sequestration of these toxic intermediates.

In addition, mitochondrial transporters are significantly downregulated in the *EHHADH$_{MUT}$* cell line. The mitochondrial dicarboxylate carrier transports malate and succinate out of the mitochondrium in exchange for phosphate [98], whereas the

ADP/ATP translocase transports ATP out of the mitochondrial matrix in exchange for cytosolic ADP [99]. It is already known, that impaired mitochondrial β-oxidation and the resulting accumulation of β-oxidation intermediates inhibit these mitochondrial carriers [100-103]. For the ADP/ATP translocase it has been reported, that long-chain acyl-CoAs inhibit the activity on the cytosolic and mitochondrial side of the IMM [103,104]. Ciapaite et al. [101] found that palmitoyl-CoA inhibits only the exchange of mitochondrial ATP against cytosolic ADP and has no effect of mitochondrial ATP synthesis. The inhibition of both, dicarboxylate carrier and ADP/ATP translocase, may thereby lead to a decreased amount ATP in *EHHADH$_{MUT}$* cells.

7.6 Effects of mistargeting of EHHADH$_{MUT}$ on mitochondrial respiration and supercomplex formation

Mitochondrial β-oxidation and mitochondrial oxidative phosphorylation are tightly coupled processes, as reducing equivalents are directly fed into the respiratory chain. $FADH_2$ is generated during the oxidation of long-chain acyl-CoA. The electrons from $FADH_2$ enter directly the respiratory chain via the electron transfer flavoprotein (ETF). The electrons from the reduced ETF are then transferred onto ubiquinone, which is accomplished by the ETF:ubiquinone oxidoreductase, to build ubiquinol. Complex III reoxidized ubiquinol to ubiquinone and the electrons are transferred onto the respiratory chain complex. The second reducing equivalent formed during β-oxidation is NADH. The NAD^+-dependent oxidation of L-3-hydroxyacyl-CoAs to 3-ketoacyl-CoA is catalyzed by L-3-hydroxyacyl-CoA dehydrogenase. NADH enters the respiratory chain at complex I. In addition, Sumegi et al. [105] showed binding of thiolase and L-3-hydroxyacyl-CoA dehydrogenase to complex I, which is believed to enhance the efficient shuttling of NADH produced by β-oxidation to respiratory chain complex I. Furthermore, at low concentrations of NADH, the binding of L-3-hydroxyacyl-CoA dehydrogenase to complex I is abolished, indicating a specificity of this binding for metabolic channeling [106]. The hypothesis of an immediate interaction between β-oxidation and the respiratory chain has gained further support by the observation of a physical association between enzymes of mitochondrial β-oxidation and respiratory chain supercomplexes [107].

The formation of supercomplexes promotes direct electron transfer, mediates substrate channeling, increases catalytic efficiency, sequesters reactive

intermediates, and stabilizes respiratory chain complexes [52]. Mitochondrial supercomplexes consist of one complex I subunit, two complex III subunits and a variable number of complex IV subunits. In addition, the association of complex II with mitochondrial supercomplexes has been shown [108]. According Schägger et al. [51] approximately 84% of complex I is assembled into the supercomplexes I_1III_2, $I_1III_2IV_1$, and $I_1III_2IV_{2-4}$. Hence, only ~ 16 % of complex I is found in free form. In this study, the incorporation of $EHHADH_{MUT}$ into MTP led to decreased supercomplex assembly, as the erroneous incorporation of $EHHADH_{MUT}$ into MTP resulted in conformational changes of MTP and, thereby, reduced mitochondrial supercomplex formation by 44% in the *EHHADH$_{MUT}$* cell line.

It is also known, that decreased supercomplex assembly will reduce oxidative phosphorylation capacity [97,109]. By means of high-resolution respirometry a decreased oxidative phosphorylation capacity in the *EHHADH$_{MUT}$* cell line compared to the *EHHADH$_{WT}$* cell line was observed. The oxygen consumption after addition of palmitoylcarnitine for β-oxidation and pyruvate and glutamate for complex I showed a decrease in oxidative phosphorylation in *EHHADH$_{MUT}$* of 30 % and 33 %, respectively. Both indicate a decreased supply of reducing equivalents from β-oxidation and a modified tricarboxylic acid cycle. The addition of succinate can compensate to some extent the reduction in oxygen consumption to only 19 % in *EHHADH$_{MUT}$* cells. LEAK respiration, after the addition of oligomycin, is also significantly reduced in *EHHADH$_{MUT}$* cells compared to *EHHADH$_{WT}$* cells. One likely explanation may be alterations in the IMM that impact its flexibility and, thereby, respiration. Baggetto et al. [110] showed, that a higher cholesterol level in the IMM is accompanied by a decreased LEAK respiration due to decreased proton permeability. In addition, Brand et al. [111] showed, that the amount of ADP/ATP translocase has an impact on LEAK respiration. A decrease in the amount of ADP/ATP translocase led to a decrease in the proton conductance, whereas the opposite applied to an increase in abundance of ADP/ATP translocase. Since the *EHHADH$_{MUT}$* cell line showed indeed a decreased amount of ADP/ATP translocase, this might explain the decreased LEAK respiration. Further, as oxygen consumption by the *EHHADH$_{MUT}$* cell line was still significantly decreased after uncoupling, it appears both the phosphorylation and non-phosphorylation system are affected in the *EHHADH$_{MUT}$* cell line.

7.7 Development of diseases due to the mistargeting of proteins

Mistargeting of proteins and the causal correlation with the development of a disease is a subject of research over the last years. The here described autosomal dominant form of Fanconi´s syndrome is caused by the mistargeting of the peroxisomal protein EHHADH into mitochondria. In the following, I will compare the Faconi´s syndrome with other mistargeting caused diseases.

A first example in literature, where the mistargeting of a peroxisomal protein into mitochondria causes a genetic disease, was the autosomal recessive disease primary hyperoxaluria type 1 (PH1). Most of the patients with PH1 have a complete deficiency of the catalytic activity of the hepatic peroxisomal enzyme alanine/glyoxylate aminotransferase (AGT), however about a third of patients show residual enzyme activity [112]. Human AGT is a homodimeric protein, which is in human solely located in peroxisomes and catalyzes the transamination of glyoxylate to glycine. The deficiency of AGT in the peroxisomes leads to the formation of oxalate from glyoxylate catalyzed by either lactate dehydrogenase or glycolate oxidase, which in the following deposit as insoluble calcium oxalate in the kidney and the urinary tract [113]. The clinical presentations are urolithiasis and/or nephrocalcinosis and eventually lead to renal failure [114]. Over the past years a large number of different enzymatic phenotypes have been identified in PH1, including loss of the catalytic activity of AGT, protein deficiency, aggregation of AGT in peroxisomes and the mistargeting of AGT into mitochondria [113]. The latter takes place due to the combination of the polymorphism P11L and the PH1-specific point mutation G170R [112], whereby 90 – 95 % of AGT [114] is mistargeted into mitochondria. The combined effects of both mutations are the generation of a weak mitochondrial targeting sequence by the P11L polymorphism and the inhibition of the AGT dimerization by the G170R point mutation [112,113]. The dimerization of human AGT is very important, as it is shown that monomeric human AGT has a reduced catalytic acitivty [112] and is unstable , which leads to further rapid degradation [115]. The mistargeted AGT is in mitochondria still catalytic active, although it is metabolically inefficient [114].

Another example is the autosomal dominant nephrogenic diabetes insipidus (NDI), where the kidney fails to concentrate the urine in response to the anti-diuretic hormone arginine-vasopressin (AVP). AVP is produced in the pituitary and released in the case of hypernatremia or hypovolemia [116]. AVP then binds to the membranous vasopressin type-2 receptor and via cAMP signalling leads to the phosphorylation of

AQP2 by protein kinase A (PKA) [117] and insertion of Aquaporin-2 (AQP2) into the luminal membrane. This autosomal dominant form of NDI is caused by a single nucleotide deletion (727ΔG) in one allele of Aquaporin-2 gene, which leads to a C-terminal frame shift and thereby to an extended C-terminal tail [116]. The other allele encoded the wild type AQP2 protein. AQP2 is known to form homotetramers *in vivo* and *in vitro* [117,118] .Marr et al. [116] showed after co-expression of the wild type and mutated AQP2 in Madin-Darby kidney cells, the formed heterotetramer of wild type and mutated AQP2 was erroneously located mainly to the late endosomes/lysosomes after treatment with forskolin, an adenylate cyclase activator. Thereby, Marr et al. showed that not the loss of function, but rather the mistargeting of the heterotetramer of wild type and mutated AQP2 to the late endosomes/lysosomes lead to the phenotype [116].

Although PH1 and NDI are also caused by a mistargeting of a protein, the phenotypes of PH1 and NDI arises due to the absence of the protein in peroxisomes and apical membrane, respectively. Whereas in the here described Fanconi´s syndrome, the phenotype is caused by the erroneous localisation of $EHHADH_{MUT}$ in mitochondria and the following disturbance of normal mitochondrial function. Not the lack of the EHHADH in the peroxisomes leads to the development of the Fanconi´s syndrome, as an $EHHADH^{-/-}$ knockout mouse did not lead to a phenotype

In addition, $EHHADH_{MUT}$ is still transported to the peroxisomes, as shown by means of immunofluorescence staining.

To my knowledge, we showed for the first time, that not the failure, or the loss of function of the protein causes the disease, but rather the mistargeting of the protein into mitochondria and the resulting mitochondriopathy.

8 Conclusion and Outlook

Mistargeting of $EHHADH_{MUT}$ into mitochondria and incorporation into MTP leads to disturbed mitochondrial fatty acid β-oxidation and respiratory supercomplex formation. Due to impaired mitochondrial β-oxidation, *$EHHADH_{MUT}$* cells produce less acetyl-CoA, accumulate acylcarnitines, and take up less fatty acids. In addition, decreased supercomplex assembly is observed. Together they reduce oxidative phosphorylation capacity, leading to decreased mitochondrial energy production in the *$EHHADH_{MUT}$* cell line. Ultimately, this mitochondriopathy causes decreased tubular reabsorption of electrolytes and low-molecular-weight proteins, resulting in the Fanconi´s syndrome. This decreased tubular transport capacity for the nonmetabolizable glucose surrogate methyl α-D-glucoside in *$EHHADH_{MUT}$* cells compared to the *$EHHADH_{MUT}$* cell line was already shown by Klootwijk and coworkers [67].

Further research should aim at the analysis of intracellular long-chain acyl-CoA, as they exert a stronger inhibitory effect on mitochondrial and cellular transporters compared to long-chain acylcarnitines. In addition, the stoichiometry and abundance of incorporation of $EHHADH_{MUT}$ into MTP will be of interest, as it is shown by immunofluorescence analysis that not all MTP complexes are affected to the same extent, thus explaining the less severe accumulation of β-oxidation intermediates in comparison to other MTP deficiencies. In addition, the metabolic and proteomic analysis of urine and blood plasma specimens from affected family members will provide further insights into the underlying pathomechnism, as a cell culture model is and will remain an artificial system. Purification of MTP complex from both $EHHADH_{WT}$ and $EHHADH_{MUT}$ cells and determination of its activity based on established protocols [119-123] will provide insight into the functional consequences of the erroneous incorporation of $EHHADH_{MUT}$ into MTP.

III. References

1. Keller C, Geberth S. Praxis der Nephrologie. Springer Medizin Verlag, Heidelberg, Second Edition, 2007.
2. Schmidt RF, Lang F, Thews G. Physiologie des Menschen. Springer Medizin Verlag Heidelberg, Twenty-Ninth Edition, 2005.
3. Speckmann EJ, Hescheler J, Köhling R. Physiologie. Elsevier GmbH, München, Fifth Edition, 2008.
4. Avner ED, Harmon WE, Niaudet P, Yoshikawa N. Pediatric Nephrology. Springer Verlag Berlin Heidelberg, Sixth Edition, 2009.
5. Ganten D. RK. Grundlagen der Molekularen Medizin. Springer Medizin Verlag, Heidelberg, 3rd Edition, 2008.
6. Abderhalden E. Familiäre Cystindiathese. Z Physiol Chem 1903;38:557-61.
7. Andreoli TE, Hoffman JF, Fanestil DD, Schultz SG. Clinical Disorders of Membrane Transport Processes. Springer US, 1987.
8. Baum M. The Fanconi syndrome of cystinosis: insights into the pathophysiology. Pediatr Nephrol 1998;12:492-7.
9. Lignac GOE. Über Störung des Cystinstoffwechsels bei Kindern. Deut Arch Klin Med 1924;145:139-50.
10. Fanconi G. Die nicht diabetischen Glykosurien und Hyperglykämien des älteren Kindes. Jahrb Kinderheilkd 1931;133:257-300.
11. Clay RD, Darmady EM, Hawkins M. The nature of the renal lesion in the Fanconi syndrome. J Pathol Bacteriol 1953;65:551-8.
12. De Toni G. Remarks on the relations between renal rickets (renal dwarfism) and renal diabetes. Acta Paediatr 1933;16:479-84.
13. Debré R, Marie J, Cléret F, Messimy R. Rachitisme tardif coexistant avec une néphrite chronique et une glycosurie. Arch Med Enf 1934;37:597-606.
14. Fanconi G. Der frühinfantile nephrotisch-glykosurische Zwergwuchs mit hypophosphatämischer Rachitis. Jahrb Kinderheilkd 1936;147:299-338.
15. Nyhan WL, Barshop BA, Ozand P. Atlas of metabolic diseases. Oxford University Press Inc., Second Edition, 2005.
16. http://emedicine.medscape.com/article/981774-overview. (Accessed 15.01.2015)

17. McCune DJ. Intractable hypophosphatemic rickets with renal glycosuria and acidosis (the Fanconi syndrome). Am J Dis Child 1943;65:81.
18. Stowers JM, Dent CE. Studies on the mechanism of the Fanconi syndrome. Q J Med 1947;16:275-90.
19. Cho HY, Lee BH, Choi HJ, Ha IS, Choi Y, Cheong HI. Renal manifestations of Dent disease and Lowe syndrome. Pediatr Nephrol 2008;23:243-9.
20. Sirac C, Bridoux F, Essig M, Devuyst O, Touchard G, Cogne M. Toward understanding renal Fanconi syndrome: step by step advances through experimental models. Contrib Nephrol 2011;169:247-61.
21. Bokenkamp A, Bockenhauer D, Cheong HI, et al. Dent-2 disease: a mild variant of Lowe syndrome. J Pediatr 2009;155:94-9.
22. Bokenkamp A, Ludwig M. Disorders of the renal proximal tubule. Nephron Physiol 2011;118:p1-6.
23. Epstein FH. Oxygen and renal metabolism. Kidney Int 1997;51:381-5.
24. Beck JS, Breton S, Mairbaurl H, Laprade R, Giebisch G. Relationship between sodium transport and intracellular ATP in isolated perfused rabbit proximal convoluted tubule. Am J Physiol 1991;261:F634-9.
25. Ren H, Wang WM, Chen XN, et al. Renal involvement and followup of 130 patients with primary Sjogren's syndrome. J Rheumatol 2008;35:278-84.
26. Korbet SM, Schwartz MM. Multiple myeloma. J Am Soc Nephrol 2006;17:2533-45.
27. Watanabe T, Yoshikawa H, Yamazaki S, Abe Y, Abe T. Secondary renal Fanconi syndrome caused by valproate therapy. Pediatr Nephrol 2005;20:814-7.
28. Rifkin BS, Perazella MA. Tenofovir-associated nephrotoxicity: Fanconi syndrome and renal failure. Am J Med 2004;117:282-4.
29. Hong YT, Fu LS, Chung LH, Hung SC, Huang YT, Chi CS. Fanconi's syndrome, interstitial fibrosis and renal failure by aristolochic acid in Chinese herbs. Pediatr Nephrol 2006;21:577-9.
30. Isnard Bagnis C, Deray G, Baumelou A, Le Quintrec M, Vanherweghem JL. Herbs and the kidney. Am J Kidney Dis 2004;44:1-11.
31. Cleveland WW, Adams WC, Mann JB, Nyhan WL. Acquired Fanconi Syndrome Following Degraded Tetracycline. J Pediatr 1965;66:333-42.

32. Izzedine H, Launay-Vacher V, Isnard-Bagnis C, Deray G. Drug-induced Fanconi's syndrome. Am J Kidney Dis 2003;41:292-309.
33. Loghman-Adham M. Aminoaciduria and glycosuria following severe childhood lead poisoning. Pediatr Nephrol 1998;12:218-21.
34. Goyer RA. Mechanisms of lead and cadmium nephrotoxicity. Toxicol Lett 1989;46:153-62.
35. Yaffe MP. The machinery of mitochondrial inheritance and behavior. Science 1999;283:1493-7.
36. Schwartz M, Vissing J. Paternal inheritance of mitochondrial DNA. N Engl J Med 2002;347:576-80.
37. Gvozdjáková A. Mitochondrial Medicine: Mitochondrial Metabolism, Diseases, Diagnosis and Therapy. Springer Science + Buisness Media B.V., 2008.
38. Alberts B. JA, Lewis J., Raff M., Roberts K., Walter P. Molecular Biology and the Cell. Taylor and Francis Group, New York, Fifth edition, 2008.
39. Herrmann JM, Riemer J. The intermembrane space of mitochondria. Antioxid Redox Signal 2010;13:1341-58.
40. Schrader M, Yoon Y. Mitochondria and peroxisomes: are the 'big brother' and the 'little sister' closer than assumed? Bioessays 2007;29:1105-14.
41. Reddy JK, Hashimoto T. Peroxisomal beta-oxidation and peroxisome proliferator-activated receptor alpha: an adaptive metabolic system. Annu Rev Nutr 2001;21:193-230.
42. Mandel LJ. Metabolic substrates, cellular energy production, and the regulation of proximal tubular transport. Annu Rev Physiol 1985;47:85-101.
43. Bartlett K, Eaton S. Mitochondrial beta-oxidation. Eur J Biochem 2004;271:462-9.
44. Berg JM, Tymoczko JL, Stryer L. Stryer Biochemie. Elsevier GmbH, München, 6th Edition, 2007.
45. http://www.genenames.org/genefamilies/mitocomplex#FATP, Cambridge, HUGO Gene Nomenclature Committee
46. Kremer A. Crashkurs Biochemie. Elsevier GmbH, München, 1st Edition, 2005.
47. Lenaz G. Role of mobility of redox components in the inner mitochondrial membrane. J Membr Biol 1988;104:193-209.
48. Green DE, Tzagoloff A. The mitochondrial electron transfer chain. Arch Biochem Biophys 1966;116:293-304.

49. Hackenbrock CR, Chazotte B, Gupte SS. The random collision model and a critical assessment of diffusion and collision in mitochondrial electron transport. J Bioenerg Biomembr 1986;18:331-68.
50. Bianchi C, Genova ML, Parenti Castelli G, Lenaz G. The mitochondrial respiratory chain is partially organized in a supercomplex assembly: kinetic evidence using flux control analysis. J Biol Chem 2004;279:36562-9.
51. Schägger H, Pfeiffer K. The ratio of oxidative phosphorylation complexes I-V in bovine heart mitochondria and the composition of respiratory chain supercomplexes. J Biol Chem 2001;276:37861-7.
52. Schägger H. Respiratory chain supercomplexes. IUBMB life 2001;52:119-28.
53. Bruel C, Brasseur R, Trumpower BL. Subunit 8 of the Saccharomyces cerevisiae cytochrome bc1 complex interacts with succinate-ubiquinone reductase complex. J Bioenerg Biomembr 1996;28:59-68.
54. Boumans H, Grivell LA, Berden JA. The respiratory chain in yeast behaves as a single functional unit. J Biol Chem 1998;273:4872-7.
55. Schägger H, Pfeiffer K. Supercomplexes in the respiratory chains of yeast and mammalian mitochondria. The EMBO journal 2000;19:1777-83.
56. Schägger H. Respiratory chain supercomplexes of mitochondria and bacteria. Biochim Biophys Acta 2002;1555:154-9.
57. Meisinger C, Sickmann A, Pfanner N. The mitochondrial proteome: from inventory to function. Cell 2008;134:22-4.
58. Omura T. Mitochondria-targeting sequence, a multi-role sorting sequence recognized at all steps of protein import into mitochondria. J Biochem 1998;123:1010-6.
59. Pfanner N, Wiedemann N. Mitochondrial protein import: two membranes, three translocases. Curr Opin Cell Biol 2002;14:400-11.
60. Hasan S, Platta HW, Erdmann R. Import of proteins into the peroxisomal matrix. Front Physiol 2013;4:261.
61. Fawcett DW. The Cell. Urban und Schwarzenberg, München, 1981.
62. Wanders RJ, Waterham HR. Biochemistry of mammalian peroxisomes revisited. Annu Rev Biochem 2006;75:295-332.
63. Hoefler G, Forstner M, McGuinness MC, et al. cDNA cloning of the human peroxisomal enoyl-CoA hydratase: 3-hydroxyacyl-CoA dehydrogenase

bifunctional enzyme and localization to chromosome 3q26.3-3q28: a free left Alu Arm is inserted in the 3' noncoding region. Genomics 1994;19:60-7.

64. Reddy MK, Usuda N, Reddy MN, Kuczmarski ER, Rao MS, Reddy JK. Purification, properties, and immunocytochemical localization of human liver peroxisomal enoyl-CoA hydratase/3-hydroxyacyl-CoA dehydrogenase. Proc Natl Acad Sci U S A 1987;84:3214-8.
65. Qi C, Zhu Y, Pan J, et al. Absence of spontaneous peroxisome proliferation in enoyl-CoA Hydratase/L-3-hydroxyacyl-CoA dehydrogenase-deficient mouse liver. Further support for the role of fatty acyl CoA oxidase in PPARalpha ligand metabolism. J Biol Chem 1999;274:15775-80.
66. Houten SM, Denis S, Argmann CA, et al. Peroxisomal L-bifunctional enzyme (Ehhadh) is essential for the production of medium-chain dicarboxylic acids. J Lipid Res;53:1296-303.
67. Klootwijk ED, Reichold M, Helip-Wooley A, et al. Mistargeting of peroxisomal EHHADH and inherited renal Fanconi's syndrome. N Engl J Med 2014;370:129-38.
68. Dettmer K, Nurnberger N, Kaspar H, Gruber MA, Almstetter MF, Oefner PJ. Metabolite extraction from adherently growing mammalian cells for metabolomics studies: optimization of harvesting and extraction protocols. Anal Bioanal Chem 2011;399:1127-39.
69. Masood A, Stark KD, Salem N, Jr. A simplified and efficient method for the analysis of fatty acid methyl esters suitable for large clinical studies. J Lipid Res 2005;46:2299-305.
70. Kuznetsov A, Lassnig B, Gnaiger E. Course on High-Resolution Respirometry - Laboratory Protocol Citrate Synthase Mitochondrial Marker Enzyme In: Mitochondrial Physiology Network 814; 2003.
71. Wisniewski JR, Zougman A, Nagaraj N, Mann M. Universal sample preparation method for proteome analysis. Nat Methods 2009;6:359-62.
72. Benjamini Y, Hochberg Y. Controlling the False Discovery Rate: a Practical and Powerful Approach to Multiple Testing. J Roy Stat Soc B 1995;57:289-300.
73. Shekhawat PS, Matern D, Strauss AW. Fetal fatty acid oxidation disorders, their effect on maternal health and neonatal outcome: impact of expanded

newborn screening on their diagnosis and management. Pediatr Res 2005;57:78R-86R.

74. ter Veld F, Primassin S, Hoffmann L, Mayatepek E, Spiekerkoetter U. Corresponding increase in long-chain acyl-CoA and acylcarnitine after exercise in muscle from VLCAD mice. J Lipid Res 2009;50:1556-62.
75. Sim KG, Hammond J, Wilcken B. Strategies for the diagnosis of mitochondrial fatty acid beta-oxidation disorders. Clin Chim Acta 2002;323:37-58.
76. Tyni T, Pourfarzam M, Turnbull DM. Analysis of mitochondrial fatty acid oxidation intermediates by tandem mass spectrometry from intact mitochondria prepared from homogenates of cultured fibroblasts, skeletal muscle cells, and fresh muscle. Pediatr Res 2002;52:64-70.
77. Rinaldo P, Cowan TM, Matern D. Acylcarnitine profile analysis. Genet Med 2008;10:151-6.
78. Giak Sim K, Carpenter K, Hammond J, Christodoulou J, Wilcken B. Quantitative fibroblast acylcarnitine profiles in mitochondrial fatty acid beta-oxidation defects: phenotype/metabolite correlations. Mol Genet Metab 2002;76:327-34.
79. Ventura FV, Ijlst L, Ruiter J, et al. Carnitine palmitoyltransferase II specificity towards beta-oxidation intermediates--evidence for a reverse carnitine cycle in mitochondria. Eur J Biochem 1998;253:614-8.
80. Zierz S, Neumann-Schmidt S, Jerusalem F. Inhibition of carnitine palmitoyltransferase in normal human skeletal muscle and in muscle of patients with carnitine palmitoyltransferase deficiency by long- and short-chain acylcarnitine and acyl-coenzyme A. Clin Investig 1993;71:763-9.
81. Sander J, Sander S, Steuerwald U, et al. Neonatal screening for defects of the mitochondrial trifunctional protein. Mol Genet Metab 2005;85:108-14.
82. Frohnert BI, Bernlohr DA. Regulation of fatty acid transporters in mammalian cells. Prog Lipid Res 2000;39:83-107.
83. Doege H, Stahl A. Protein-mediated fatty acid uptake: novel insights from in vivo models. Physiology (Bethesda) 2006;21:259-68.
84. Eaton S. Control of mitochondrial beta-oxidation flux. Prog Lipid Res 2002;41:197-239.
85. Oram JF, Wenger JI, Neely JR. Regulation of long chain fatty acid activation in heart muscle. J Biol Chem 1975;250:73-8.

86. Hall AM, Smith AJ, Bernlohr DA. Characterization of the Acyl-CoA synthetase activity of purified murine fatty acid transport protein 1. J Biol Chem 2003;278:43008-13.
87. Rasmussen JT, Rosendal J, Knudsen J. Interaction of acyl-CoA binding protein (ACBP) on processes for which acyl-CoA is a substrate, product or inhibitor. Biochem J 1993;292 (Pt 3):907-13.
88. O'Donnell JM, Alpert NM, White LT, Lewandowski ED. Coupling of mitochondrial fatty acid uptake to oxidative flux in the intact heart. Biophys J 2002;82:11-8.
89. Gullans SR, Brazy PC, Soltoff SP, Dennis VW, Mandel LJ. Metabolic inhibitors: effects on metabolism and transport in the proximal tubule. Am J Physiol 1982;243:F133-40.
90. Soltoff SP, Mandel LJ. Active ion transport in the renal proximal tubule. III. The ATP dependence of the Na pump. J Gen Physiol 1984;84:643-62.
91. Andreoli SP, Mallett CP. Disassociation of oxidant-induced ATP depletion and DNA damage from early cytotoxicity in LLC-PK1 cells. Am J Physiol 1997;272:F729-35.
92. Balaban RS, Mandel LJ, Soltoff SP, Storey JM. Coupling of active ion transport and aerobic respiratory rate in isolated renal tubules. Proc Natl Acad Sci U S A 1980;77:447-51.
93. Migita K, Zhao Y, Katsuragi T. Mitochondria play an important role in adenosine-induced ATP release from Madin-Darby canine kidney cells. Biochem Pharmacol 2007;73:1676-82.
94. Deracinois B, Flahaut C, Duban-Deweer S, Karamanos Y. Comparative and Quantitative Global Proteomics Approaches: An Overview. Proteomes 2013;1:180-218.
95. Schägger H, de Coo R, Bauer MF, Hofmann S, Godinot C, Brandt U. Significance of respirasomes for the assembly/stability of human respiratory chain complex I. J Biol Chem 2004;279:36349-53.
96. Acin-Perez R, Bayona-Bafaluy MP, Fernandez-Silva P, et al. Respiratory complex III is required to maintain complex I in mammalian mitochondria. Mol Cell 2004;13:805-15.

97. D'Aurelio M, Gajewski CD, Lenaz G, Manfredi G. Respiratory chain supercomplexes set the threshold for respiration defects in human mtDNA mutant cybrids. Hum Mol Genet 2006;15:2157-69.
98. Gutierrez-Aguilar M, Baines CP. Physiological and pathological roles of mitochondrial SLC25 carriers. Biochem J 2013;454:371-86.
99. Fiore C, Trezeguet V, Le Saux A, et al. The mitochondrial ADP/ATP carrier: structural, physiological and pathological aspects. Biochimie 1998;80:137-50.
100. Ventura FV, Ruiter J, Ijlst L, de Almeida IT, Wanders RJ. Differential inhibitory effect of long-chain acyl-CoA esters on succinate and glutamate transport into rat liver mitochondria and its possible implications for long-chain fatty acid oxidation defects. Mol Genet Metab 2005;86:344-52.
101. Ciapaite J, van Eikenhorst G, Krab K. Application of modular control analysis to inhibition of the adenine nucleotide translocator by palmitoyl-CoA. Mol Biol Rep 2002;29:13-6.
102. Vaartjes WJ, Kemp A, Souverijn JH, van den Bergh SG. Inhibition by fatty acyl esters of adenine nucleotide translocation in rat-liver mitochondria. FEBS Lett 1972;23:303-8.
103. Shrago E, Woldegiorgis G, Ruoho AE, DiRusso CC. Fatty acyl CoA esters as regulators of cell metabolism. Prostaglandins Leukot Essent Fatty Acids 1995;52:163-6.
104. Chua BH, Shrago E. Reversible inhibition of adenine nucleotide translocation by long chain acyl-CoA esters in bovine heart mitochondria and inverted submitochondrial particles. Comparison with atractylate and bongkrekic acid. J Biol Chem 1977;252:6711-4.
105. Sumegi B, Srere PA. Complex I binds several mitochondrial NAD-coupled dehydrogenases. J Biol Chem 1984;259:15040-5.
106. Fukushima T, Decker RV, Anderson WM, Spivey HO. Substrate channeling of NADH and binding of dehydrogenases to complex I. J Biol Chem 1989;264:16483-8.
107. Wang Y, Mohsen AW, Mihalik SJ, Goetzman ES, Vockley J. Evidence for physical association of mitochondrial fatty acid oxidation and oxidative phosphorylation complexes. J Biol Chem 2010;285:29834-41.
108. Acin-Perez R, Fernandez-Silva P, Peleato ML, Perez-Martos A, Enriquez JA. Respiratory active mitochondrial supercomplexes. Mol Cell 2008;32:529-39.

109. Rosca MG, Vazquez EJ, Kerner J, et al. Cardiac mitochondria in heart failure: decrease in respirasomes and oxidative phosphorylation. Cardiovasc Res 2008;80:30-9.
110. Baggetto LG, Clottes E, Vial C. Low mitochondrial proton leak due to high membrane cholesterol content and cytosolic creatine kinase as two features of the deviant bioenergetics of Ehrlich and AS30-D tumor cells. Cancer Res 1992;52:4935-41.
111. Brand MD, Pakay JL, Ocloo A, et al. The basal proton conductance of mitochondria depends on adenine nucleotide translocase content. Biochem J 2005;392:353-62.
112. Lumb MJ, Danpure CJ. Functional synergism between the most common polymorphism in human alanine:glyoxylate aminotransferase and four of the most common disease-causing mutations. J Biol Chem 2000;275:36415-22.
113. Danpure CJ, Lumb MJ, Birdsey GM, Zhang X. Alanine:glyoxylate aminotransferase peroxisome-to-mitochondrion mistargeting in human hereditary kidney stone disease. Biochim Biophys Acta 2003;1647:70-5.
114. Danpure CJ. Primary hyperoxaluria type 1: AGT mistargeting highlights the fundamental differences between the peroxisomal and mitochondrial protein import pathways. Biochim Biophys Acta 2006;1763:1776-84.
115. Danpure CJ, Purdue PE, Fryer P, et al. Enzymological and mutational analysis of a complex primary hyperoxaluria type 1 phenotype involving alanine:glyoxylate aminotransferase peroxisome-to-mitochondrion mistargeting and intraperoxisomal aggregation. Am J Hum Genet 1993;53:417-32.
116. Marr N, Bichet DG, Lonergan M, et al. Heteroligomerization of an Aquaporin-2 mutant with wild-type Aquaporin-2 and their misrouting to late endosomes/lysosomes explains dominant nephrogenic diabetes insipidus. Hum Mol Genet 2002;11:779-89.
117. Kamsteeg EJ, Heijnen I, van Os CH, Deen PM. The subcellular localization of an aquaporin-2 tetramer depends on the stoichiometry of phosphorylated and nonphosphorylated monomers. J Cell Biol 2000;151:919-30.
118. Kamsteeg EJ, Wormhoudt TA, Rijss JP, van Os CH, Deen PM. An impaired routing of wild-type aquaporin-2 after tetramerization with an aquaporin-2

mutant explains dominant nephrogenic diabetes insipidus. EMBO J 1999;18:2394-400.

119. Tyni T, Johnson M, Eaton S, Pourfarzam M, Andrews R, Turnbull DM. Mitochondrial fatty acid beta-oxidation in the retinal pigment epithelium. Pediatr Res 2002;52:595-600.
120. Wanders RJ, L IJ, Poggi F, et al. Human trifunctional protein deficiency: a new disorder of mitochondrial fatty acid beta-oxidation. Biochem Biophys Res Commun 1992;188:1139-45.
121. Wanders RJ, Ruiter JP, L IJ, Waterham HR, Houten SM. The enzymology of mitochondrial fatty acid beta-oxidation and its application to follow-up analysis of positive neonatal screening results. J Inherit Metab Dis 2010;33:479-94.
122. Uchida Y, Izai K, Orii T, Hashimoto T. Novel fatty acid beta-oxidation enzymes in rat liver mitochondria. II. Purification and properties of enoyl-coenzyme A (CoA) hydratase/3-hydroxyacyl-CoA dehydrogenase/3-ketoacyl-CoA thiolase trifunctional protein. J Biol Chem 1992;267:1034-41.
123. Wanders RJ, L IJ, van Gennip AH, et al. Long-chain 3-hydroxyacyl-CoA dehydrogenase deficiency: identification of a new inborn error of mitochondrial fatty acid beta-oxidation. J Inherit Metab Dis 1990;13:311-4.